Frantz Stabo-Eeg

Development of instrumentation for Mueller matrix ellipsometry

Thesis for the degree of Philosophiae Doctor

Trondheim, February 2009

Norwegian University of Science and Technology
Faculty of Natural Sciences and Technology
Department of Physics

NTNU
Norwegian University of
Science and Technology

NTNU
Norwegian University of Science and Technology

Thesis for the degree of Philosophiae Doctor

Faculty of Natural Sciences and Technology
Department of Physics

© Frantz Stabo-Eeg

ISBN 978-82-471-1432-2 (printed ver.)
ISBN 978-82-471-1434-6 (electronic ver.)
ISSN 1503-8181

Doctoral theses at NTNU, 2009:32

Printed by NTNU-trykk

Abstract

This thesis gives an introduction to the Mueller-Stokes calculus, which is used to describe partially and fully polarized light. It describes how polarized light interacts with various sample configurations resulting in a Mueller matrix, and how this can be measured by using appropriate instrumentation. Specifically, two such Mueller matrix ellipsometers have been realized. One system is based on rotating Fresnel bi-prism and the other on Ferro-electric liquid crystals. The systems are unique in different ways. The rotating Fresnel bi-prism Mueller matrix ellipsometer is an optimal UV-NIR achromatic suitable for high power angular scattering measurements. The Ferro-electric liquid crystals Mueller matrix ellipsometer is a fast acquisition system capable of measuring Mueller matrices at 50 Hz.

The thesis gives an introduction to the topics discussed in the attached six scientific papers. The first three papers report on construction and design of the ellipsometers. Paper I describes the design and characterization of two achromatic 132° bi-prism compensators optimized for Mueller matrix applications, while paper II describes an actual implementation and tests of an optimal Mueller matrix ellipsometer using these prisms. Chapter 5 of this thesis, shows results from scattering and fluorescence measurements using this system. The Ferro-electric liquid crystals based Mueller matrix ellipsometer is outlined in Paper III. In Section 5.4 of this thesis, it is shown how this system can be extended to an imaging polarimeter. In paper II,III, IV and V some other applications of the systems are shown, which also test the performances.

- Paper I
  The Fresnel bi-prism approach, also known as "achromatic device 1 (AD1)", was used in Paper I to design two achromatic 132° compensators. Such compensators are favorable in Mueller matrix ellipsometers, since they are capable of producing optimal conditioned system matrices leading to small experimental errors. Several papers describe the design of achromatic half-wave or quarter-wave prisms, but to our knowledge no other papers has yet described achromatic 132° prism designs. The actual measured retardation of two different prism materials, CaF_2 and fused silica, are given. It was concluded that CaF_2 is the superior material of the two concerning both spectral range (185 - 8000 nm) and refractive index dispersion. Both prisms are specifically promising in broad band applications like for instance synchrotron based systems.

- Paper II
  A well conditioned multiple laser Mueller ellipsometer is constructed using the bi-prisms in Paper I . The well conditioning makes the system less sen-

sitive to calibration errors and noise. Several papers have outlined the importance of well conditioned system matrices also noted by Paper I. Paper II includes a complete deduction, concerning the relation between the condition numbers and experimental errors. In particular it is shown how the measured matrix errors are directly related to the product of the condition numbers and the calibration errors. In contradiction to the condition number's significance, few papers report the actual values obtained from working systems. This paper describes the instrumentation of an optimal broad band polarimeter with accompanying experimental results and the actual measured condition numbers during operation. The ability to measure physical realizable Mueller matrices is also discussed. To our knowledge, no other system design has obtained such well conditioned system matrices over the reported spectral range from UV to NIR.

- Paper III
  Systems based on mechanical rotation of prisms, like that of Paper II, can be very slow compared to other technologies. The Liquid Crystals (LC) technology is for instance capable of operating at least one order of magnitude faster. Previously, LC Mueller matrix ellipsometers in the visible range has been reported. Paper III extends this range into the infra-red using Ferro Electric Liquid Crystals (FLC). As in Paper II, the design is chosen based on optimization on the condition numbers of the ellipsometer's system matrices. Fixed waveplates are included in the design in order to optimize the performance of the polarimeter. This results in a near optimal broad band performance. The measured actual switching times and retardation of the crystals are also reported. Based on stability considerations it is concluded that the FLC are capable of measuring a full Mueller matrices at 50 Hz. Paper III elaborates further on the first near infra-red-FLC spectroscopic Mueller matrix design and shows the first initial results.

- Paper IV
  In complex media, like for instance tissue or other biological material, optical models can be hard, if not impossible, to obtain. Other analyzing techniques are then valuable. The Lu-Chipman matrix product decomposition is one such technique which can be used in order to obtain new knowledge of the system. Knowledge of artifacts generated by the decomposition itself is also needed in order to correctly interpret results. In Paper IV , three simple optical components are studied, a visible polarizer, a IR polarizer and a roughened glass plate. The azimuth orientations of such homogeneous polarization elements may be estimated from the direction of the eigenpolarization of the decomposed matrices. It is here demonstrated that there is an

apparent ambiguity in the determination of both the azimuth angles and the absolute retardance. For instance, one has to assume some prior knowledge of the system in order to interpret the absolute retardance value and orientation correctly. The paper reports on results from the FLC Mueller matrix ellipsometer.

- Paper V
  The polarization response from a sample tends to provide information that is largely uncorrelated with spectral and intensity images and can give complementary information about samples. In Paper V several different types of land mines and three types of plants are investigated by detecting the Mueller matrix in a back scattering geometry at both specular and of specular angles. The depolarization index is concluded to be the polarization metric containing the most information, as it varies largely from sample to sample. The other polarization metrics like diattenuation and retardance is close to zero for back scattering geometries. The result shown that plants depolarize light more during 1570 nm coherent illumination than the mines. Depolarization information give complementary information and is capable of discriminating plants from surface mines. The depolarization profiles for the non-specular angles are shown to result in a Lorentzian profile.

- Paper VI
  A part of this thesis work was also to study particles, such as aggregated proteins. Some Mueller matrix measurements of the protein Human transthyretin (TTR) are included in Chapter 5. In order to study protein conformation luminescent probes can be used. In Paper VI, three different conjugated polymers, currently used to study protein conformations, are optical characterized. All three polymers PTAA, POMT and POWT are constructed from a conjugated polythiophene backbone, but with different attached side groups. PTAA is an acetic acid, while POMT and POWT have amino acid based side-chains. By varying the ionic strength of the buffer solutions the polymers can be forced to twist and bend, due to charging or neutralization of the side-chains. The twist and bend of the polymers cause shift in the energy levels. Both the quantum efficiency and two photon absorption cross sections of the polymers are studied in this paper under various pH buffer solutions. Of the three studied polymers, POMT is shown to have both a better quantum efficiency and a larger two-photon absorption cross section. An example of spectral imaging using POMT attached to amyloidal fibrils is also given.

Acknowledgments

The past four years have been both challenging and rewarding, and many people should be thanked for their support and friendship during these years. First and foremost I would like to thank my supervisor and now friend professor Mikael Lindgren for inviting me to do a PhD some years ago. I am very thankful for his help, feedback and patience in improving the scientific contents and language of this thesis and attached publications. Both Mikael Lindgren and my co-supervisor Morten Kildemo have provided me with several helpful discussions and ideas during my work, which have been greatly appreciated.

Work related to protein aggregation could not have been done without the helpful collaborators Per Hammarström, Peter Nilsson and Karin Sörgjerd at Linköping university. They provided me with proteins and conjugated polymers samples and helpful discussions. The mine fragment samples were provided by Ove Steinvall and Dietmarat Letalick at the Swedish Defence Research Agency (FOI). I also appreciated the collaboration I had with Master students Jarle Landstein, Hallvard Skjerping and Lars M. Sandvik who have put a lot of effort and work into the liquid crystal based system in this thesis. The mechanical workshop group at the physics department has been very helpful in making parts for the instruments. I would also like to thank Kay Gastinger and the rest of SINTEF IKT, who have been very helpful in lending me various intstruments and optical components. I would like to thank my fellow PhD-colleagues working with optics; Ingar Nerbø which also contributed to some of the articles, and Eirik Glimsdal for correcting misprints in the thesis and general discussion about Matlab and Latex. Furthermore I would like to thank my other Trondheim friends and fellow PhD-colleagues, Christian, Lars L., Bjarte, Martin, Edrun, Jan Øystein, Jan Petter, Eskil, Per Kristian, Kristine, Alex, Marte H., Marte G., Lars Erik, Thomas, Henrik, Danni and Dionne, who have made the last couple of years memorable.

I specially thank my beloved partner Lillian Kråkmo, for helping me with the matrix algebra within this thesis, for believing in me and for giving me a son. Sverre, thank you for not eating up any part of this thesis work and for until now being a great kid.

List of Papers

Paper I
Stabo-Eeg, Frantz, Kildemo, Morten, Garcia-Caurel, Enric and Lindgren, Mikael.
"Design and characterization of achromatic 132° *retarders in* CaF_2 *and fused silica."*
Journal of Modern Optics **55**, (14), 2203-2214, (2008)

Paper II
Stabo-Eeg, Frantz; Kildemo, Morten; Nerbø , Ingar Stian and Lindgren, Mikael.
"A well conditioned multiple laser Mueller matrix ellipsometer."
Optical Engineering **47**(7), 073604 (2008)

Paper III
Ladstein, Jarle; Stabo-Eeg, Frantz; Garcia-Caurel, Enric and Kildemo, Morten
"Fast near-infra-red spectroscopic Mueller matrix ellipsometer based on ferroelectric liquid crystal retarders."
Phys Stat Solidi (c) **5**, No. 5, 1097-1100 (2008)

Paper IV
Stabo-Eeg, Frantz; Ladstein, Jarle and Kildemo, Morten
"Product decomposition of measured Mueller matrices from the FLC based NIR Mueller Matrix Ellipsometer".
Phys Stat Solidi (c) **5**, No. 5, 1093-1096 (2008)

Paper V
Stabo-Eeg, Frantz; Letalick, Dietmar; Steinvall, Ove; and Lindgren, Mikael.
"Discriminating land mines from natural backgrounds by depolarization".
Proc. SPIE , Paper 7114-16 (2008.) (Preprint)

Paper VI
Stabo-Eeg, Frantz; Hammarström, Per; Inganäs, Olle; Nilsson, K. Peter R.; Lindgren, Mikael.
"Quantum efficiency and two-photon absorption cross-section of conjugated polyelectrolytes used for protein conformation measurements with applications on amyloid structures".
Chemical Physics **336** 121-126 (2007).

My contribution to the papers

Paper I:
The paper was written by me and I have performed all the major parts of the work, including design, measurements and analysis of measurements. Mikael Lindgren and Morten Kildemo helped with discussion and presentation of the paper. Enric Garcia-Caurel provided me with several of the references concerning other prisms.

Paper II:
The paper was written by me and I have contributed substantially to all parts of the work, including design, construction, measurements and analysis of measurements. Mikael Lindgren and Morten Kildemo helped with discussion and presentation of the paper. Matlab tools for analyzing the reflection at a SiO2 /c-Si interface were provided by Ingar Stian Nerbø. Both Ingar Stian Nerbø and I contributed to calculation found the appendix with some help from Elena Celledoni. All other Labview and Matlab programs were written by me except some of the motion control parts of the gonorimeter provided to me by Jarle Landstein.

Paper III:
Morten Kildemo wrote the paper. The Matlab code for the calibration process was programmed by me as well as the product decomposition tools needed in the analysis of the results. The Labview programming for the instrumentation was mainly programmed by Jarle Landstein, but I also contributed to some parts of this code. I also took part in interpreting the results and contributed to the general discussion around the results.

Paper IV
The paper was written by me and I have contributed substantially to all parts of the paper. Morten Kildemo helped with analyzing and discussing the results. He also helped with presentation of the paper. Jarle Landstein performed the actual measurements.

Paper V:
The paper was written by me and I have contributed substantially to all parts of the work. All polarimetric measurements are performed by me, while reflection measurements results were provided by Dietmar Letalick and Ove Steinvall. Mikael Lindgren helped with data analysis, discussion and presentation of the paper.

Paper VI:
The paper was written by me in collaboration with Mikael Lindgren. K. Peter R. Nilsson provided the polymers and Per Hammarström performed the synthesis of the polymers. All authors contributed to the general discussion of the paper. Rajesh Mishra provided helpful discussions about insulin amyloid heterogeneity and provided the measurements included in the application

Other Publications not included in the thesis

- Ladstein, Jarle; Kildemo, Morten; Svendsen, Guro K.; Nerbø,Ingar S.; Stabo-Eeg, Frantz.
  "Characterisation of liquid crystals for broadband optimal design of Mueller matrix ellipsometers."
  Proceedings of SPIE Vol. **5687** (2007).

- Nilsson, K. Peter R.; Åslund, Andreas; Berg, Ina; Nyström, Sofie; Konradsson, Peter; Herland, Anna; Inganäs, Olle; Stabo-Eeg, Frantz; Lindgren, Mikael; Westermark, Gunilla T.; et al..
  "Imaging Distinct Conformational States of Amyloid-B Fibrils in Alzheimer's Disease Using Novel Luminescent Probes."
  ACS Chemical Biology **2**:553-560 (2007).

- Røyset, Arne; Støren, Trude Elna Marie; Stabo-Eeg, Frantz; Lindmo, Tore.
  "Quantitative measurements of flow velocity and direction using transversal Doppler optical coherence tomography."
  Proceedings of SPIE Vol. **6079** (2006).

- Nilsson, K. Peter R.; Olsson, Johan D. M.; Lindgren, Mikael; Stabo-Eeg, Frantz; Konradsson, Peter; Inganäs, Olle.
  "Chiral recognition of a synthetic peptide using enantiomeric conjugated polyelectrolytes and optical spectroscopy."
  Macromolecules **38**(16):6813-6821 (2005).

- Lindgren, Mikael; Stabo-Eeg, Frantz; Schnell, Edrun Andrea; Nilsson, K. Peter R.; Inganäs, Olle.
  "Biosensing and imaging with enantiomeric luminescent conjugated polythiophenes using multiphoton excitation."
  Proceeedings of SPIE Vol. **5935** (2005).

- Stabo-Eeg, Frantz; Gastinger, Kay; Hunderi, Ola; Lindgren, Mikael.
  "Determination of the phase and polarization changing properties of reflective spatial light modulators in one set-up."
  Proceedings of SPIE Vol. **5618** (2004).

Contents

Preface

This thesis is submitted as a partial fulfillment of the requirements for the degree of Philosophia Doctor (PhD) at the University of Science and Technology (NTNU). The study was performed at the Department of Physics, under supervision of Professor Mikael Lindgren and Associate Professor Morten Kildemo.

The work started September 2004 and ended December 2008. The employment also included teaching duties equivalent to one year, as well as following PhD-courses amounting to one semester full-time study.

Frantz Stabo-Eeg

1 Introduction

The vectorial nature of light is called polarization. It is one of the fundamental properties of light beside intensity, wavelength and coherence [1]. Light can be more or less polarized depending on how it is generated and how it interacts with matter. The light's polarization can be viewed in many everyday phenomena Figure 1.1. For instance, light becomes polarized when reflected from surfaces. This is clearly seen when viewing light reflections from a water surface through polaroid glasses. Particles that are much smaller than the wavelength cause the unpolarized sunlight to become strongly polarized. This scattering effect is known as Rayleigh scattering [2] and results in a polarization dependent pattern in the sky's hemisphere. Many living organism like insects [3] have polarization dependent vision and can utilize the natural polarization of the sky's hemisphere for navigation. Also many sea living animals can see polarized light. It has even been suggested that animals like cuttlefish use polarization to communicate [4]. Although animals have used polarization for a long time, the first recorded scientific observation of polarization was not until the discovery of double refraction in calcite (Iceland spar) in 1669, by Erasmus Bartholinus [5]. The Vikings may have utilized the sky's polarization in navigation, but this is disputed [6]. The history of polarization has been summarized by several authors [1, 7–10].

The late discovery of polarization is probably related to the poor polarization sensitivity of the human eye. A human observer can be trained to see polarization [11], visible as a yellowish bow-tie shape called the Haidinger's brush. It got its named after Wilhelm Karl von Haidinger who first described it in 1844 [12]. Most people do not notice polarized light without wearing some kind of optical device, such as polaroid glasses. Several instruments called polarimeters or ellipsometers have been developed in order to investigate the polarization's interaction with matter. The first documented polarimeter was constructed by Biot in 1816 [13] which soon found its applications in sugar production [14].

The study of polarization has evolved into several scientific topics both within chemistry, biology and physics. Today polarization has many applications, such as ellipsometry, astronomical polarimetry, spectropolarimetry, radar polarimetry, remote sensing, polarization light scattering, cryptography and general studies of optical components [15].

Polarization can be described in different ways, see for instance Section 2.3. Here the Stokes-Mueller calculus, which can describe randomly fluctuating light or

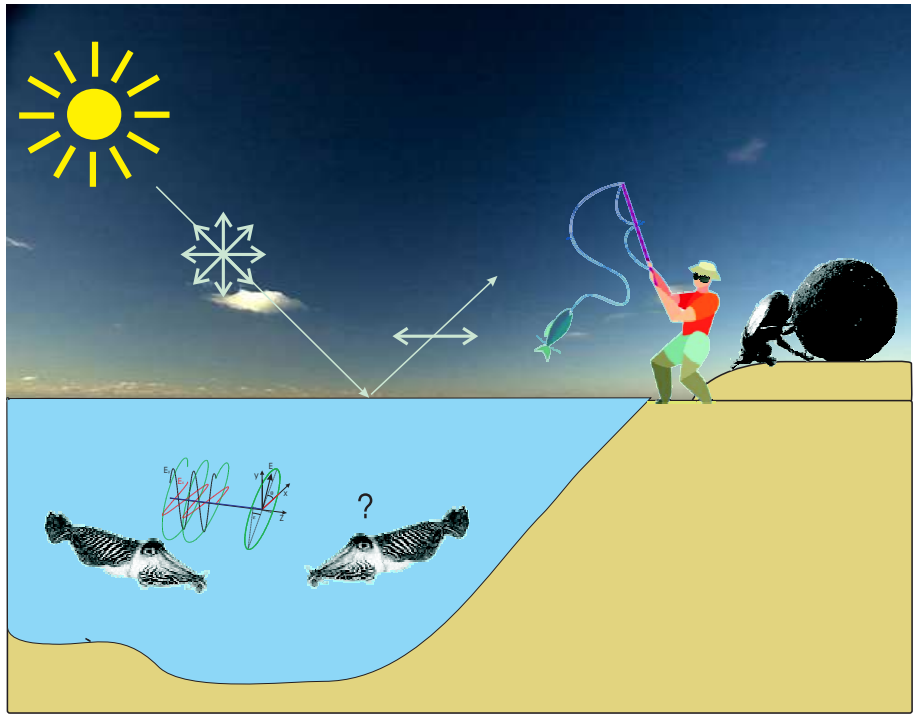

Figure 1.1: *Some effects of polarization as it appears in nature. The polarization of the sky is utilized by many insects, like for instance the dung beetle. The sky's polarization can be seen by wearing polaroid glasses. Cuttlefish might even use polarization to communicate [4].*

depolarized light, will be used. The ability of a sample to produce depolarized light is sometimes the only polarization metric which can distinguish objects, especially in backscattering geometries, see for instance Paper V or [16]. The alteration of the polarization state can be described by the Mueller matrix. It is basically a transfer matrix for both polarized and depolarized light. This transfer matrix can be measured by an optical technique referred to as either Mueller matrix polarimetry or Mueller Matrix Ellipsometry (MME).

Chapter 2 gives a short introduction to how polarized light is described by Stokes vectors and interacts with samples though Mueller matrices. Chapter 3 gives an introduction to how the Mueller matrix of a sample can be measured, and describe two such developed instruments, how they were optimized and calibrated. The measured Mueller matrix can sometimes be unphysical due to incorporated random noise or calibration errors. How to obtain physically realizable Mueller matrices is discussed in Chapter 4. Ellipsometry traditionally obtains physical information about the sample by modeling. When modeling is computationally difficult or impossible alternative techniques is important. This is discussed in

Chapter 4. Chapter 5 gives an introduction to studied unpublished applications of Mueller matrix ellipsometry, hence scattering, fluorescence and Mueller matrix imaging polarimetry, based on recent measurements. Chapter 6 gives a short summary and conclusion of this thesis work.

2 Polarized light

The following chapter gives an introduction to the notation used in the thesis and will serve as a brief introduction to the Mueller-Stokes calculus. A historical description to the origin to the Mueller-Stokes calculus can be found elsewhere [8].

2.1 Polarized light and the polarization ellipse

In the literature one finds different definitions of the polarization parameters. Here the convention proposed by Hauge *et al.* [17] will be used. The electric field components for fully polarized light propagating along the z-axis, are then decomposed into,

$$E_x(z,t) = \mathbf{Re}\left[E_{x0}e^{\left(i\omega t - \frac{2\pi z}{\lambda} + \delta_x\right)}\right],\ E_y(z,t) = \mathbf{Re}\left[E_{y0}e^{\left(i\omega t - \frac{2\pi z}{\lambda} + \delta_y\right)}\right], \tag{2.1}$$

where E_{x0} and E_{y0} are amplitudes, ω the angular frequency, λ the wavelength and δ_x and δ_y the phases for the electric field's x and y polarizations, respectively. The end point of the electrical field vector for fully polarized light generally follows an ellipse when traced at the same position in space over one period $T = \frac{2\pi}{\omega}$, see Figure 2.1. For a phase-shift of exactly $\delta = \delta_y - \delta_x = \frac{\pi}{2} \pm n \cdot \pi$ one has circularly polarized light. The clockwise rotation of the electric field, when viewed into the source, is defined as right circular polarization. The ellipticity ϵ, is defined as the tangent between the half axes of this ellipse, whereas the azimuth angle θ is defined as the rotation of its major axis. ϵ and θ can be shown to be the related to the phases and amplitudes of the electric fields compontents [17],

$$\sin 2\epsilon = \frac{2E_{x0}E_{y0}}{E_{x0}^2 + E_{y0}^2}\sin\delta,\ \ \tan 2\theta = \frac{2E_{x0}E_{y0}}{E_{x0}^2 + E_{y0}^2}\cos\delta. \tag{2.2}$$

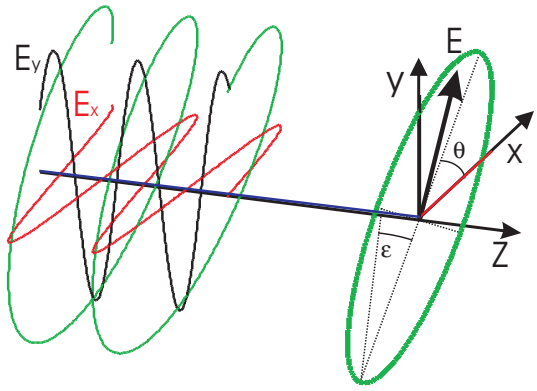

Figure 2.1: *The polarization ellipse. Plotted with phase-shift* $\delta = \pi/3$ *and amplitudes* $E_{x0} = E_{y0}$.

2.2 Partial polarized light and the Mueller-Stokes calculus

George Gabriel Stokes stated in 1852 [18] that any mixture of incoherent polarized light can be fully determined by four parameters,*

$$\mathbf{s} = \begin{bmatrix} s_0 \\ s_1 \\ s_2 \\ s_3 \end{bmatrix} = \begin{bmatrix} I_0 + I_{90} \\ I_0 - I_{90} \\ I_{45} - I_{-45} \\ I_R - I_L \end{bmatrix} = \begin{bmatrix} < E_{x0}^2 > + < E_{y0}^2 > \\ < E_{x0}^2 > - < E_{y0}^2 > \\ 2 < E_{x0} E_{y0} \cos(\delta) > \\ 2 < E_{x0} E_{y0} \sin(\delta) > \end{bmatrix} \tag{2.3}$$

The intensity measurements I, refer to common polarization states, $<>$ corresponds to a time-average of the associated electric field components and δ the phase shift.† The Stokes parameters are related to the ellipticity and azimuth angle for fully polarized light [17],

$$\mathbf{s} = s_0 \begin{bmatrix} 1 \\ \cos(2\epsilon)\cos(2\theta) \\ \cos(2\epsilon)\sin(2\theta) \\ \sin(2\epsilon) \end{bmatrix}. \tag{2.4}$$

Henri Poincaré found that the Stokes parameters can be geometrically represented

*This was the first successful mathematical description of partial polarized light. Previous attempts tried to describe partial polarized light by using electric field amplitudes without success.

†Other notation use $[I, M, S, C]$, $[P1, P2, P3, P4]$ or $[I, Q, U, V]$ to describe the Stokes parameters. Some authors also use different ordering of the Stokes elements [19].

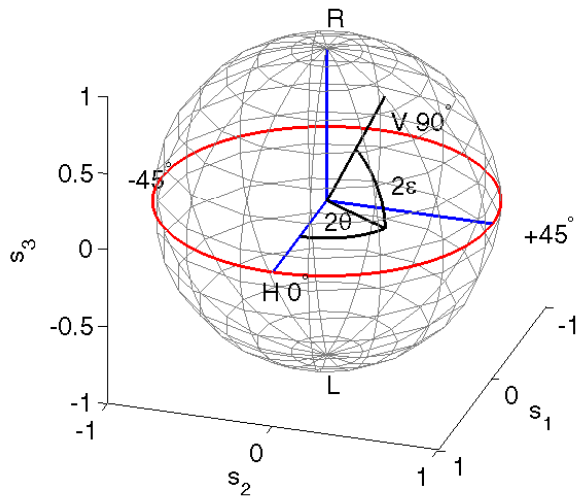

Figure 2.2: *The Stokes vector can be projected onto a surface called the Poincaré sphere. Its location is determined by the azimuth and ellipticity angle θ and ϵ. Partially polarized states can be described by using the degree of polarization P as radius.*

by a sphere [20]. The surface of the Poincaré sphere can be drawn by using s_1, s_2, s_3 as a Cartesian coordinate system [‡], see Figure 2.2. For fully polarized light $s_0 = \sqrt{s_1^2 + s_2^2 + s_3^2}$. This is not true for partially polarized light. Instead an important metric, the degree of polarization P [21],

$$P = \frac{\sqrt{s_1^2 + s_2^2 + s_3^2}}{s_0}, \tag{2.5}$$

is used. Partially polarized states can also be represented within the Poincaré sphere by using P as the radius. In this representation totally unpolarized light is collapsed into the origin of the sphere [21]. A general polarization state can then be described by $\mathbf{s} = [1, P\cos(2\epsilon)\cos(2\theta), P\cos(2\epsilon)\sin(2\theta), P\sin(2\epsilon)]^T$ [17]. Paul Soleillet [22] and Francis Perrin [23] described linear algebraic relations how to transfer a polarization state interacting with materials to another state using the Stokes formalism. This linear relation was later put into matrix form by Hans Mueller [24]. The physically realizable transfer matrix $\mathbf{M}$ is today known as the

[‡]This coordinate system is related to the polar coordinates (r, θ, ϕ) by $(1, \pi/2 - 2\epsilon, 2\theta)$ [21].

Mueller matrix[§].

$$\mathbf{s}' = \mathbf{M} \cdot \mathbf{s}$$
$$\begin{bmatrix} s'_0 \\ s'_1 \\ s'_2 \\ s'_3 \end{bmatrix} = \begin{bmatrix} m_{11} & m_{12} & m_{13} & m_{14} \\ m_{21} & m_{22} & m_{23} & m_{24} \\ m_{31} & m_{32} & m_{33} & m_{34} \\ m_{41} & m_{42} & m_{43} & m_{44} \end{bmatrix} \cdot \begin{bmatrix} s_0 \\ s_1 \\ s_2 \\ s_3 \end{bmatrix} \tag{2.6}$$

Here $\mathbf{s}'$ is the resulting column vector of Stokes parameters upon interaction between a sample associated with the Mueller matrix $\mathbf{M}$, with some incoming light's Stokes vector $\mathbf{s}$. Consequently, any optical system's Mueller matrix $\mathbf{M}_{sys}$, which is constructed by a succession of optical components, can be directly calculated by multiplication of the Mueller matrices of the sub-components or layers, as the light propagate from 1 to N.

$$\mathbf{M}_{sys} = \mathbf{M}_N \mathbf{M}_{N-1} \cdots \mathbf{M}_1. \tag{2.7}$$

The Mueller matrices for standard components have been derived [1, 15], for convenience some specific matrices used in this thesis are described below.

The Mueller matrix of a homogenous diattenuating retarder

A diattenuating sample, or diattenuator, experiences differences in absorption between the two principal axes, while a retarder experiences difference in phase $\delta_c = \delta_s - \delta_f$ with one axis being slow (s) and the other fast (f) (*i*.e. $\delta_s > \delta_f$). A sample, where the eigenpolarization states of the retarder are aligned with the eigenpolarization states of the diattenuator, is referred to as homogenous [15]. A homogenous diattenuating retarder has the following Mueller matrix

$$\mathbf{M}_{diat}(T, \delta, \psi) = T \begin{bmatrix} 1 & \cos 2\psi & 0 & 0 \\ \cos 2\psi & 1 & 0 & 0 \\ 0 & 0 & \sin 2\psi_c \cos \delta_c & \sin 2\psi_c \sin \delta_c \\ 0 & 0 & -\sin 2\psi_c \sin \delta_c & \sin 2\psi_c \cos \delta_c \end{bmatrix}. \tag{2.8}$$

Here $\tan \psi e^{-i\delta_c} = \tan(\frac{T_s}{T_p}) e^{-i(\delta_s - \delta_f)}$, and T_f and T_s are the transmission coefficient of the matrix' fast and slow axis. $T = \frac{|T_f|^2 + |T_s|^2}{2}$ is the transmission coefficient for unpolarized light. Note that this matrix also can describe a pure diattenuator ($\delta_c = 0$) , a pure retarder ($\Psi = \frac{\pi}{4}$), and the identity matrix ($\Psi = \frac{\pi}{4}, \delta_c = 0$).

[§]Often 0-3 indexing are used [17].

The Mueller matrix of a polarizer

One extreme case of a diattenuator is an ideal polarizer which only transmitt one polarization state. The Mueller matrix of Eq.2.8 can then be reduced to

$$\mathbf{M}_{pol} = \frac{\tau}{2}\begin{bmatrix} 1 & 1 & 0 & 0 \\ 1 & 1 & 0 & 0 \\ 0 & 0 & 0 & 0 \\ 0 & 0 & 0 & 0 \end{bmatrix}, \tag{2.9}$$

where τ is the transmission coefficient.

The Mueller matrix of an isotropic reflecting surface

The reflection of an electrometric light-wave at an interface between two isotropic media can be accurately described by the Fresnel complex reflection coefficients R_p and R_s. The Mueller matrix $\mathbf{M}_{ref}$ for such a reflecting surface has an identical form as that of a homogenous diattenuating retarder in Eq.2.8,

$$\mathbf{M}_{ref} = \tau\begin{bmatrix} 1 & -\cos 2\psi & 0 & 0 \\ -\cos 2\psi & 1 & 0 & 0 \\ 0 & 0 & \sin 2\psi\cos\Delta & \sin 2\psi\sin\Delta \\ 0 & 0 & -\sin 2\psi\sin\Delta & \sin 2\psi\cos\Delta \end{bmatrix}, \tag{2.10}$$

where $\frac{R_p}{R_s} = \tan\psi e^{i\Delta} = \tan(\frac{r_p}{r_s})e^{i(\Delta_p - \Delta_s)}$. Δ is the altered phase difference between the $s-$ and $p-$polarization and $\tan\psi$ is the absolute value of the ratio between the real r_s and r_p reflection coefficients. $\tau = \frac{|r_p|^2+|r_s|^2}{2}$ is the reflection coefficient for unpolarized light.

Optical Rotation and rotation of coordinate systems

Rotation of the electromagnetic field vector around the axis of propagation can be described by the Mueller matrix $\mathbf{R}$,

$$\mathbf{R}(\theta) = \begin{bmatrix} 1 & 0 & 0 & 0 \\ 0 & \cos(2\theta) & \sin(2\theta) & 0 \\ 0 & -\sin(2\theta) & \cos(2\theta) & 0 \\ 0 & 0 & 0 & 1 \end{bmatrix}. \tag{2.11}$$

$\mathbf{R}$ is also used to transform between coordinates systems rotated around the axis of light propagation. A Mueller matrix $\mathbf{M}(\theta)$ which has been rotated an angle θ, is given by

$$\mathbf{M}(\theta) = \mathbf{R}(-\theta)\mathbf{M}\mathbf{R}(\theta). \tag{2.12}$$

2.3 Alternative descriptions of polarized light

The Mueller-Stokes calculus is not unique, but it is the most complete description of polarized light available [21]. However, it has some limitations compared with other approaches. First of all, absolute phase information of the light is not retained, as it is based on intensities instead of amplitudes. Alternative representations such as the Jones calculus [21, 25, 26] or the cross-spectral density matrix of Wolf [27], must be used in order to describe interference phenomena. The Stokes vector is also constructed by a non-orthogonal vector space which complicates the matrix algebra.

The Jones calculus [25, 26] defines the amplitudes and phases of the electric field components in a vector $\mathbf{E}$ and optical interactions using 2×2 transfer matrices $\mathbf{J}$,

$$\begin{gathered}\mathbf{E}' = \mathbf{J}\mathbf{E} \\ \begin{bmatrix} E'_x \\ E'_y \end{bmatrix} = \begin{bmatrix} a & b \\ c & d \end{bmatrix} \begin{bmatrix} E_x \\ E_y \end{bmatrix}.\end{gathered} \tag{2.13}$$

This calculus is equivalent to the Mueller calculus when describing fully polarized light, but can not describe any depolarizing effects. Another popular description of partially polarized light is the density matrix formalism [28] ¶. In the density matrix calculus correlations between the electric fields components of the light are calculated and presented in 2×2 matrix form. The density matrix is a Hermitian matrix defined as the direct product of the Jones vector with its Hermitian adjoint,

$$\mathbf{J}_M = \begin{bmatrix} < E_x E_x^* > & < E_x E_y^* > \\ < E_y E_x^* > & < E_y E_y^* > \end{bmatrix} \begin{bmatrix} J_{xx} & J_{xy} \\ J_{yx} & J_{yy} \end{bmatrix}. \tag{2.14}$$

The brackets denote averaging over many wave cycles. Among the three most known representations are that of Wiener, Barakat [29] and Wolf [30]. The Stokes vector and the density matrices contain the same information and are simple linear combination of each other. When rewriting the density matrix as a vector $\mathbf{J}_M^{4\times1}$ the transformation is carried out using [17, 21, 31],

$$\begin{gathered}\mathbf{s} = \mathbf{A}\mathbf{J}_M^{4\times1}, \\ \begin{bmatrix} s_0 \\ s_1 \\ s_2 \\ s_3 \end{bmatrix} = \begin{bmatrix} 1 & 0 & 0 & 1 \\ 1 & 0 & 0 & -1 \\ 0 & 1 & 1 & 0 \\ 0 & i & -i & 0 \end{bmatrix} \begin{bmatrix} J_{xx} \\ J_{xy} \\ J_{yx} \\ J_{yy} \end{bmatrix}.\end{gathered} \tag{2.15}$$

¶Also known as the polarization matrix calculus or coherency matrix calculus. We have chosen to use the density matrix name in order to avoid confusion with the Hermitian 4×4 coherency matrices of Simon and Cloude.

A 4×4 density transfer matrix $\mathbf{F}_J$ can be constructed from Eq.2.14 [17]

$$\mathbf{F}_J = \mathbf{J} \otimes \mathbf{J}^* = \begin{bmatrix} aa^* & ab^* & ba^* & bb^* \\ ac^* & ad^* & bc^* & bd^* \\ ca^* & cb^* & da^* & db^* \\ cc^* & cd^* & dc^* & dd^* \end{bmatrix}. \tag{2.16}$$

$\otimes$ is the Kronecker product. $\mathbf{F}_J$ can be directly related to the Mueller-Stokes formalism using Eq. 2.15

$$\mathbf{M}_J = \mathbf{A}\mathbf{F}_J\mathbf{A}^{-1} \tag{2.17}$$

$$= \frac{1}{2}\begin{bmatrix} aa^* + cc^* + bb^* + dd^* & aa^* + cc^* - bb^* - dd^* & ab^* + cd^* + ba^* + dc^* & -i(ab^* + cd^*) + ba^* - dc^*) \\ aa^* - cc^* + bb^* - dd^* & aa^* - cc^* - bb^* + dd^* & ab^* - cd^* + ba^* - dc^* & -i(ab^* - cd^* - ba^* + dc^*) \\ ac^* + ca^* + bd^* + db^* & ac^* + ca^* - bd^* - db^* & ad^* + cb^* + bc^* + da^* & -i(ad^* + cb^* - bc^* - da^*) \\ i(ac^* - ca^* + bd^* - db^*) & i(ac^* - ca^* - bd^* + db^*) & i(ad^* - cb^* + bc^* - da^*) & ad^* - cb^* - bc^* + da^* \end{bmatrix}. \tag{2.18}$$

$\mathbf{M}_J$ is called a Mueller-Jones matrix due to the direct relation between the Mueller matrix and Jones matrix. Barakat and Anderson stated the set of conditions when a Mueller matrix can be defined by a Jones matrix, *i.e.* when it is a Mueller-Jones matrix [32]. They also showed how a non-Mueller-Jones matrix can be approximated to its nearest complementary Jones matrix, see 4.1.1. Barakat and Anderson used Simons definition for the coherency matrix [33] in order to establish the Hermitian matrix.

When using 2×2 transfer matrices the density formalism is unable to describe depolarizing samples like the Mueller-Stokes calculus [21]. The coherency matrix is also harder to visualize than the Stokes vector. For more information about the coherency matrix, see [21, 28, 29]. Non of the described calculi changes the state of polarization as the wave propagates.

3 Polarimeters

This chapter describes how to measure the interaction between polarized light and a sample using the 4×4 Mueller matrix. Such an instrument is either referred to as a Mueller matrix polarimeter or a Mueller Matrix Ellipsometer (MME) depending on the author or research field. The Mueller matrix depends on wavelength, angle of incident and location on the sample [15]. In the following these will be assumed fixed for simplicity.

3.1 General approach

A polarimeter consists of five basic parts; a light source, a Polarization State Generator (PSG), a sample, a Polarization State Analyzer (PSA) and a detector, see Figure 3.1. Basically, the Mueller matrix of a sample is found by probing it with a

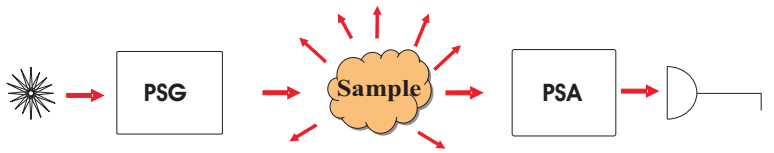

Figure 3.1: *Simplified sketch of the basic components of a polarimeter; source, Polarization State Generator (PSG), sample, Polarization State Analyzer (PSA) and detector.*

set of appropriate polarization states, controlled by the PSG, and then analyzing the altered polarization state with the PSA. At least four intensity measurements are required to determine a single Stokes vector [34]. To find all 16 Mueller matrix elements a minimum of four probing states are needed for each Stokes vector measurement [15]. In most setups both the PSA and PSG have an anti-symmetric ordering and use the same optical components. A variety of possible technical solutions exist, such as systems based on photo-elastic modulators [35], electro-optical modulators [36–38], Pockel's cells [39,40], liquid crystals [37,41,42], rotating prisms retarders or wave plates [43, 44]. The PSA and PSG can either be based on a fixed set or based on continuous modulation of the polarization states. Continuous modulation like photo-elastic modulators can operate very fast, but requires

complicated demodulation techniques. The thesis will focus on non-modulating techniques using a fixed set of polarization states, as it simplifies the acquisition and reduces the overall cost considerably. Two different systems have been designed, built and evaluated: one system based on dual rotating prism retarders (Paper I and II), and a second system based on Ferro-electric Liquid Crystal (FLC) and fixed waveplates (Paper III). In both systems a single intensity matrix $\mathbf{B}$ is collected. $\mathbf{B}$ depends on both the Mueller matrix of the sample $\mathbf{M}$, and the system's generating and analyzing matrices $\mathbf{W}$ and $\mathbf{A}$,

$$\mathbf{B} = \mathbf{AMW}. \tag{3.1}$$

$\mathbf{M}$ is found by inverting the matrices $\mathbf{A}$ and $\mathbf{W}$ and form

$$\mathbf{M} = \mathbf{A}^{-1}\mathbf{B}\mathbf{W}^{-1}. \tag{3.2}$$

Theoretical expressions for the generating matrix $\mathbf{W}$ and analyzing matrix $\mathbf{A}$ are not needed in practical implementations, as they can be found by calibration, see Section 3.5. However, explicit expressions are needed when optimizing performance.

3.2 General expressions for the system matrices

The system matrices $\mathbf{A}$ and $\mathbf{W}$ are not Mueller matrices, but constructed by a set of probing Stokes vectors $\{\mathbf{w}\}$ and a set of analyzing states $\{\mathbf{a}\}$. Each vector $\mathbf{w_i}$ in $\{\mathbf{w}\}$ can be found by multiplying the polarization state generator's Mueller matrix $\mathbf{M}_{PSG_i}$ in state i with the Stokes vector for unpolarized light $\mathbf{s}_{unpol} = [1, 0, 0, 0]^T$,

$$\mathbf{w}_i = \mathbf{M}_{PSG_i} \cdot \mathbf{s}_{unpol}. \tag{3.3}$$

If four probing states are used, $\mathbf{W}$ is given by

$$\mathbf{W} = [\mathbf{w}_1, \mathbf{w}_2, \mathbf{w}_3, \mathbf{w}_4]. \tag{3.4}$$

Similarly, an analyzing matrix $\mathbf{A}$ can be defined for each analyzing state $\mathbf{a}_j$, given by the first row of the PSA's Mueller matrix $\mathbf{M}_{PSA_j}$ in state j.

$$\mathbf{a}_j = [1, 0, 0, 0] \cdot \mathbf{M}_{PSA_j}. \tag{3.5}$$

A 4×4 analyzing matrix $\mathbf{A}$ can then be constructed*,

$$\mathbf{A} = \begin{bmatrix} \mathbf{a}_1 \\ \mathbf{a}_2 \\ \mathbf{a}_3 \\ \mathbf{a}_4 \end{bmatrix}. \tag{3.6}$$

Each element $b_{i,j}$ in $\mathbf{B}$ can now be measured, and the Mueller matrix of the sample retracted. $\mathbf{A}$ and $\mathbf{W}$ can also be constructed using more than four states resulting in $n \times 4$ and $4 \times m$ matrices.

3.3 Specific expressions for the system matrices

Each of the two experimental systems in this thesis uses rotated retarders having Mueller matrices of the form $\mathbf{M}_{ret}(\theta, \delta)$ given by Eq. 2.12 and 2.8:

$$\mathbf{M}_{ret}(\theta, \delta) = \mathbf{M}_{rot}(\theta)^{-1}\mathbf{M}_{ret}(\delta)\mathbf{M}_{rot}(\theta)$$

$$= \begin{bmatrix} 1 & 0 & 0 & 0 \\ 0 & (\cos(2\,\theta))^2 + (\sin(2\,\theta))^2 \cos(\delta) & \cos(2\,\theta)\sin(2\,\theta) - \sin(2\,\theta)\cos(\delta)\cos(2\,\theta) & -\sin(2\,\theta)\sin(\delta) \\ 0 & \cos(2\,\theta)\sin(2\,\theta) - \sin(2\,\theta)\cos(\delta)\cos(2\,\theta) & (\sin(2\,\theta))^2 + (\cos(2\,\theta))^2 \cos(\delta) & \cos(2\,\theta)\sin(\delta) \\ 0 & \sin(2\,\theta)\sin(\delta) & -\cos(2\,\theta)\sin(\delta) & \cos(\delta) \end{bmatrix}, \tag{3.7}$$

with $\psi_c = \frac{\pi}{4}$ and $T = 1$.

3.3.1 The compensator based Mueller matrix ellipsometer

The ellipsometer of Paper II is based on Azzam's dual rotating compensator setup [43]. † The compensators are specially designed Fresnel bi-prisms where the retardation is created by four internal reflections, see Paper I. The PSG and PSA designs are realized by combining a linear polarizer with a compensator rotated at angle θ from the transmission axis of the polarizer, see Figure 3.2. The resulting Mueller matrix $\mathbf{M}_{PSG}$ for the PSG is given by

$$\mathbf{M}_{PSG}(\theta, \delta) = \mathbf{M}_{ret}(\theta, \delta)\mathbf{M}_{pol}$$

*Note that the elements in $\{\mathbf{a}\}$ are row vectors and $\{\mathbf{w}\}$ are column vectors.

†Azzam uses continuous modulation of the compensators at an 1:5 ratio and finds the Mueller elements by Fourier analysis. In this thesis the elements are found by using fixed angular positions instead of continuous rotation.

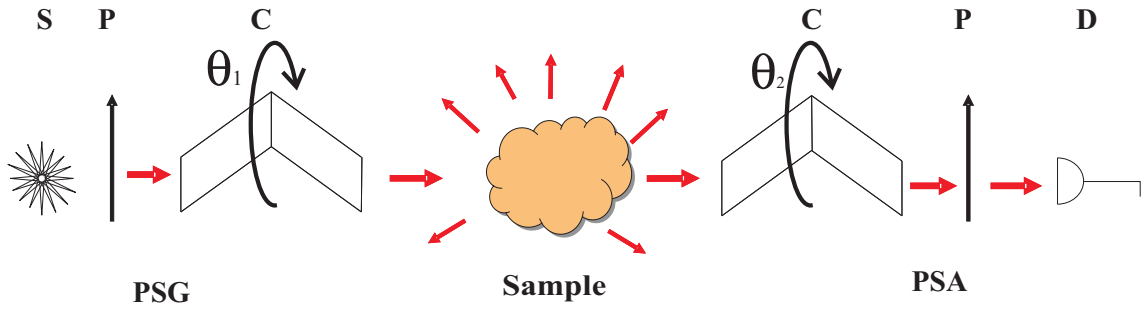

Figure 3.2: *The optical components of the Fresnel bi-prism setup. (S) Source, (P) Polarizer, (C) Compensator, (D) Detector.*

$$= \begin{bmatrix} 1 & 1 & 0 & 0 \\ (\cos(2\theta))^2 + (\sin(2\theta))^2 \cos(\delta) & (\cos(2\theta))^2 + (\sin(2\theta))^2 \cos(\delta) & 0 & 0 \\ \cos(2\theta)\sin(2\theta) - \sin(2\theta)\cos(\delta)\cos(2\theta) & \cos(2\theta)\sin(2\theta) - \sin(2\theta)\cos(\delta)\cos(2\theta) & 0 & 0 \\ \sin(2\theta)\sin(\delta) & \sin(2\theta)\sin(\delta) & 0 & 0 \end{bmatrix}. \tag{3.8}$$

Each rotation angle θ_i creates a vector state in $\{\mathbf{w}\}$. The Mueller matrix of the PSA $\mathbf{M}_{PSA}$ can be constructed with the opposite ordering of the optical elements[‡],

$$\mathbf{M}_{PSA} = \mathbf{M}_{pol}\mathbf{M}_{ret}(\theta, \delta)$$

$$= \begin{bmatrix} 1 & \cos^2(2\theta) + \sin^2(2\theta)\cos(\delta) & \cos(2\theta)\sin(2\theta) - \sin(2\theta)\cos(\delta)\cos(2\theta) & -\sin(2\theta)\sin(\delta) \\ 1 & \cos^2(2\theta) + \sin^2(2\theta)\cos(\delta) & \cos(2\theta)\sin(2\theta) - \sin(2\theta)\cos(\delta)\cos(2\theta) & -\sin(2\theta)\sin(\delta) \\ 0 & 0 & 0 & 0 \\ 0 & 0 & 0 & 0 \end{bmatrix}. \tag{3.9}$$

A realization of a Mueller matrix ellipsometer based on this approach is described in Paper II.

3.3.2 The Ferro-electric liquid crystal based system

A second MME was developed, which was based upon a combination of fixed waveplates and Ferro-electric Liquid Crystals (FLC). FLCs are made out of the smectic C liquid crystals. The molecules are arranged in layers and each molecule layer is aligned at an angle with the layer-normal. The chirality of the molecule introduces a spontaneous dipole moment. This dipole moment is used to control

[‡]Note that if $\delta = \delta_{PSG} = \delta_{PSA}$ then $\mathbf{A} \neq \mathbf{W}^T$ while if $\delta_{PSG} = -\delta_{PSA}$ then $\mathbf{A} = \mathbf{W}^T$.

the liquid crystal by applying an external electric field. Two stable directions of the molecular alignment are possible depending on the direction of the electric field. Since the molecules are birefringent a two-state optical retarder can be constructed. The total retardation is proportional to the crystal thickness.

The FLC-MME was uniquely designed to operate in the near infrared range. A different FLC-MME system for the visible FLC-MME range has been reported by others [45]. The arrangement of the optical components can be viewed in Figure 3.3, and is a variant of the Stokes polarimeter of Gandorfer *et al.* [46]. The Mueller

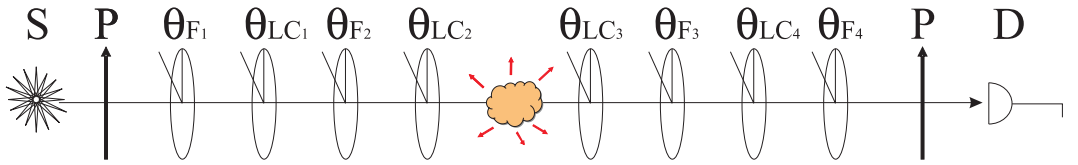

Figure 3.3: *The optical components of the FLC setup. (θ) Rotation angles, (P) Polarizer, (F_i) Fixed waveplate, (LC_i) Ferro-electric liquid crystals, (D) Detector.*

matrix for the PSG, $\mathbf{M}_{FLC_{PSG}}$, can be calculated from

$$\mathbf{M}_{FLC_{PSG}} = \mathbf{M}_{ret}(\theta_{LC_2}, \Delta_{LC_2})\mathbf{M}_{ret}(\theta_{F_2}, \Delta_{F_2})\mathbf{M}_{ret}(\theta_{LC_1}, \Delta_{LC_1})\mathbf{M}_{ret}(\theta_{F_1}, \Delta_{F_1})\mathbf{M}_{pol}, \tag{3.10}$$

since each FLC effectively acts as a fixed waveplate. Similarly, the matrix $\mathbf{M}_{FLC_{PSA}}$ is given by

$$\mathbf{M}_{FLC_{PSA}} = \mathbf{M}_{pol}\mathbf{M}_{ret}(\theta_{F_4}, \Delta_{F_4})\mathbf{M}_{ret}(\theta_{LC_4}, \Delta_{LC_4})\mathbf{M}_{ret}(\theta_{F_3}, \Delta_{F_3})\mathbf{M}_{ret}(\theta_{LC_4}, \Delta_{LC_4}). \tag{3.11}$$

Only the four variables θ_{LC_1},θ_{LC_2},θ_{LC_3} and θ_{LC_4} are influenced during switching of the FLC's creating overall $2^4 = 16$ combined generating and analyzing polarization states. The measured intensity, as the FLC's switch through each step, is effected by the detectors impulse response and the internal movement of the liquid crystal molecules, see Figure 3.4. The intensity vector is cut a length ΔT directly after each step to avoid unstable values. Calculations were performed to find the best place to cut the vector. Figure 3.5 shows the calculated statistical variance for different cut lengths ΔT when sampling at 120 kHz and measuring each step at 1.2 ms. Already after 0.2 ms some stability is obtained. The best stability was found after approximately 0.8 ms. After this the variance increases since the number of remaining sample points of the intensity vector decreases.

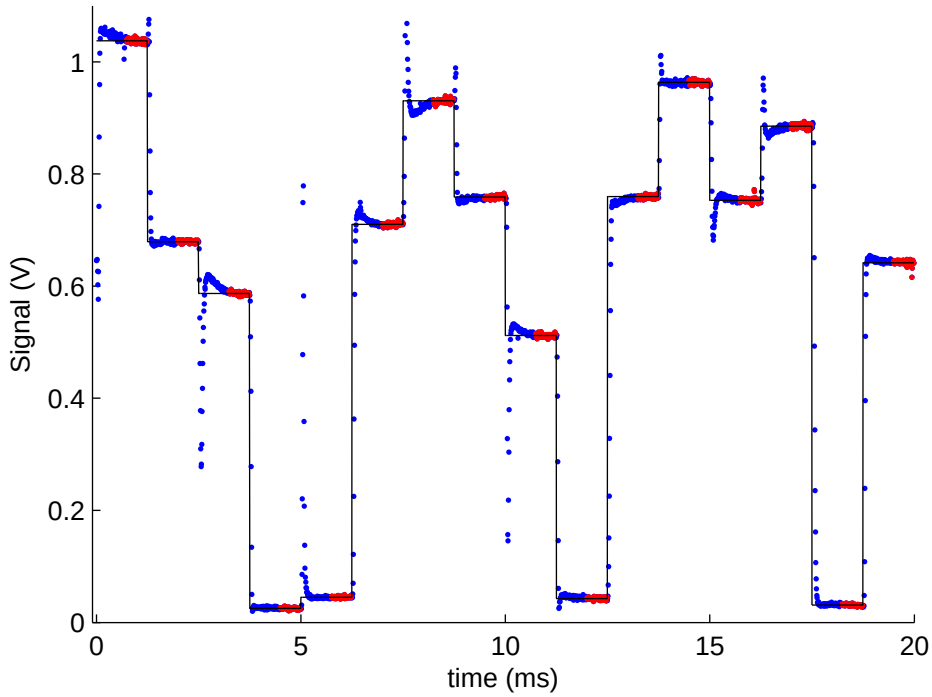

Figure 3.4: *The measured voltage from the InGaAs detector as the crystals switch through each of their 16 steps with the sample position void (blue and red dots). Some points in the vector are removed to avoid the oscillation introduced with each step. Only the last points in the measurements for each step are kept (red dots). The solid black line shows the averaged value of the kept values.*

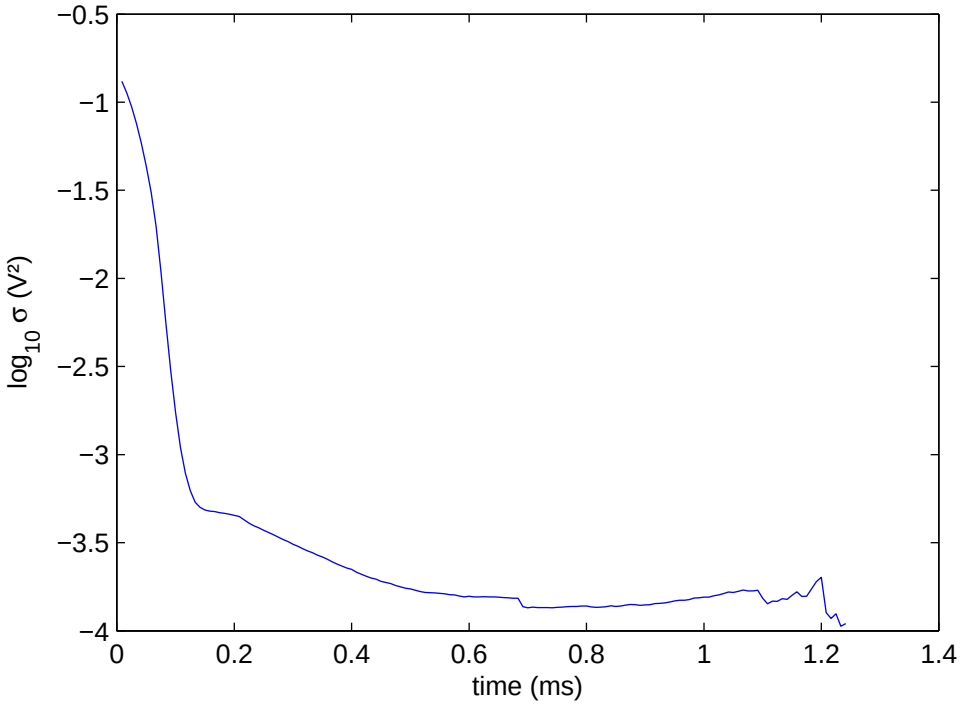

Figure 3.5: *The calculated variance for different cut lengths ΔT when sampling at 120 kHz and measuring each step at 1.2 ms.*

3.4 Optimization of MME performance

The matrix inversion of Eq.3.2 magnifies the measurement noise in $\mathbf{M}$ due to calibration errors $\frac{||\mathbf{\Delta A}||}{||A||}$ and $\frac{||\mathbf{\Delta W}||}{||W||}$, and measurement noise $\left(\frac{||\mathbf{\Delta B}||}{||\mathbf{B}||}\right)$, since

$$\frac{||\mathbf{\Delta M}||}{||\mathbf{M}||} \lesssim \kappa_A \frac{||\mathbf{\Delta A}||}{||\mathbf{A}||} + \kappa_W \frac{||\mathbf{\Delta W}||}{||W||} + \kappa_W \kappa_A \frac{||\mathbf{\Delta B}||}{||\mathbf{B}||}, \tag{3.12}$$

(see the appendix of Paper II for the detailed derivation). κ_W and κ_A are the corresponding matrix condition numbers for $\mathbf{W}$ and $\mathbf{A}$. The condition number is defined by the matrix norm

$$\kappa_A = ||\mathbf{A}||||\mathbf{A}||^{-1}. \tag{3.13}$$

The norm is calculated as the ratio of the largest to the smallest singular value of the matrix [47]. Both systems were optimized by minimization of the system condition numbers in order to minimize effects of errors. Minimizing the condition

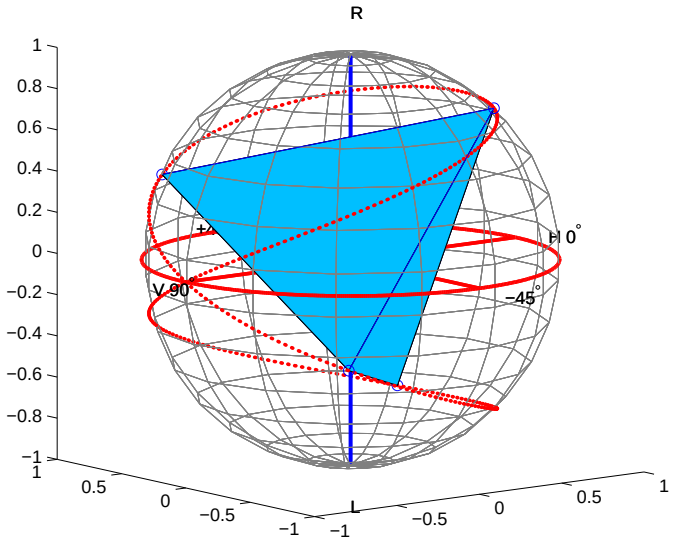

Figure 3.6: *The optimal polarization states create a tetrahedron within the Poincaré sphere. The dotted 8 shaped line represents all the available polarization states with the rotating compensator based PSG [48].*

numbers maximizes the relative importance of each probing Stokes vector and analyzing vector, making them as linearly independent as possible.

The optimization is described in detail in Paper I for the Fresnel Bi-prism system and results of the FLC system's optimization are presented in Paper III. The most optimal states for the rotating compensator system are shown in Figure 3.6.

3.5 Calibration

The calibration routine for the MMEs is based on the procedure suggested by Compain *et al.* [49]. A short description of the calibration process is also given in Paper II and III, but some more details and background are outlined in this section.

The main limitations of the calibration are:

- The forms of the Mueller matrices of the reference samples have to be known.

- The orientation of one of the reference samples must be precisely known.
- Coarse prior knowledge about the other calibration sample orientation is needed.
- The set of reference samples must include at least two samples with sufficiently different Mueller matrices, so that **W** and **A** become uniquely defined.

The calibration routine has several attractive properties:

- The choice of calibration samples does not dependent on **A** or **W**.
- **A** and **W** can be independently determined.
- System simulation is not needed to account for errors.
- All systematic errors are accounted for, as long as the calibration configuration is equal to that of the measurement configuration.

Many different sets of calibration samples can be used. The focus will here be on transmission calibration using two polarizers and a retarder.

A set of intensity matrices $\{\mathbf{B}\}$ accompanying the set of calibration samples $\{\mathbf{M}\}$, together with that of no sample $\mathbf{B}_0$, are measured,

$$\mathbf{B}_0 = \mathbf{AW}, \quad \mathbf{B}_i = \mathbf{AM}_i\mathbf{W}, \quad i = 1, 2, 3. \tag{3.14}$$

Two sets $\{\mathbf{C}\}$ and $\{\mathbf{C}'\}$ are then constructed, with each set defined as

$$\mathbf{C}_i = \mathbf{B}_0^{-1}\mathbf{B}_i = \mathbf{W}^{-1}\mathbf{M}_i\mathbf{W}, \quad i = 1, 2, 3 \tag{3.15}$$

and

$$\mathbf{C}'_i = \mathbf{B}_i\mathbf{B}_0^{-1} = \mathbf{AM}_i\mathbf{A}^{-1}, \quad i = 1, 2, 3. \tag{3.16}$$

$\mathbf{C}_i$ is independent of **A**, and $\mathbf{C}'_i$ is independent of **W**. $\mathbf{C}_i$, $\mathbf{C}'_i$ and $\mathbf{M}_i$ are similar matrices [§] with the same eigenvalues, apart from the introduced random noise [¶]. A sample with both retardation and diattenuation will take a Mueller matrix in the form of that of Eq. 2.8, having two real and two imaginary eigenvalues,

$$\lambda_{R1} = 2\tau\cos^2\psi, \qquad \lambda_{R2} = 2\tau\sin^2\psi, \tag{3.17}$$

$$\lambda_{C1} = \tau\sin 2\psi e^{-i\Delta}, \qquad \lambda_{C2} = \tau\sin 2\psi e^{+i\Delta}. \tag{3.18}$$

[§] If the dimension of **A** and **W** is greater than 4×4, then C' and C are not longer similar matrices. The properties of the calibration samples must then be found by alternative approaches.

[¶] An interesting property of the calibration algorithm is that no calibration is needed when measuring Mueller matrices with known form, as the physical parameter can be found directly from the eigenvalues of **C**.

By associating the eigenvalues of $\mathbf{C}_i$ with the theoretical eigenvalues of $\mathbf{M}_i$, the Mueller matrix of each calibration sample can be reconstructed

$$\tau = \frac{1}{2}\left(\lambda_{R1} + \lambda_{R2}\right), \quad \Delta = \pm\frac{1}{2}\ln\left(\frac{C2}{C1}\right) \tag{3.19}$$

$$\Psi = \arctan\left(\sqrt{\frac{\lambda_{R1}}{\lambda_{R2}}}\right) \text{ or } \Psi = \frac{\pi}{2} - \arctan\left(\sqrt{\frac{\lambda_{R2}}{\lambda_{R1}}}\right). \tag{3.20}$$

Some prior knowledge of the sample is needed, since the choice of all optical parameters is not unique. The transmission τ of a polarizer like that of Eq. 2.9 is

$$\tau = \text{Trace}(\mathbf{M}). \tag{3.21}$$

$\mathbf{W}$ and $\mathbf{X}'$ are found, after reconstructing the set $\{\mathbf{M}\}$, by solving two sets of linear equations

$$\mathbf{M}_i\mathbf{X} - \mathbf{X}\mathbf{C}_i = 0 \tag{3.22}$$

$$\mathbf{X}'\mathbf{M}_i - \mathbf{C}'_i\mathbf{X}' = 0, \tag{3.23}$$

These equations have unique solutions $\mathbf{X} = \mathbf{W}$ and $\mathbf{X}' = \mathbf{A}$. It is convenient to rewrite 3.22 and 3.23,

$$\mathbf{H}_i\mathbf{x} = 0 \tag{3.24}$$

$$\mathbf{H}'_i\mathbf{x}' = 0, \tag{3.25}$$

where $\mathbf{H}_i$ and $\mathbf{H}'_i$ are 16×16 matrices and $\mathbf{x}$ and $\mathbf{x}'$ are 16×1 vectors. In the case of $\mathbf{H}_i$ this is established by first defining

$$\begin{aligned} \mathbf{G}_i^1 &= \mathbf{M}_i\mathbf{U}^{\mathbf{1}} - \mathbf{U}^{\mathbf{1}}\mathbf{C}_i \\ &\vdots \\ \mathbf{G}_i^{16} &= \mathbf{M}_i\mathbf{U}^{16} - \mathbf{U}^{16}\mathbf{C}_i, \end{aligned} \tag{3.26}$$

where

$$\mathbf{U}^1 = \begin{bmatrix} 1 & 0 & 0 & 0 \\ 0 & 0 & 0 & 0 \\ 0 & 0 & 0 & 0 \\ 0 & 0 & 0 & 0 \end{bmatrix}, \mathbf{U}^2 = \begin{bmatrix} 0 & 1 & 0 & 0 \\ 0 & 0 & 0 & 0 \\ 0 & 0 & 0 & 0 \\ 0 & 0 & 0 & 0 \end{bmatrix}, \cdots, \mathbf{U}^{16} = \begin{bmatrix} 0 & 0 & 0 & 0 \\ 0 & 0 & 0 & 0 \\ 0 & 0 & 0 & 0 \\ 0 & 0 & 0 & 1 \end{bmatrix}. \tag{3.27}$$

Each 4×4 matrix $\mathbf{G}_i$ is written into a new 16×1 vector $\mathbf{g}_i$. $\mathbf{K}$ is then constructed from

$$\mathbf{K} = [\mathbf{g}_1, \mathbf{g}_2, \cdots, \mathbf{g}_{16}]. \tag{3.28}$$

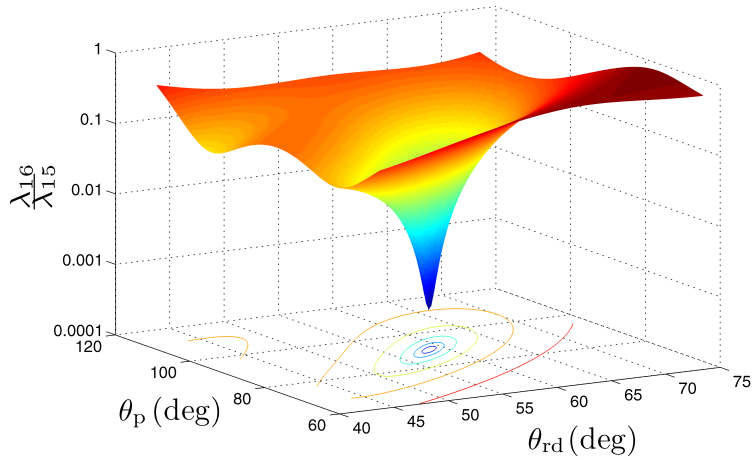

Figure 3.7: *Ratio of the smallest to the second smallest eigenvalue of the matrix K Eq. 3.33, used in the solution for the 16 elements of* $\mathbf{W}$ *and* $\mathbf{A}$.

$\mathbf{K'}_j$ is created similarly starting with Eq 3.23. The over-determined system's least square solution can be found by solving

$$\mathbf{Kx} = 0 \tag{3.29}$$

$$\mathbf{K'x'} = 0, \tag{3.30}$$

where $\mathbf{K}$ and $\mathbf{K'}$ are given by

$$\mathbf{K} = \mathbf{H}_1^T\mathbf{H}_1 + \mathbf{H}_2^T\mathbf{H}_2 + \mathbf{H}_3^T\mathbf{H}_3 \tag{3.31}$$

$$\mathbf{K'} = \mathbf{H'}_1^T\mathbf{H'}_1 + \mathbf{H'}_2^T\mathbf{H'}_2 + \mathbf{H'}_3^T\mathbf{H'}_3. \tag{3.32}$$

Their unique solutions are found for the one eigenvalue equal to zero, with corresponding eigenvectors $\mathbf{w}$ and $\mathbf{a}$. $\mathbf{w}$ and $\mathbf{a}$ are then rewritten into the 4×4 matrices $\mathbf{W'}$ and $\mathbf{A'}$. The retrieved system matrices $\mathbf{W'}$ and $\mathbf{A'}$ are multiplied by an arbitrary constant, since any scalar multiplied with the solution also is a solution of 3.31 and 3.32. Both $\mathbf{A'}$ and $\mathbf{W'}$ are then rescaled with their matrix norms $||\mathbf{A'}||$ and $||\mathbf{W'}||$. This scaling has no practical effect on $\mathbf{M}$, but can be convenient if one likes to compare results from several calibrations (like in Section 3.6).

When noise is present Eq. 3.30 and Eq. 3.32 are unlikely to be zero. The solutions are then found by choosing the eigenvectors which correspond to the smallest eigenvalues λ_{16} and λ'_{16}. The orientation of the calibration sample cannot be found by their matrix eigenvalues, since rotation, defined in Eq.2.12, also produces similar matrices. The matrices $\mathbf{K}$ and $\mathbf{K'}$ in Eq. 3.31 are functions of these angles with eigenvalues $\{\lambda_1(\theta_{pol2}, \theta_{ret}), \ldots, \lambda_{16}(\theta_{pol2}, \theta_{ret})\}$. The set of rotation angles $\{\theta\}$ of the reference samples must be related to the position of one of the

reference samples. In our setups the orientation of first polarizer θ_{pol1} is assumed to be known. λ_{16} will approach zero while the rest are non-zero for the correct values of other calibration samples, in this case θ_{pol2} and θ_{ret} [49]. The values of the angles can then be obtained by minimizing the ratio of the smallest eigenvalue λ_{16} compared to the other non-null eigenvalues of $\mathbf{K}$ and $\mathbf{K}'$,

$$\epsilon_W = \frac{\lambda_{16}}{\sum_{i=1}^{15} \lambda_i}, \quad \epsilon_A = \frac{\lambda'_{16}}{\sum_{i=1}^{15} \lambda'_i}, \tag{3.33}$$

see Figure 3.7. The angles found from ϵ_W and ϵ_A can be different due to noise. Optimization is therefore performed upon the sum of ϵ_W and ϵ_A. When the orientations of the second polarizer θ_{pol2} and the retarder θ_{ret} have been found, the correct rotated Mueller matrices are inserted into Eq. 3.16 and Eq. 3.15, to obtain $\mathbf{A}$ and $\mathbf{W}$.

3.5.1 Choice of reference samples

Compain [49] also stated that the accuracy of the calibration routine is optimal when $\frac{\lambda_{15}}{\lambda_1}$ is at its maximum, (i.e. the ratio between the second smallest and

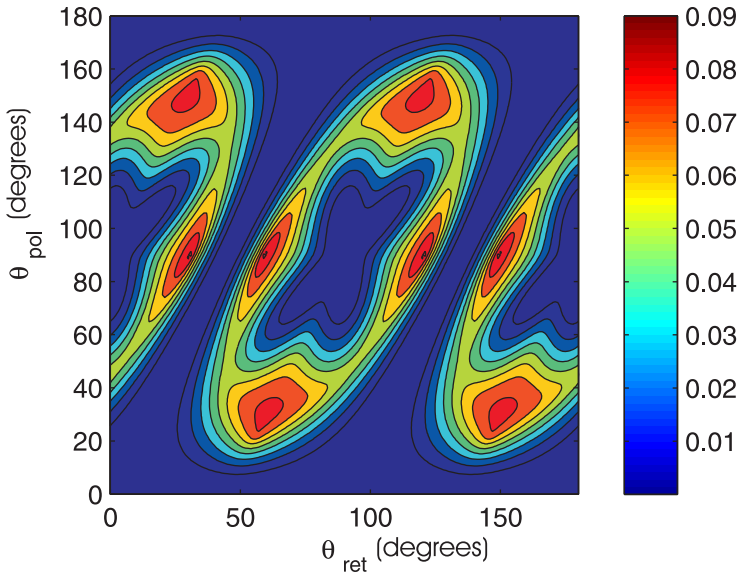

Figure 3.8: *The error estimator $\frac{\lambda_{15}}{\lambda_1}$ for different choices of polarizer orientation θ_{pol} and retardation orientation θ_{ret}.*

the largest eigenvalue), which should ensure good balance among the 15 nonzero

eigenvalues of the matrix $\mathbf{K}$. For the choice of calibration samples, two polarizers and one retarder, this occurs when [50]:

$$\theta_{pol} = 90^\circ \tag{3.34}$$
$$\theta_{ret} = 30.5^\circ \text{ or } 59.5^\circ \tag{3.35}$$
$$\Delta = 109^\circ. \tag{3.36}$$

$\Delta = 132^\circ$ retarders were chosen as calibration samples in our systems, since these already were available. These retarders also have a $\frac{\lambda_{15}}{\lambda_1}$ value similar to that of $\Delta = 109^\circ$. Figure 3.8 shows how the accuracy is altered in the calibration for different choice of polarizer orientations θ_{pol} and retardation orientation θ_{ret} using the achromatic $\Delta = 132^\circ$ retarder. The calibration is best when the error estimator $\frac{\lambda_{15}}{\lambda_1}$ is at its maximum (colored coded in the figure). The optimal orientations of the calibration samples were found to be equal to those found when using a $\Delta = 109^\circ$ retarder.

3.6 Accuracy

38 different calibrations were performed in order to quantify the accuracy of the rotating compensator MME. The data were sampled at 15 kHz acquiring 10000 samples for each intensity measurement $b_{i,j}$, using 473 nm coherent laser illumination. Figure 3.9 shows the resulting Mueller matrix for the Fresnel bi-prism calibration sample **M3**, both when the sample has been part of the calibration, and when using the obtained averaged calibration on multiple measurements. The mean variances $\bar{\sigma}^2$ and mean standard deviations $\bar{\sigma}$, averaged over all the Mueller matrix elements $m_{i,j}$ and calculated for all the calibration $\{\mathbf{M0}, \mathbf{M1}, \mathbf{M2}, \mathbf{M3}\}$, are tabulated in Table 3.1. Calculated values for $\mathbf{A}$ and $\mathbf{M}$ are also shown. The index c in the table is used for the values obtained when **M3** is a part of the calibrations, while the index s is used for values obtained using the averaged system matrices $\mathbf{A}_{avg}$ and $\mathbf{W}_{avg}$. As observed from Figure 3.9 and Table 3.1, the standard deviation of s is almost double to that of c. This is as expected since, in the case of c, each of the system matrices has been optimized to fit individually together with 3 other samples ($\sigma_s \approx \sigma_c/\sqrt{(4)}$). The measurement used in this thesis should be compared against the values of s. The average condition numbers calculated from the calibrations were $\kappa_A = 1.80$ and $\kappa_W = 1.80$, and this leads to a maximum relative error $\frac{||\mathbf{\Delta M}||}{||\mathbf{M}||} \lesssim 1\%$ when using the right hand side of Eq. 3.12 by calculating $\frac{||\mathbf{\Delta A}||}{||\mathbf{A}||} = \frac{||\sum_{i=1}^{n} \mathbf{A}_i - \mathbf{A}_{avg}||}{||\mathbf{A}_{avg}||}$. This value is larger than the average $\frac{||\mathbf{\Delta M}||}{||\mathbf{M}||} = 0.06\%$ calculated from all the samples. This accuracy is only assured when the actual measuring configuration is close to that used in the calibration.

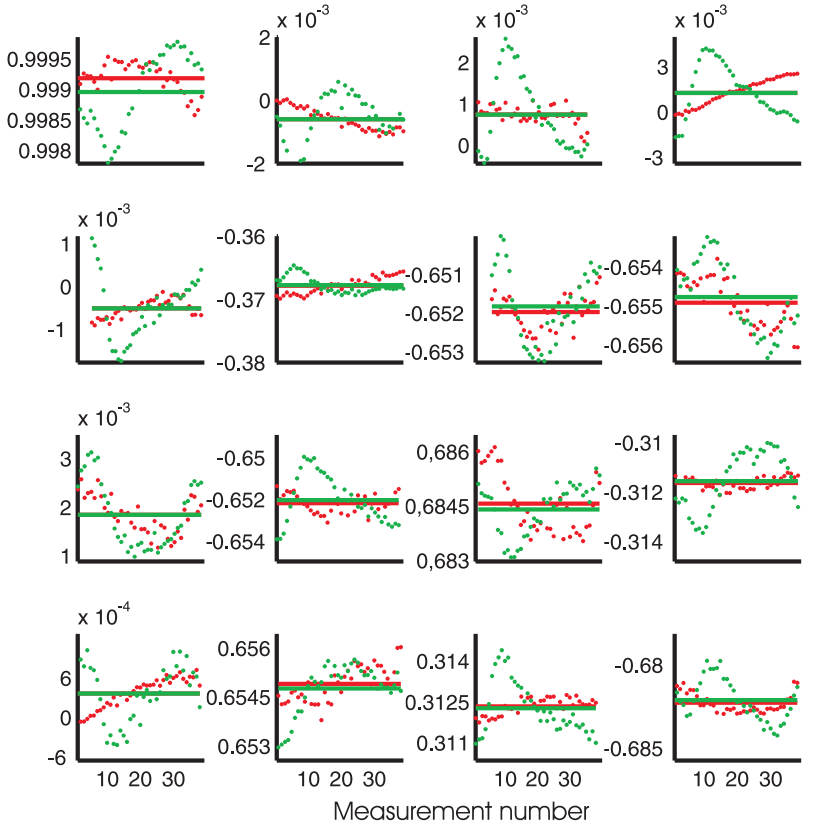

Figure 3.9: *The variation of the Fresnel bi-prism calibration sample M3 when it is a part of the calibration (green) and when using the averaged calibration matrices* $\mathbf{A}_{avg}$ *and* $\mathbf{W}_{avg}$ *on multiple measurements (red).*

Table 3.1: *The calculated standard deviation and variance from the averaged matrix values.*

	A	**W**	$\mathbf{M0}_c$	$\mathbf{M1}_c$	$\mathbf{M2}_c$	$\mathbf{M3}_c$	$\mathbf{M0}_s$	$\mathbf{M1}_s$	$\mathbf{M2}_s$	$\mathbf{M3}_s$
$\bar{\sigma}^2$ (10^{-6})	0.36	0.45	0.071	0.12	0.74	0.33	1.0	0.38	1.5	1.2
$\bar{\sigma}$ (10^{-4})	6.0	6.7	2.7	3.5	8.6	5.8	10.0	6.2	12.3	10.7

4 Analyzing the Mueller matrix

As stated by Chipman: "It is impossible to analyze real arbitrary Mueller matrices without considering three tricky topics: physical realizability, depolarization and inhomogenity" [15] *. Chapter 3 outlined how the Mueller matrix could be measured by different techniques. Here an introduction to how to retrieve physically relevant parameters from measurements will be given. A pre-requisite for reaching between theory and experiments are embedded within the Mueller-Jones formalism. The Jones matrices are constructed from first principles, while the Mueller-Stokes calculus is a phenomenological construction. If the system can be described by a Jones matrix, the system's Mueller-Jones matrix can be directly found using Eq. 2.18. It is also possible to filter an unphysical matrix to its nearest complimentary physically realizable Mueller matrix or Mueller-Jones matrix in order to remove noise or analyze physical properties.

4.1 A physically realizable Mueller matrix

Not all real 4×4 matrices are physically realizable Mueller matrices, see Figure 4.1. Even matrices which transfer a Stokes vector into another Stokes vector (Stokes Matrix) might not be a Mueller matrix [53]. Tests which can determine if a matrix is physically realizable are valuable in order to find computational errors, noise and systematical errors in data collected in measurements.

A Mueller matrix must satisfy two constraints to be physically realizable [8, 54].†

1. **The polarization constraint:**
   The matrix must not over-polarize, *i.e* $\mathbf{M}$ can not produce outgoing Stokes vectors with degree of polarization greater than unity.

2. **The gain constraint:**
   The gain of the matrix must be less than unity, *i.e* $\mathbf{M}$ can not produce

*A Mueller matrix is inhomogeneous if the eigenpolarization states are non-orthogonal. This occur *i.e.* when $\mathbf{p} \neq \mathbf{d}^T$. None of the measured samples in this thesis is inhomogeneous, therefore the discussion around this subject is left to other authors [15, 51, 52].

†Some authors [55] only use the polarization constraint to determine whether a matrix is physically realizable.

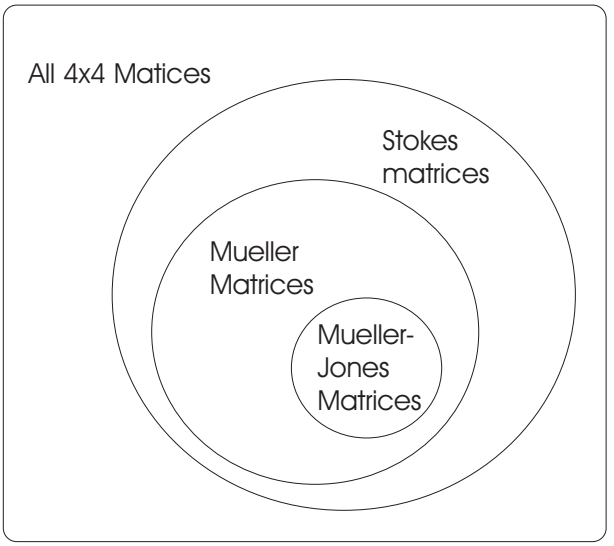

Figure 4.1: *Different domains for* 4×4 *matrices.*

outgoing Stokes vectors with larger intensity than that of the incoming Stokes vector.

Using a set of restricting conditions on sertain linear combinations of **M**'s sub-elements one check if the matrix is physical realizable. Simpler conditions can be made if one chooses to transfer the Mueller matrix to a positive semidefinite coherency matrix [53, 55, 56].

The polarization constraint

Cloude showed that the polarization constraint is satisfied if the sample's 4×4 Hermitian coherency matrix is positive semidefinite. Cloude's coherency matrix is used in Paper II. Here, the coherency matrix of Simon will be discussed [33], since it is unitarily equivalent to Cloude's matrix [53], (*i.e.* has the same eigenvalues) [‡]. The coherency matrix, according to Simon, is equal to [32, 33]

$$\mathbf{H} = \frac{1}{2} \sum_{i=1}^{4} \sum_{j=1}^{4} m_{i,j} \sigma_i \otimes \sigma_j^*, \tag{4.1}$$

[‡]They may not have the same eigenvectors. To the author's experience these two different coherency matrices produce the same numerical results for all tested Mueller matrices when applied in matrix filtering.

where σ_i and σ_j are the Pauli spin matrices

$$\sigma_1 = \begin{bmatrix} 1 & 0 \\ 0 & 1 \end{bmatrix}, \quad \sigma_2 = \begin{bmatrix} 1 & 0 \\ 0 & -1 \end{bmatrix}, \quad \sigma_3 = \begin{bmatrix} 0 & 1 \\ 1 & 0 \end{bmatrix}, \quad \sigma_4 = \begin{bmatrix} 0 & -i \\ i & 0 \end{bmatrix}. \tag{4.2}$$

The Mueller matrix is physically realizable if $\mathbf{H}$ has no negative eigenvalues (the coherency matrix is positive semidefinite). Cloude also defined a system fidelity H_{fid} (dB) [55] to quantify the quality of the measured $\mathbf{M}$,

$$H_{fid} = -10 \log_{10} \frac{\sum \lambda_+}{\sum \lambda_-}, \tag{4.3}$$

where λ_+ and λ_- are the positive and negative eigenvalues of the coherence matrix $\mathbf{H}$. H_{fid} can be used to check the performance of a polarimeter like in Paper II, and help discovering artifacts in measurements like in Section 5.4.

The gain constraint

Cloude's realizability test does not consider gain. The gain constraint is satisfied if [54]

$$g_f = m_{11} + \sqrt{(m_{12}^2 + m_{13}^2 + m_{14}^2)} \leq 1 \tag{4.4}$$

$$g_r = m_{11} + \sqrt{(m_{21}^2 + m_{31}^2 + m_{41}^2)} \leq 1. \tag{4.5}$$

These constraints are also referred to as the forward and backward transmittance constraints. This is specially important for unscaled absolute Mueller matrix measurements containing transmission or reflection information.

4.1.1 Mueller Matrix filtering

Filtering to obtain physical Mueller matrices

The measured matrix $\mathbf{M}$ can be approximated (or filtered) to it's nearest physically correct Mueller matrix $\mathbf{M}'$. $\mathbf{M}$ is filtered by setting all negative eigenvalues in the diagonal matrix $\mathbf{D}$, from a spectral decomposition $\mathbf{H} = \mathbf{V}\mathbf{D}\mathbf{V}^*$ to zero, and multiplying the new eigenvalue matrix $\mathbf{D}'$ with the corresponding eigenvector matrices $\mathbf{V}$. A filtered coherency matrix $\mathbf{H}'$ is then obtained,

$$\mathbf{H}' = \mathbf{V}\mathbf{D}'\mathbf{V}^*. \tag{4.6}$$

$\mathbf{V}^*$ is the conjugate transpose of $\mathbf{V}$. The filtered matrix $\mathbf{H}'$ is thereafter converted back to a filtered Mueller matrix $\mathbf{M}'$, see the end of this section. It has been shown by numerical simulation [57], that the error reduction from this filtering is about 30% for non-depolarizing samples, and 10% for samples with depolarization.

Filtering to get Mueller-Jones matrices

Kostinski showed that a physically realizable Mueller matrix $\mathbf{M}$ can be decomposed into a non-depolarizing Mueller-Jones matrix $\mathbf{M}_J$ and an independent additive depolarizing matrix $\mathbf{M}_{comp}$, when the depolarization is isotropic [58]:

$$\mathbf{M} = \mathbf{M}_J + \mathbf{M}_{comp}. \tag{4.7}$$

More specifically, any physically realizable Mueller matrix $\mathbf{M}$ can be regarded as a combination of four Mueller-Jones matrices [32]:

$$\mathbf{M} = \Sigma_{i=1}^{4} \lambda_i \mathbf{M}_{J_i}. \tag{4.8}$$

Each $\mathbf{M}_{J_i}$ is constructed from the corresponding eigenvector $\mathbf{v}_i$ in $\mathbf{V}$. If the largest eigenvalue λ_1 satisfies $|\lambda_1| \gg \max(|\lambda_2|, |\lambda_3|, |\lambda_4|)$, the matrix $\mathbf{M}$ can be approximated by a single Mueller-Jones matrix by performing filtering. The filtering to a Mueller-Jones matrix can be found by first calculating a filtered Coherency matrix $\mathbf{H_J}$ by

$$\mathbf{H_J}' = \left(\lambda_1 - \frac{d}{2} \mathbf{v_1} \mathbf{v_1}^* \right), \tag{4.9}$$

and then transforming it into a Mueller-Jones matrix [59]. Here $\mathbf{v}_1$ is the eigenvector corresponding to λ_1, and d is given by

$$d = \frac{2}{3}(\lambda_2 + \lambda_3 + \lambda_4). \tag{4.10}$$

Transformation from $\mathbf{H}_J$ to $\mathbf{M}_J$

The coherency matrix $\mathbf{H_J}$ for a Mueller-Jones matrix is calculated using Eq. 4.1 and Eq. 2.18, resulting in

$$\mathbf{H_J} = \begin{bmatrix} |a|^2 & a^*b & a^*c & a^*d \\ b^*a & |b|^2 & b^*c & b^*d \\ c^*a & c^*b & |c|^2 & c^*d \\ d^*a & d^*b & d^*c & |d|^2 \end{bmatrix}, \tag{4.11}$$

which clearly is a Hermitian matrix. $\mathbf{F_J}$ is obtained by comparing Eq. 4.11 with Eq. 2.18. The sub-elements of $\mathbf{H_J}$ are reorganized in the following order:

$$\mathbf{F_J} = \begin{bmatrix} h_{1,1} & h_{1,2} & h_{2,1} & h_{2,2} \\ h_{1,3} & h_{1,4} & h_{2,3} & h_{2,4} \\ h_{3,1} & h_{3,2} & h_{4,1} & h_{4,2} \\ h_{3,3} & h_{3,4} & h_{4,3} & h_{4,4} \end{bmatrix}. \tag{4.12}$$

The Mueller-Jones matrix is calculated using Eq. 2.17. The same transformation is used to transform the filtered $\mathbf{H}'$, Eq. 4.9, back to $\mathbf{M}'$. This is done by first using Eq. 4.12 obtaining a matrix $\mathbf{F}'$, and then using Eq. 2.17 establishing $\mathbf{M}'$.

4.2 Product decomposition

The Mueller matrix contains all polarization effects produced by a sample. They can be summarized by three main effects:

- Depolarization is the ability to create randomly polarized light, i.e. loss of coherence of the incident field.
- Diattenuation is the difference in transmittance or reflectance between orthogonal components of the incident field.
  - Linear dichroism: difference in transmittance or reflectance between the linear components.
  - Circular dichroism: difference in transmittance or reflectance between the circular components.
- Retardance is the shift of phase between orthogonal components of the incident field.
  - Linear retardance: difference in phase between the linear components
  - Optical rotation: difference in phase between the circular components

Lu and Chipman developed a data reduction algorithm for separating these physical properties within the Mueller matrix. This algorithm can be practical when sample modeling is impossible or unpractical to implement. Any arbitrary physical Mueller matrix $\mathbf{M}$, can be divided into uniquely defined product of three simpler matrices, a diattenuation matrix $\mathbf{M}_D$, a retardance matrix $\mathbf{M}_R$ and a pure depolarizing matrix $\mathbf{M}_\Delta$ [60]. Six different possible factor orderings are possible in this decomposition. Devided in two main routines, a forward and reverse product decomposition routine [61–63]. Each routine consists of three equivalent interchangeable orderings using simple orthogonal transformations. The forward decomposition routine corresponds to an optical ordering with the depolarizer being at the end, while the reverse decomposition routine corresponds to an optical ordering with the depolarizer at the front [62, 63]. Consequently, the chosen decomposition should be based on some prior knowledge of the sample in which the depolarization occurs. [§]

[§]A variant of the decomposition routine has also been developed for non-complete 3×3 Mueller matrices [64].

Some physical quantities within the Mueller matrix can be directly found from the matrix elements without performing decomposition. These include the diattenuation vector $\mathbf{d}$, polariance vector $\mathbf{p}$ and depolarization index P_d (defined in Eq. 4.3). A 2×2 short hand notation is often used for convenience:

$$\mathbf{M} = m_{1,1} \begin{bmatrix} 1 & \mathbf{d}^T \\ \mathbf{p} & \mathbb{M} \end{bmatrix} \tag{4.13}$$

$$\mathbf{d} = \frac{[m_{12}, m_{13}, m_{14}]^T}{m_{11}} \tag{4.14}$$

$$\mathbf{p} = \frac{[m_{21}, m_{31}, m_{41}]^T}{m_{11}}. \tag{4.15}$$

$\mathbb{M}$ is the 3×3 lower right sub-matrix of $\mathbf{M}$, and $\mathbf{d}$ and $\mathbf{p}$ are 3×1 vectors. The length of $\mathbf{p}$ is recognized as the degree of polarization for completely unpolarized incoming light. The length d of $\mathbf{d}$ is the absolute difference in transmission T_q and T_r scaled by its sum, i.e.

$$d = \frac{|T_q - T_r|}{T_q + T_r}, \tag{4.16}$$

for the Mueller matrix eigenpolarization states q and r. For isotropic reflective surfaces, this equals to the difference in the reflectance between the $s-$ and $p-$polarizations.

The focus will here be only on the forward decomposition. It has the following ordering of the sub-matrices [60],

$$\mathbf{M} = m_{11}\mathbf{M}_\Delta\mathbf{M}_R\mathbf{M}_D, \tag{4.17}$$

with the form ¶,

$$\mathbf{M}_D = \begin{bmatrix} 1 & \mathbf{d}^T \\ \mathbf{d} & \mathbb{M}_D \end{bmatrix}, \qquad \mathbf{M}_R = \begin{bmatrix} 1 & \mathbf{0}^T \\ \mathbf{0} & \mathbb{M}_R \end{bmatrix}, \qquad \mathbf{M}_\Delta = \begin{bmatrix} 1 & \mathbf{0}^T \\ \mathbf{p}_\Delta & \mathbb{M}_\Delta \end{bmatrix}. \tag{4.18}$$

The first step of the forward decomposition is to construct the diattenuating matrix $\mathbf{M}_D$ by finding the sub-matrix $\mathbb{M}_D$, which is given by

$$\mathbb{M}_D = \sqrt{1 - d^2}\mathbf{I} + (1 - \sqrt{1 - d^2})\hat{\mathbf{d}}\hat{\mathbf{d}}^T, \tag{4.19}$$

where I is the 3×3 identity matrix and $\hat{\mathbf{d}} = \mathbf{d}/|\mathbf{d}|$. The contribution from the diattenuation can then be removed from the original Mueller matrix $\mathbf{M}$ by inversion,

$$\mathbf{M}' = \mathbf{M}\mathbf{M}_D^{-1} = \mathbf{M}_\Delta\mathbf{M}_R \tag{4.20}$$

$$= \begin{bmatrix} 1 & \mathbf{0}^T \\ \mathbf{p}_\Delta & \mathbb{M}_\Delta\mathbb{M}_R \end{bmatrix} = \begin{bmatrix} 1 & \mathbf{0}^T \\ \mathbf{p}_\Delta & \mathbb{M}' \end{bmatrix}. \tag{4.21}$$

¶The reverse decomposition routine uses a slightly different form of the sub-matrices, see [62] for a detailed discussion.

Two new sub-matrices can now be constructed:

$$\mathbb{M}_R = \frac{1}{\sqrt{1-d^2}}(\mathbb{M} - (1-\sqrt{1-d^2}\hat{\mathbf{p}}\hat{\mathbf{d}}^T) \tag{4.22}$$

and

$$\begin{aligned}\mathbb{M}_\Delta = \pm(&\mathbb{M}'\mathbb{M}'^T \\ &+ (\sqrt{\lambda_1\lambda_2} + \sqrt{\lambda_2\lambda_3} + \sqrt{\lambda_3\lambda_1})\mathbf{I})^{-1}(\sqrt{\lambda_1} + \sqrt{\lambda_2} + \sqrt{\lambda_3})\mathbb{M}'\mathbb{M}'^T \\ &+ \sqrt{\lambda_1\lambda_2\lambda_3}\mathbf{I}),\end{aligned} \tag{4.23}$$

from which $\mathbf{M}_R$ and $\mathbf{M}_\Delta$ in Eq. 4.18 are found. λ_1, λ_2 and λ_3 are the eigenvalues of the matrix product $\mathbb{M}'(\mathbb{M}')^T$. The sign is given by the sign of the determinant of $\mathbb{M}'$. If the overall determinant of $\mathbf{M}$ is negative, a more general form of Eq. 4.23 must be used [65]. The polariance vector of $\mathbf{M}'$, $\mathbf{p}_\Delta$, is given by

$$\mathbf{p}_\Delta = \frac{\mathbf{p} - \mathbb{M}\mathbf{d}}{1-D^2}. \tag{4.24}$$

A retardance vector $\mathbf{r} = [1, r_1, r_2, r_3]$ can be defined from sub-elements $m_{R_{i,j}}$ of the decomposed $\mathbf{M}_R$ matrix:

$$\mathbf{r} = \frac{R}{2\sin(R)}\begin{bmatrix} m_{R_{3,4}} - m_{R_{4,3}} \\ m_{R_{4,2}} - m_{R_{2,4}} \\ m_{R_{2,3}} - m_{R_{3,2}} \end{bmatrix}, \tag{4.25}$$

where

$$R = |\mathbf{r}| = \cos^{-1}\left(\frac{\mathrm{Trace}(\mathbf{M}_R) - 1}{2}\right), \tag{4.26}$$

$$\theta = \frac{1}{2}\arctan\left(\frac{r_2}{r_1}\right) = \frac{1}{2}\arctan\left(\frac{m_{R_{4,2}} - m_{R_{2,4}}}{m_{R_{3,4}} - m_{R_{4,3}}}\right). \tag{4.27}$$

Decomposition of the retarding Matrix

The decomposed retardance matrix $\mathbf{M}_R$ can be decomposed further into a product of two sub-matrices, one rotated linear retarder matrix $\mathbf{M}_{LR}$ and one optical rotation matrix $\mathbf{M}_{OR}$ [66],

$$\mathbf{M}_R = \mathbf{M}_{LR}\mathbf{M}_{OR}, \tag{4.28}$$

where

$$\mathbf{M}_{LR} = \begin{bmatrix} 1 & 0 & 0 & 0 \\ 0 & \cos(2\,\theta)^2 + (\sin(2\,\theta))^2 \cos(\delta) & \sin(2\,\theta)\cos(2\,\theta)\,(1-\cos(\delta)) & -\sin(2\,\theta)\sin(\delta) \\ 0 & \sin(2\,\theta)\cos(2\,\theta)\,(1-\cos(\delta)) & \sin(2\,\theta)^2 + (\cos(2\,\theta))^2\cos(\delta) & \cos(2\,\theta)\cos(\delta) \\ 0 & \sin(2\,\theta)\sin(\delta) & -\cos(2\,\theta)\sin(\delta) & \cos(\delta) \end{bmatrix}, \quad (4.29)$$

$$\mathbf{M}_{OR} = \begin{bmatrix} 1 & 0 & 0 & 0 \\ 0 & \cos(2\alpha) & \sin(2\alpha) & 0 \\ 0 & -\sin(2\alpha) & \cos(2\alpha) & 0 \\ 0 & 0 & 0 & \end{bmatrix}. \quad (4.30)$$

The linear retardance δ and optical rotation α are expressed by

$$\delta = 2\cos^{-1}\left[\sqrt{r_3^2\sin^2(\frac{R}{2}) + \cos^2(\frac{R}{2})}\right], \quad (4.31)$$

$$\alpha = \cos^{-1}\left[\frac{\cos(\frac{R}{2})}{\cos(\frac{\delta}{2})}\right]. \quad (4.32)$$

4.3 Depolarization

One of the main reasons to apply the Mueller-Stokes calculus is to study depolarization effects. The depolarization phenomenon usually originates from rapidly varying retardance, diattenuation, multiple reflections, multiple scatterings or are due to spatial integration over an extended sample with varying polarimetric response. There are many ways of quantifying depolarization which easily can lead to confusion. Each of these depolarization metrics is defined in a slightly different manner and thereby has a slightly different interpretation. First of all it is important to know when depolarization is present and quantify its magnitude. In this thesis we have chosen to use the polarization index to quantify the polarization power of the Mueller matrix. In the following section we will relate the polarization index to some other metrics often found in the literature.

When is a Mueller matrix depolarizing?

It has been stated that a necessary [33,67] and sufficent [68] condition for a Mueller matrix $\mathbf{M}$ to be non-depolarizing is

$$\mathbf{Trace}\left(\mathbf{M}^T\mathbf{M}\right) = \sum_{i,j=1}^{4} m_{i,j}^2 = 4m_{11}^2. \quad (4.33)$$

This statement is only correct for a physical Mueller matrix [54], *i.e.* when the eigenvalues of the corresponding coherency matrix are non-negative.

The depolarization index

The depolarization index or degree of purity P_d, is defined by [69]

$$P_d = \sqrt{\frac{\sum_{i,j=1}^{4} m_{i,j}^2 - m_{1,1}^2}{3m_{1,1}^2}} \begin{cases} 1, & \text{Completely polarized} \\ 0, & \text{Completely depolarized} \end{cases}$$

and measures the deviation from Eq 4.33. Its magnitude describes the Euclidian distance for how close $\mathbf{M}$ is to the set of non-depolarizing Mueller matrices [15]. P_d is closely related but not equivalent to another definition of depolarization, namely the Average Degree of Polarization.

The Average Degree of Polarization

The Average Degree of Polarization (ADoP) is based on a geometrical average of all incoming fully polarized states. It is defined by [70]

$$ADoP = \frac{1}{\pi} \int_0^{\pi} \int_{\pi/4}^{-\pi/4} P(\epsilon, \theta) \cos(2\epsilon) \mathrm{d}\theta \mathrm{d}\epsilon \begin{cases} 0, & \text{Completely polarized} \\ 1, & \text{Completely depolarized,} \end{cases}$$

where P is the degree of polarization, given by Eq. 2.5, for the outgoing Stokes vector $\mathbf{s}'$. Chipman performed a comparison between the average geometrical degree of polarization and the polarization index and found for some cases large discrepancies [70]. Especially for cases where the depolarization acts non-symmetrically, i.e when the diattenuation and polariance vectors are different, i.e. $\mathbf{d} \neq \mathbf{p}$. However, computation of ADoP is much more time consuming than P_D. So in many cases it can be convenient to calculate P_D instead. Note that for $\mathbf{p} = \mathbf{d}$ smaller discrepancies are found. In the same way an average degree of linear and circular polarization, P_L and P_C, can be expressed [71].

Entrophy

As given by Eq. 4.8 any Mueller matrix can be described by a combination of four other Mueller-Jones matrices. The entrophy of the Mueller matrix is an often used disorder parameter and is given by [72, 73]

$$E = -\sum_{i=1}^{4} p_i \log_4(p_i) \begin{cases} 1, & \text{Completely depolarized} \\ 0, & \text{Completely polarized} \end{cases}$$

where $p_i = \frac{\lambda_i}{\sum_{j=1}^{4} \lambda_j}$ and the λ_i are the eigenvalues of the coherency matrix. If the disorder is high the Mueller matrix must be expressed by four Mueller-Jones matrices, while matrices with a low entrophy can be approximated by a smaller number of matrices or even a single matrix.

Relations

The entrophy can be related to the depolarization index for isotropic depolarization [71] ,

$$E_{iso} = -\frac{3P_d + 1}{4} \log_4 \left(\frac{3P_d + 1}{4} \right) - 3\frac{1 - P_d}{4} \log_4 \left(\frac{1 - P_d}{4} \right), \tag{4.34}$$

and for anisotropic depolarization [71],

$$E_{aniso} = E_{iso} - \frac{1}{2m_{00}} \sum_{i=1}^{3} \lambda_i \log_4 \left(\frac{2\lambda_i}{m_{00}(1 - P_d)} \right). \tag{4.35}$$

5 Future applications of Mueller matrix ellipsometry

This chapter will present resently studied MME applications and currently unpublished work. Section 5.1 will give a short introduction to Rayleigh and Mie scattering, which will be used to compare results obtained from scattering measurements on protein aggregates using the rotating compensator setup. Fluorescence Mueller matrix measurements on fluorescein in glycerol and embedded within proteins will be presented and discussed. Section 5.4 present how the FLC setup was extended to an imaging Mueller matrix ellipsometer and give a specific example of how this can be utilized in mechanical stress analysis.

Mueller matrix ellipsometry can be used in many other areas than that discussed throughout this thesis. Some other possible applications are discussed in references [21, 74, 75]. The attached thesis papers also show a few applications of MME which will not be discussed further here.

5.1 Light scattering

5.1.1 Elastic scattering of particles

Gustav Mie originally derived the expressions for elastic scattering of electromagnetic waves by spherical particles. Bohren and Huffman derived these result using the Stokes-Mueller formalism [2]. The scattered field ($\mathbf{E}_{sca}$) during plane wave illumination ($\mathbf{E}_{inc}$) can be related using the transfer Jones matrix (or scattering matrix),

$$\begin{bmatrix} E_{\parallel,sca} \\ E_{\perp,sca} \end{bmatrix} \propto \begin{bmatrix} a & b \\ c & d \end{bmatrix} \begin{bmatrix} E_{\parallel,inc} \\ E_{\perp,inc} \end{bmatrix}. \tag{5.1}$$

$E_\parallel$ and $E_\perp$ are the electric fields parallel and orthogonal to the scattering plane. For optical active particles, b and c are generally different from zero, while being zero for symmetric particles like spheres or cylinders [2]. When $b = c = 0$, the

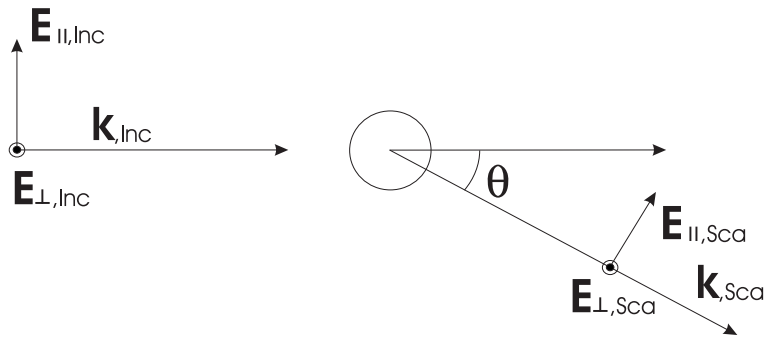

Figure 5.1: *The scattered field ($\mathbf{E}_{sca}$) during plane wave illumination ($\mathbf{E}_{inc}$). $|\mathbf{k}| = |\mathbf{k}_{inc}| = |\mathbf{k}_{sca}|$ is the length for the wave-vector appropriate for the surrounding medium and θ is the scatter angle.*

corresponding Mueller matrix elements, using Eq.2.18, become

$$\begin{aligned} m_{1,1} = m_{2,2} &= \frac{1}{2}\left(|a^2| + |d^2|\right) \\ m_{1,2} = m_{2,1} &= \frac{1}{2}\left(|a^2| - |d^2|\right) \\ m_{3,3} = m_{4,4} &= \frac{1}{2}\left(ad^* + da^*\right) = \mathbf{Re}(ad^*) \\ m_{3,4} = -m_{4,3} &= \frac{i}{2}\left(ad^* - da^*\right) = \mathbf{Im}(ad^*). \end{aligned} \tag{5.2}$$

For a sufficiently small particle regardless of shape the matrix elements are proportional to

$$\begin{aligned} m_{1,1} &= \frac{1}{2}(1 + \cos^2\theta) \\ m_{1,2} &= -\frac{1}{2}\sin^2\theta \\ m_{3,3} &= \cos\theta \\ m_{3,4} &= 0. \end{aligned} \tag{5.3}$$

This is known as Rayleigh scattering. Here θ is the scattered angle, see Figure 5.1. For larger spherical particles, the matrix elements are given by the Mie theory [2],

$$\begin{aligned} a &= \sum_{n=1}^{\infty} \frac{2n+1}{n(n+1)}(a_n\tau_n + b_n\pi_n) \\ d &= \sum_{n=1}^{\infty} \frac{2n+1}{n(n+1)}(a_n\pi_n + b_n\tau_n), \end{aligned} \tag{5.4}$$

where π_n and τ_n are recursive functions

$$\pi_n = \frac{2n-1}{n-1}\cos\theta\pi_{n-1} - \frac{n}{n-1}\pi_{n-2} \tag{5.5}$$

$$\tau_n = n\cos(\theta)\pi_n - (n+1)\pi n - 1. \tag{5.6}$$

Specifically $\pi_0 = 0$, $\pi_1 = 1$ and a_n and b_n are scattering coefficients given by

$$a_n = \frac{m\psi_n(mx)\psi_n'(x) - \psi_n(x)\psi_n'(mx)}{m\psi_n(mx)\zeta_n'(x) - \zeta_n(x)\psi_n'(mx)},$$

$$b_n = \frac{\psi_n(mx)\psi_n'(x) - m\psi_n(x)\psi_n'(mx)}{\psi_n(mx)\zeta_n'(x) - m\zeta_n(x)\psi_n'(mx)}, \tag{5.7}$$

when the permeability of the particle and surrounding medium is the same, ψ and ζ are Riccati-Bessel functions of the first and second kind. The prime indicates differentiation with respect to the arguments in the parentheses. x is a size parameter scaled as $x = \frac{2\pi N\hat{a}}{\lambda}$. $\hat{a}$ is the radius of the particle, $m = \frac{N_1}{N}$ is the relative refractive indices between that of the particle N_1 and that of the surrounding medium N. Implemented computer codes for the Mie-scattering algorithm are available on the web [76]. In this thesis the Matlab code implemented by Dave Barnett was used [77]. More robust and accurate algorithms for calculating a_n and b_n can be implemented [78].

The PSA in the rotating compensator setup collects light through a circular pinhole. The PSA will collect light from a larger area than for $\theta = 90°$, as the effective project area becomes an ellipse. This is known as the "Lambert's cosine law". In this case the measured Mueller matrix $\mathbf{M}$ is rescaled with $\sin\theta$,

$$\mathbf{M}' = \mathbf{M}\sin\theta, \tag{5.8}$$

in order to obtain a Lambertian surface, *i.e.* an area independent of viewing angle. An example of measured and simulated scattering from an ensemble with mean sphere radius $\hat{a} = 1.95$ μm is shown in Figure 5.2, together with results from Mueller matrix measurements using the rotating compensator setup. In the simulation $N = 1.596$ and $N_1 = 1.336$ were used. The simulated data was averaged over an ensemble of different particles sizes. Scattering from an ensemble of particles can be seen as a sum of scattering Mueller matrices for each individual particle [2]. Each individual matrix was scaled by a Gaussian particle distribution with standard deviation $\sigma = 3.3 \cdot 10^{-8}$m.

5.1.2 Inelastic scattering of particles

A special case of scattering is when the photon gives up or gains energy, *i.e.* inelastic scattering, for instance by phonon-photon interactions. To the author's

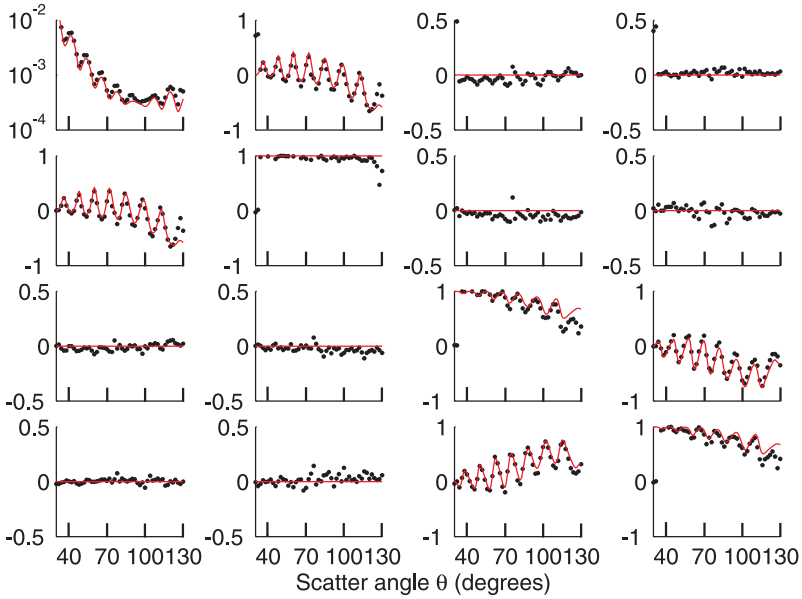

Figure 5.2: *The measured (dotted) and simulated scattering Mueller matrix (solid red) for spherical particles with mean particle radius* $\hat{a} = 1.95$ *μm and* $\lambda = 532$ *nm for various scatter angles* θ*. In the simulation a Gaussian ensemble of particle sizes with standard deviation* $\sigma = 0.03\mu m$*, was used.*

knowledge, the Mueller matrix calculus has not been widely adopted for inelastic scattering Some authors have used the Mueller matrix calculus to calculate Raman scattering [79], scattering from anisotropic biomolecules and ellipsoids [80], inelastic scattering from a uniform sphere [81] or cylinders [82]. Videen [81] used an extension of Mie theory which follows the derivation of Bohren and Huffman [2]. In inelastic scattering the scattered field E_{sca} has a lower wavenumber $k_2 = \frac{2\pi}{\lambda_2}$ than that of the plane-wave illumination E_{inc}'s, $k_1 = \frac{2\pi}{\lambda_1}$. According to Videen *et. al* [81] inelastic scattered radiation from large particles differs from that of elastic scattered radiation, while the matrix elements are equal to the matrix elements of Eq. 5.3 for both elastic and inelastic in the Rayleigh regime (small particles) [81]. The absolute magnitude of the un-scaled elements is approximately 10 times less for inelastic radiation.

5.2 Investigating fluorescence anisotropy using MME

Luminescence can be induced by the absorption of light. First the absorbed photon causes an electron to be excited from a lower electronic state (usually the ground state) to an excited state, then as the electron relaxes from the excited state to a lower electronic state a photon is emitted [83]. Luminescence is divided into two categories; fluorescence if the transition is spin allowed and phosphorescence if it is not. The energy of the absorbed photon is usually higher than that of the emitted photon.

The population of excited states within a fluorescent sample is given by the illuminating polarization states, as only molecules with a parallel transition moments component will be excited. To what extent the emitted light also is polarized, is usually determined by calculating the fluorescence anisotropy, defined as [83]

$$r_A = \frac{I_\parallel - I_\perp}{I_\parallel + 2I_\perp}. \tag{5.9}$$

Here $I_\parallel$ and $I_\perp$ are the detected fluorescent intensities when measured between parallel and crossed polarizers. Eq. 5.9 bears resemblance to the diattenuation metric in Eq 4.16.

The anisotropy in a solvent is usually time-depended as the molecules will rotate after excitation. A steady state anisotropy can be calculated from an average anisotropy decay assuming a single exponential decay curve [83]

$$r_s = \frac{r_0}{1 + \frac{\tau_F}{\theta_F}}. \tag{5.10}$$

Here, θ_F is the rotational correlation time of the molecule and τ_F the fluorescence life time.

In this section the Mueller matrix approach will be used in order to investigate the fluorescent signal from fluorescein in a solvent and bound to proteins. To retrieve an estimate for the anisotropy from a measured Mueller matrix $\mathbf{M}$, the transmitted intensities will be assumed to be approximately equal to,

$$I_\parallel \approx I(\mathbf{P}_{90^\circ}\mathbf{M}\mathbf{s}_{90^\circ}) \tag{5.11}$$

$$I_\perp \approx I(\mathbf{P}_{0^\circ}\mathbf{M}\mathbf{s}_{90^\circ}). \tag{5.12}$$

Here $\mathbf{M}$ is multiplied with a polarizer $\mathbf{P}$, Eq.2.9, aligned at 0° and 90° and an incoming Stokes vector $\mathbf{s}_{90^\circ} = [1, -1, 0, 0]^T$,

5.2.1 Fluorescein dissolved in various glycerol/ethanol concentrations

Fluorescein consists of a single linear dipole moment. Fluorescein diluted in a 0.1 M NaOH solution is known to have a rotational correlation time of 120 ps [84], which is multiple orders faster than the spped of the rotating compensator setup. Samples with different concentrations of glycerol and fluorescein dissolved in ethanol were prepared and the fluorescence Mueller matrix was measured. The sample was excited by a 473 nm coherent laser source and the emitted fluorescein signal was passed through a 532 nm interference filter. The MME was calibrated in transmission mode using both the 473 nm laser, for obtaining the generating matrix **W**, and at 532 nm for obtaining the analyzing matrix **A** of the system.

An angular Mueller matrix scan was performed on the 99.5 % glycerol solution. All the samples were stored in a cylindrical sample cell that was submerged within a larger cylindrical cell filled with water. The water in the large cylindrical cell minimized surface reflections and lens effects from the small sample cell, see Figure 5.3. The resulting angular measurement is shown in Figure 5.4. The fluores-

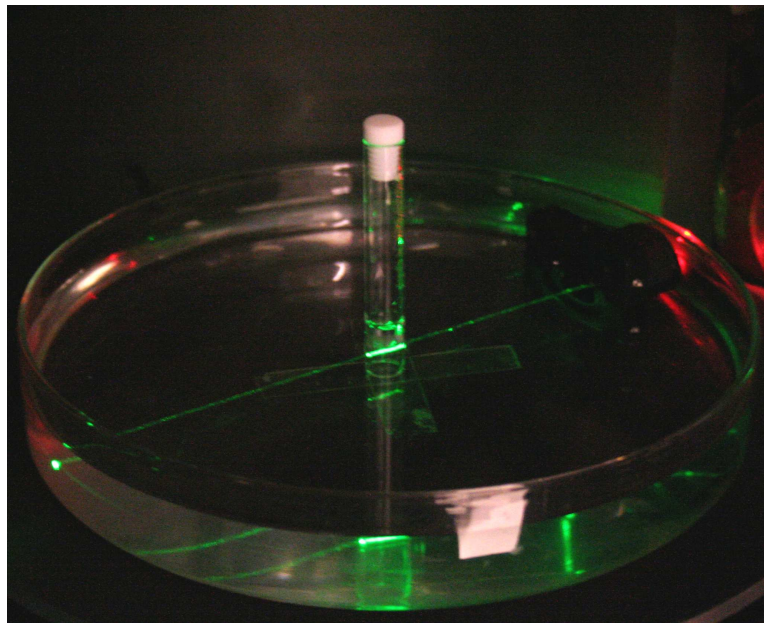

Figure 5.3: *In scattering measurements with solvent samples, the cylindrical sample cell were submerged within a larger cylindrical cell filled with water to minimize surface reflections and lens effects.*

cence Mueller matrix measured for fluorescein followed the same trend as expected

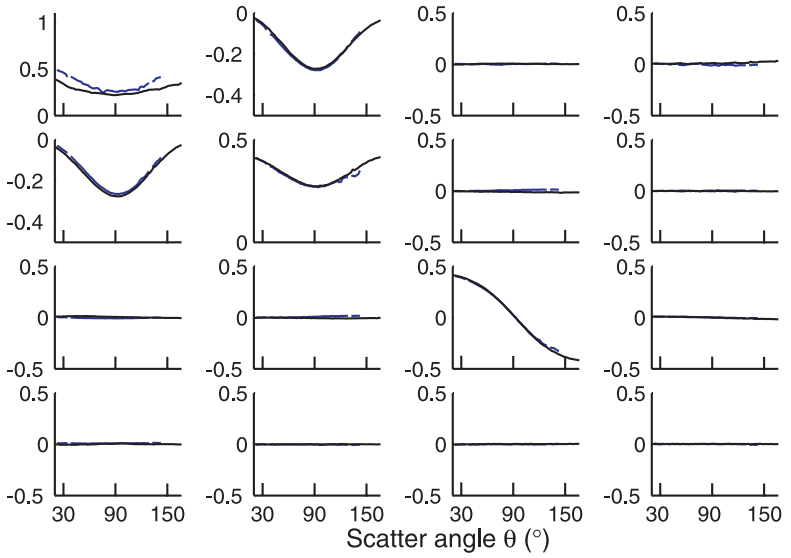

Figure 5.4: *The measured fluorescent Mueller matrix using a band lowpass filter (cutoff 490 nm)for fluorescein during 473 nm excitation (black) and for fluorescein embedded in aggregated Human transthyretin (TTR) protein (blue).*

for isotropic inelastic scattering apart from the fact that the measured fluorescence Mueller matrix elements are scaled by depolarization and that the matrix element $m_{4,4}$ is zero. The observed depolarization can easily be explained. The fluorescein solution consists of an ensemble of fluorescein molecules with randomly orientated linear dipole moments. The measured Mueller matrix consists of an averaged population of excited states given by the PSG's four polarization states. Each of these polarization states created by the rotating compensator MME is elliptical, see for instance Figure 3.6. They will to some extent populate excited states orthogonal to each other causing depolarization. Additional depolarization will be caused by the $\cos^2\theta$ probability rule [83] of also populating dipole moments aligned at an angle θ with the incoming polarizaion state. It is natural to expect $m_{4,4}$ to be zero as fluorescein is unable to emit circularly polarized light, since it only has a linear dipole moment. The theory for inelastic scattering from a uniform sphere described by Videen *et. al* [81] is therefore incapable of describing this system, as $m_{4,4} = m_{3,3}$ in their description. Few attempts have been made using the Mueller matrix approach to fluorescence [85]. The Mueller matrix formalism would need to be extended to account for such phenomena.

The steady state anisotropy was calculated from time resolved anisotropy measurements performed with a Jobin Yvon IBH FluoroCube photon-counting

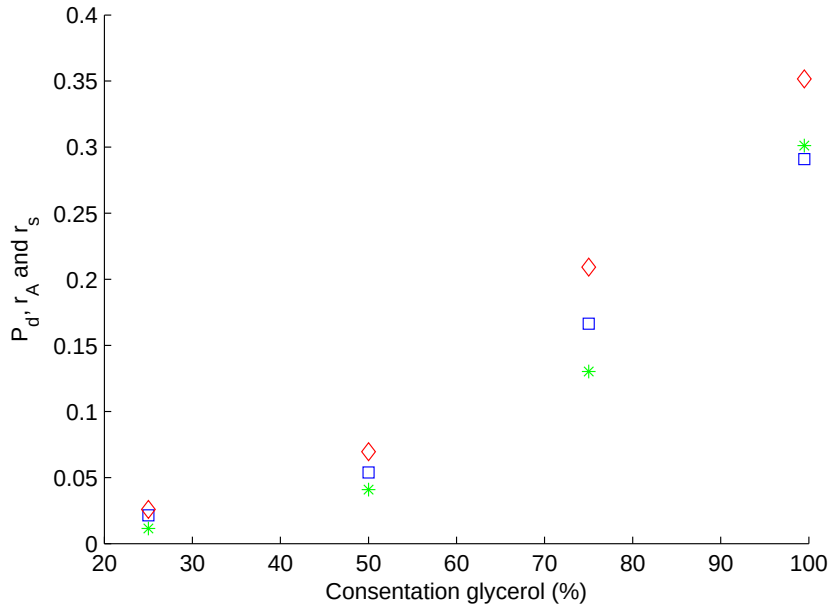

Figure 5.5: *The steady-state anisotropy $r_s(*)$, calculated Mueller matrix anisotropy r_A ($\diamondsuit$) and the polarization index P_d ($\square$) for fluorescein dissolved in different glycerol-ethanol concentrations.*

spectrometer in order to compare results with the MME measurements. The measured decay curves were fitted to a single exponential decay $r(t) = r_0 e^{-t/\theta_F}$ and the rotational correlation time θ_F was obtained. The average fluorescence life time τ_F for fluorescein was calculated from the same measurements resulting in $\tau_F = 3.86$ ns. The fluorescence Mueller matrix measurements and steady state anisotropy measurements were performed for fluorescein diluted in 25%, 50%, 75% and 99,5% glycerol concentrations in ethanol at $\theta = 90°$. As seen from Figure 5.4, this is the angle where the amplitudes of $m_{1,2}$ and $m_{2,1}$ are largest. The polarization index and an estimate for the fluorescent anisotropy were compared to the calculated steady state anisotropy, see Figure 5.5. The steady-state anisotropy $r_s(*)$ and the calculated Mueller matrix anisotropy r_A follow the same trend, within experimental analysis. Also the depolarization index follow this trend. They all increase as the molecules become immobilized for higher concentrations of glycerol, which is expected since the emitted light become more polarized.

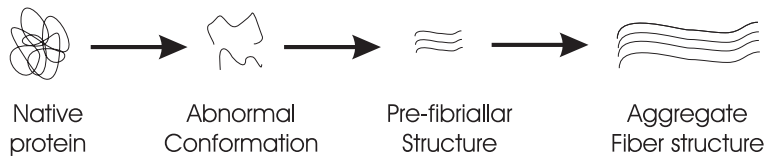

Figure 5.6: *Proteins can sometimes unfold to an abnormal conformation which can aggregate into a fiber structure.*

5.3 MME measurements during protein aggregation

Misfolded proteins and peptides can evolve into amyloid fibrils. Aggregates of such structures are known to be the hallmark of a least 20 different diseases [86], including Diabetes II, Alzheimer's and Parkinson's. During the formation of fibrils the abnormal protein conformations can go through several pre-fibrillar states see Figure 5.6. Paper VI investigates three conjugated polyelectrolytes used to study protein folding processes. In this section polarimetric signatures from aggregated Human transthyretin (TTR) protein will be investigated by performing scattering and fluorescence Mueller matrix ellipsometry.

5.3.1 Elastic scattering measurements

The protein Human transthyretin (TTR) is known to aggregate to particles and fibrillar structures upon certain denaturing conditions [87, 88]. Scattering polarimetric measurements were performed after the TTR proteins had aggregated to a final stable end product. The aggregates were submerged in distilled water and illuminated with a 405 nm coherent laser source. The rotating compensator system was then used to collect the Mueller matrices for various scatter angles. The results were compared with Rayleigh and Mie scattering. The same cylindrical sample cell, as that shown in Figure 5.3, was used. As can be seen from Figure 5.7, the scattered light clearly follow the profiles expected for Rayleigh scattering. As the upper right 2×2 and lower 2×2 sub-elements are close to zero. This indicate that the element b and c in Eq. 5.1 is zero. One can therefore conclude that there is no large optical active effect in the aggregated protein sample. Large oscillations are expected in the matrix elements for outside the Rayleigh limit for spherical particles, as the scatter angle varies. In the matrices seen in Figure 5.8, a particle with refractive index 1.4 submerged in water has been assumed. Large oscillations are seen for particles with greater radius than 0.2 μm. An ensemble of various particle sizes will to some extent average the oscillation observed in the matrix elements, as it can be seen as a sum over Mueller matrices [2]. The matrix element m_{12} and $m_{3,3}$ are generally larger than those seen for Rayleigh scattering, so this averaging will result in a different matrix. Large differences are observed

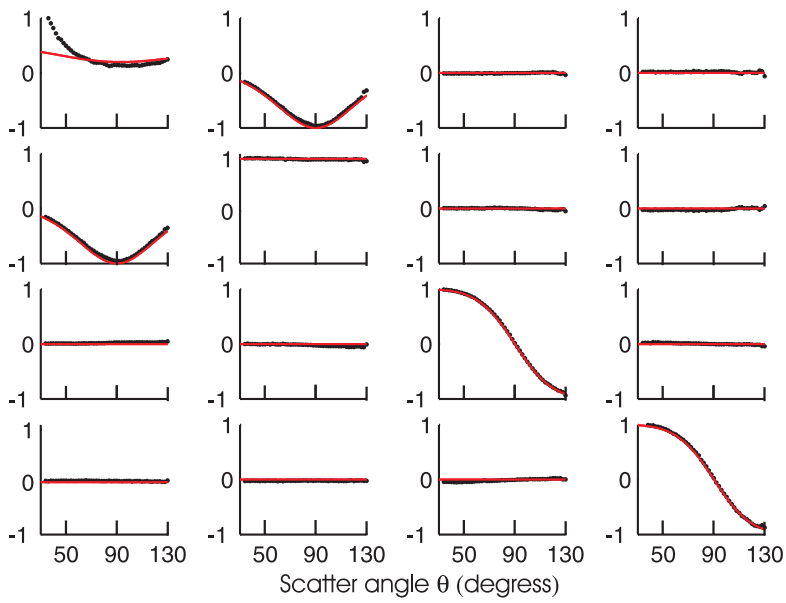

Figure 5.7: *The scattering Mueller matrix from aggregated TTR proteins during 405 nm coherent illumination at various scatter angle θ (blue dots), resembles Rayleigh scattering (red line) with the exception of $m_{1,1}$.*

for element $m_{1,1}$ for particles below 0.2 μm. $m_{1,1}$ becomes increasingly dominated by forward scattering as the particle size increases. This is also seen in Figure 5.7, as $m_{1,1}$ is not $\propto (1 + \cos^2(\theta))$.

5.3.2 Polarimetric Fluorescence measurements

A solution of TTR protein with embedded fluorescein molecules was prepared and added a NaCl solution in order to start the aggregation process. The sample was excited with a 473 nm coherent laser source, and the PSA collected the fluorescence Mueller matrices by passing the scattered light through a lowpass filter. The fluorescent Mueller matrices were collected within three time periods, before the aggregation process started, 60-5000 s and 147000-15000 s after, with 50 s intervals.

Both the depolarization index given by Eq.4.3 and r_A Eq. 5.12 were calculated from the Mueller matrices.

The calculated results, shown in Figure 5.9, were fitted against $R(t)$ and

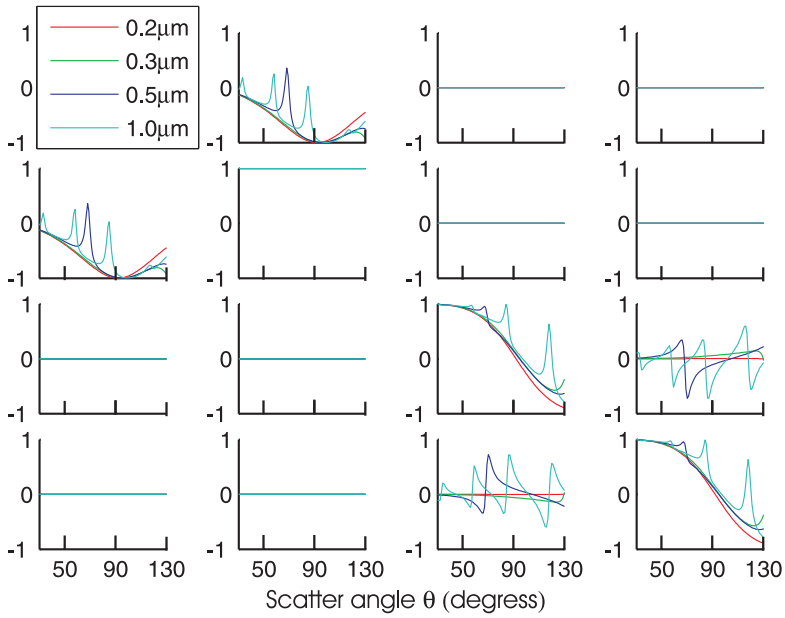

Figure 5.8: *The Scattering Mueller matrices for different particles sizes* $[0.2, 0.3, 0.5, 1]\mu m$.

Table 5.1: *Measured and fitted parameters from the Protein aggregation process.*

R_0	A_{r1}	A_{r2}	τ_{r1}	τ_{r2}	P_0	A_{p1}	A_{p2}	τ_{p1}	τ_{p2}
0.32	0.20	0.06	160	5130	0.27	0.17	0.53	160	5280

$P_d(t)$, given by

$$R(t) = R_\infty - A_{r1}e^{-t/\tau_{r1}} - A_{r2}e^{-t/\tau_{r2}}, \tag{5.13}$$

$$P_d(t) = P_\infty - A_{p1}e^{-t/\tau_{p1}} - A_{r2}e^{-t/\tau_{p2}}. \tag{5.14}$$

R_∞ and P_∞ are the end state anisotropy and end state depolarization index. The parameters obtained from the fit are tabulated in Table 5.1. The protein aggregation process seems to be governed by one fast and one slow process, which fits a double exponential decay curve [87]. Also an angular scan of the final state of the aggregated protein was performed, which resulted in similar fluorescent Mueller matrix as that observed for fluorescein in glycerol, see Figure 5.4. As the proteins form larger and larger aggregates, they use a longer time to rotate in the solution. Due to this the embedded fluorescein molecule will also become less mobile. This is probably the reasons why the light becomes more polarized with a higher anisotropy as seen in Figure 5.9. The dynamics in the aggregation process can be

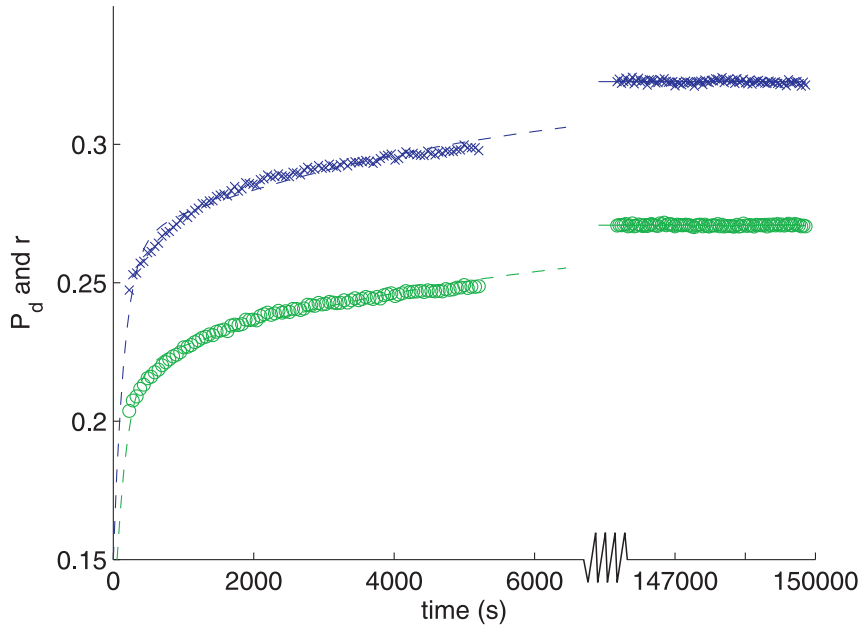

Figure 5.9: *The measured and fitted polarization index P_d ($\circ$) and anisotropy r_A ($\times$) during the TTR protein aggregation.*

followed either by measuring the polarization index during the aggregation process or by performing anisotropy measurements.

Table 5.2: *Other Mueller matrix imaging polarimeters found in the literature. (EOVR) Electro optical variable retarder, (PC) Pockels cells, (DOA) division of amplitude (RR) Rotating retarder, (LCVR) Liquid-crystal variable retarders, (QWP) quarter waveplate*

Author	Technology	Wavelength (nm)	Light source
Chipman and Pezzaniti [44]	RR	633	He-Ne laser
Pelz *et.al.* [39]	PC	785	laser diode
Lara and Dainty [40]	PC+DOA	535	solid state laser
Bueno and Artal [37]	LCVR+QWP	633	laser diode
Baba *et.al.* [91]	EOVR	635	white light
Laude-Boulesteix *et. al.* [41]	LCVR	500-700	white light

5.4 NIR to IR imaging MME

Polarimetric imaging can provide information that is uncorrelated with spectral and intensity images gives complementary information about samples. Polarimetric imaging is being used in various applications like remote sensing [89], biology [90], biomedical imaging [37, 39, 41, 91] and industrial monitoring [92].
From a literature survey, summarized in Table 5.2, several other Mueller matrix imaging polarimeters were found.

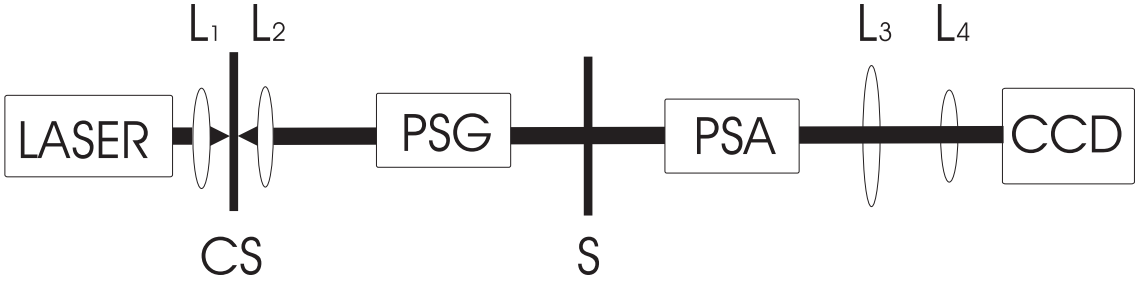

Figure 5.10: *Schematics of the Mueller matrix imaging polarimeter. L_1 and L_2 focus and collimates the laser light onto and from a coherence scrambler (CS). The sample S is mounted between the polarization state generator PSG and the polarization state analyzer PSA.*

The Ferro-electric liquid crystal based ellipsometer described in Section 3.3.2 and Paper III, was modified to be used also for imaging MME. A telescopic lens system (L_3,L_4) was mounted after the PSA in order to image the sample onto the CCD of a XEVA-FPA-1.7- 640 digital camera, as shown in Figure 5.10. The chosen digital camera operates at 15Hz and has a 14-bit InGaAs detector array

being sensitive in the range 0.9 - 1.7 μm. The samples are illuminated with a coherent laser source that has passed through a rotating diffuser plate (coherence scrambler), mounted in front of the PSG. The laser light is focused onto a small point on the diffuser plate of the coherence scrambler and a second lens collimates the scattered light. This removes the speckle patterns in the final image otherwise created by laser illumination. Each individual pixel x, y collects the intensity $\mathbf{B}$ equal to that of Eq. 3.1. The system is then calibrated using the procedure described in Section 3.5. The Mueller matrix at each pixel is obtained using Eq. 3.2 from which a Mueller matrix image $\mathbf{M}_{pic}$ is constructed,

$$\mathbf{M}_{pic} = \begin{bmatrix} m_{1,1}^{1,1} \cdots m_{1,1}^{1,l} & \cdots & \cdots & m_{1,4}^{1,1} \cdots m_{1,4}^{1,l} \\ \vdots & \vdots & \vdots & \vdots \\ m_{1,1}^{k,1} \cdots m_{1,1}^{k,l} & \cdots & \cdots & m_{1,4}^{k,1} \cdots m_{1,4}^{k,l} \\ \vdots & \ddots & & \vdots \\ \vdots & & \ddots & \vdots \\ m_{4,1}^{1,1} \cdots m_{4,1}^{1,l} & \cdots & \cdots & m_{4,4}^{1,1} \cdots m_{4,4}^{1,l} \\ \vdots & \vdots & \vdots & \vdots \\ m_{4,1}^{k,1} \cdots m_{4,1}^{k,l} & \cdots & \cdots & m_{4,4}^{k,1} \cdots m_{4,4}^{k,l} \end{bmatrix}. \tag{5.15}$$

5.4.1 Polarimetric stress and strain mapping

Polarimetric imaging is an excellent tool for investigating stress in materials. Transparent materials which experience a non-uniform stress usally become optically anisotropic. Polarimetric imaging can for instance be used in lens design [93] to reduce unwanted stress. The capability of the MME system to image stress

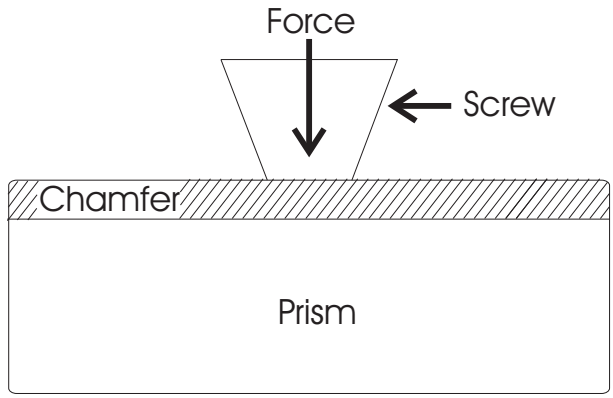

Figure 5.11: *Schematics of the scene under investigation. A screw enforced stress upon a glass prism in CaF_2. The prism is non-opaque directly below the screw, due to a crudely polished chamfer.*

patterns was investigated by inducing a direct force onto an optical component. A CaF_2 prism was pressed between a screw and a support, see Figure 5.11. The FLC imaging MME collected the Mueller matrix image $\mathbf{M}_{pic}$ as pressure was enforced by a screw. The obtained $\mathbf{M}_{pic}$, see Figure 5.12, experienced changes in the lower right 3×3 elements.

No visible polariance or diattenuation was seen for this sample, since the first column and row vector of the Mueller matrices are zero. A consequence of this is that the retardance vector $\mathbf{r} = [1, r_1, r_2, r_3]$ can be directly calculated from the subelements $m_{i,j}$ of $\mathbf{M}$, since $\mathbf{M}$ has the form of $\mathbf{M}_R$ in Eq. 4.17. The decomposition routine of Section 4.2 is not needed. However, the decomposition technique would be valuable for other samples when diattenuation and depolarization are present. The total retardation R is given by Eq. 4.26. The azimuth orientation θ of $\mathbf{r}$ is parallel with the fast axis of the rotated retarder equivalent system, and is given by Eq. 4.27. Figure 5.13 shows the orientation of the slow axis of the retarder (arrows, $\theta+\pi/2$) and the magnitude of the total retardation (color coded). The retardation's slow axis has a higher optical density than the fast axis and is proportional to the compression in the prism. The relative magnitude and orientation of the stress distribution in the prism can thereby be obtained. To estimate the quality of

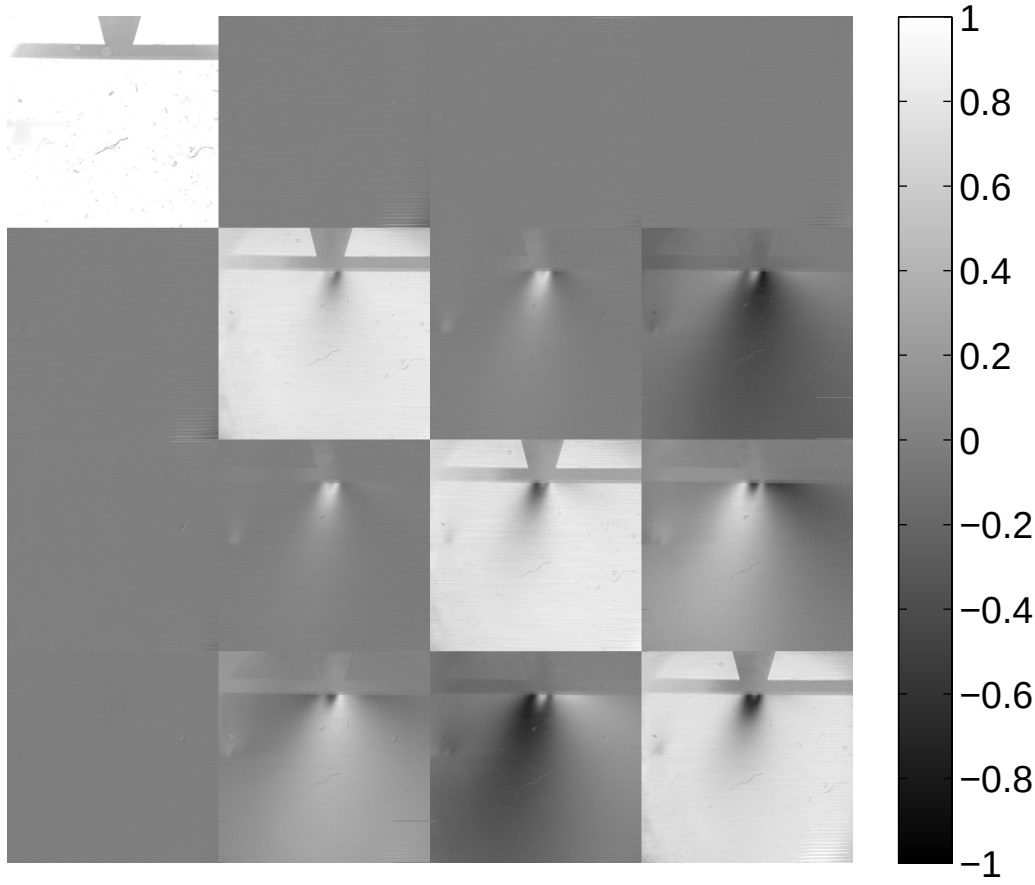

Figure 5.12: *The changes in the measured Mueller matrix of the CaF_2 prism are similar to that of a rotated pure retarder, upon enforcing stress.*

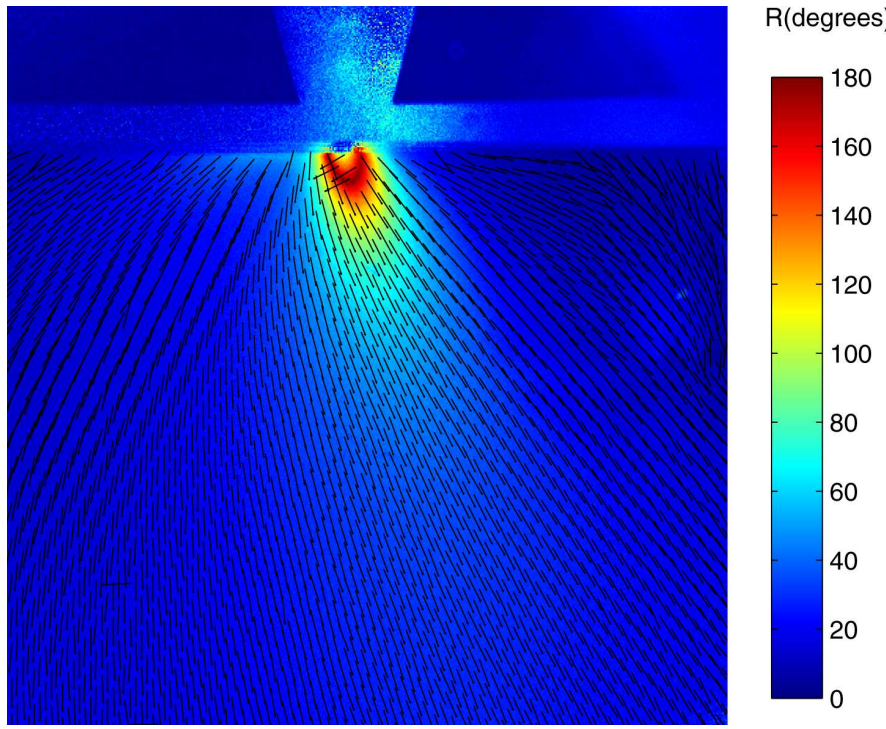

Figure 5.13: *Combined vector field and absolute retardance for the CaF_2 prism during strain. The magnitude of the retardation is color coded in the figure, while the orientation of the retardations slow axis is indicated by arrows, i.e. the orientation of the polarization vector which will experience the highest optical density when passing through the prism.*

the measurements the Cloude fidelity test, Eq. 4.3, was applied on the measured Mueller matrices, see Section 4.1. The fidelity of $\mathbf{M}_{pic}$ in Figure 5.12 is shown in Figure 5.14. Dust and interference fringes are not visible in for instance Figure 5.13, but are clearly visible in Figure 5.14 . Questionable data points can in this way be discriminated from the physically correct data points with high contrast. The chamfer edge and the screw areas where the light has not been transmitted are two such areas. Also the white stripes in the lower left corner show an area which has not been properly covered by one of the calibration samples. The waveplate used in this calibration was actually too small to cover the whole image area. The same areas contain small dark patches where the Mueller matrices are physically realizable. This is a limitation in the fidelity test. It can only detect matrices which are physically realizable and not check if they are 100 % correct.

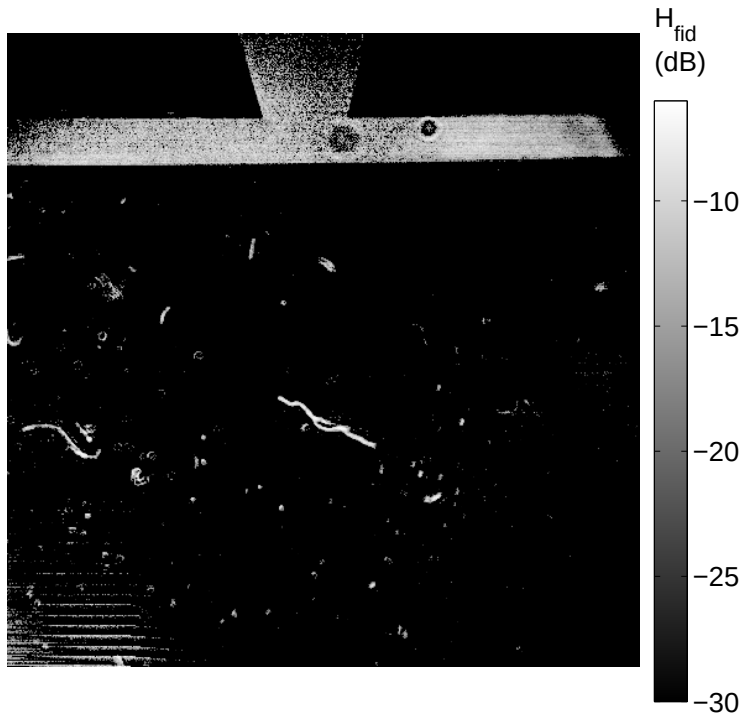

Figure 5.14: *The fidelity of the measured Mueller matrix. Dust and interference fringes are clearly visible with high contrast when using the Cloude fidelity test.*

6 Summary and Conclusion

One of the first approaches for measuring the complete Mueller matrix was to apply polarizers in combination with rotating retarders. The first ellipsometer discussed in this thesis is a variant of such a setup. This system is unique as it uses achromatic CaF_2 132° Fresnel bi-prisms for obtaining the Mueller matrix. This makes it capable of performing optimal measurements over a broad wavelength range. The achromatic behavior of the prisms is due to the low dispersion of CaF_2 and the large internal reflection angle within the prisms. The ellipsometer system has been specifically tested for wavelengths at 405, 473, 532, 633 and 1570 nm, which results in well conditioned system matrices. A well conditioned system is important for reducing calibration and random noise errors. The prisms' actual retardance has been shown to be close to optimum within the 400-8000 nm region and should be able to perform well also further into the ultra-violet region. This ellipsometer is intended for scattering measurements, and in Chapter 5 this instrument was used in scattering and fluorescence studies. In addition to the applications tested in Paper II, it was shown that the aggregation process of protein Human transthyretin (TTR) could be followed by using fluorescence Mueller matrix measurements. The protein aggregation dynamics seemed to be governed by one fast and one slow process. It was fitted to a double exponential decay curve, as observed earlier [87]. The final stable state of the aggregation process resulted in particle sizes near the Rayleigh limit with aggregated proteins smaller than the wavelength (405 nm). The exception was element $m_{1,1}$ which was slightly larger towards forward scattering.

Some improvements can still be made to the rotating compensator system. The electronics should be upgraded to lower the overall random noise. The current from the PMT detector is for instance measured over a high Ohm resistor in order to read out a voltage signal to the NI-DAQ board. Also a reference detector should be applied in the system, as oscillations in the laser sources are not currently accounted for. In studies of scattering processes, the system might also perform better if it is calibrated on suspension of spherical particles as performed by Kaplan *et al.* [94]. Only transmission calibration is currently used. Kaplan *et al.*'s approach has its own problems as clustering of particles and non-spherical particles can create systematical errors. The approach also includes mounting a removable polarizer directly in front of the PSA. The mounting arm of the PSA has been extended in order to make place for an extra polarizer. This makes it

suitable also for reflection calibration [49]. Chapter 5 also points out that further theoretical development of the Mueller-Stokes description is needed for describing fluorescence Mueller matrix ellipsometry in order to account for photo-selection processes given by the PSG.

The acquisition speed is also quite low (1/50 Hz), mainly due to the accurate but slow Newport PR50 stepper motors with a maximum angular speed of only $20°/s$. A faster system can be achieved by exchanging the two stepper motors of the PSA and PSG. The overall speed of the system has been optimized to some extent using the current stepper motors. The distance between each of the optimized angular positions are not equal, as it consists of a short step $\Delta\theta B$ and a large step $\Delta\theta A$. Now the current optimized stepping profile, shown in Figure 6.1, is used.

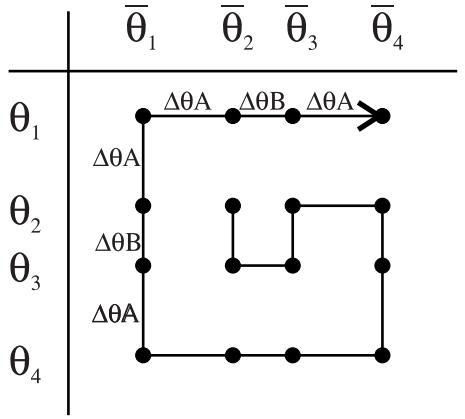

Figure 6.1: *The current stepping profile of the PSAs angle θ and PSG $\bar{\theta}$. $\Delta\theta B$ and $\Delta\theta A$ are the angular distance between the steps.*

A FLC-MME was designed in order to acquire Mueller matrices fast. Currently it can acquire complete Mueller matrices at around 50 Hz. It has been optimized for operation between 800-1900 nm and is to our knowledge the first Ferro-electric based NIR Mueller ellipsometer. The system might be pushed to operate faster than 50 Hz on the expense of accuracy. Some stability is already obtained after 0.2 ms, as seen from the plot of the variance in Figure 3.5. Mueller matrices can easily be sampled at 150 Hz. Operating faster than this will seriously reduce accuracy as the FLCs become unstable. The system is not truly optimal for a broad wavelength, as the system can be improved by choosing different fixed waveplates and FLCs thicknesses. Our group has also designed a system based on nematic liquid crystals variable retarders [42], which has an optimal broad band performance. This system operates at a lower acquisition speed (0.25 Hz), as

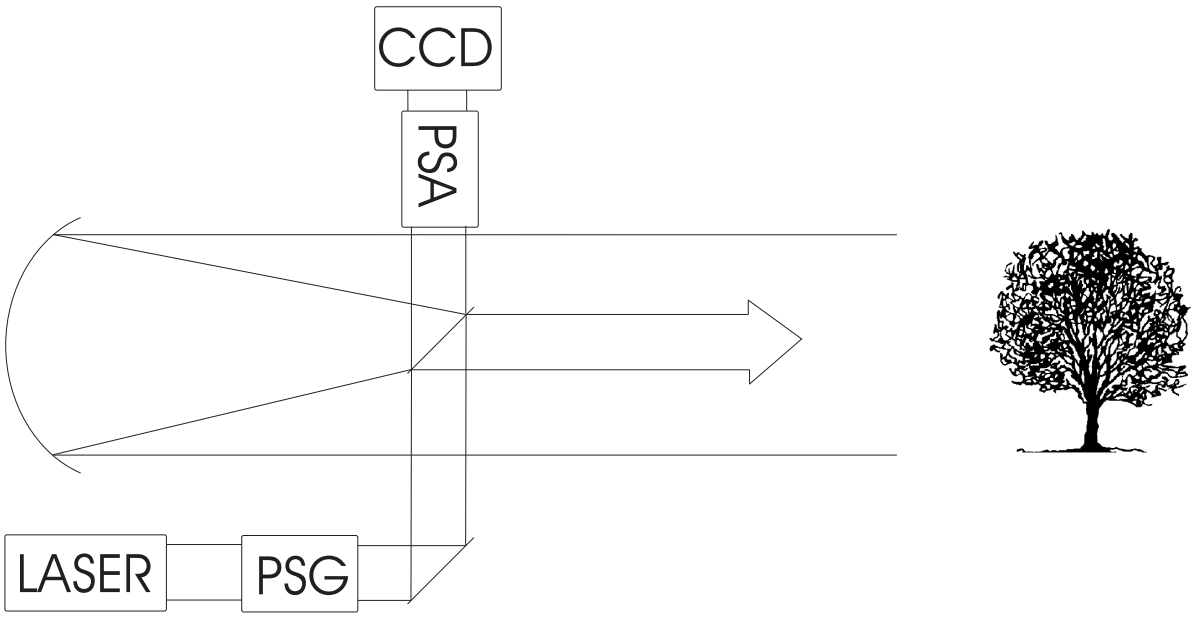

Figure 6.2: *The illuminating polarization state is reflected by the two mirrors and the backscattered light is imaged by a Newtonian telescope onto a CCD.*

stability of the crystals is reached at a later time.

Chapter 5 showed how the FLC based system could be extended to an imaging polarimeter by including lenses and exchanging the InGaAs detector with an InGaAs CCD. The current camera operates at 15 Hz which reduces the acquisition rate of Mueller matrices to approximately 1 Hz. The main speed limitations is the calculation of the Mueller matrix from Eq.3.2 which scales with the resolution of the image. Work is currently under progress as Master student projects to reduce this calculation time. This is important for real time monitoring of a sample. The $\mathbf{B}_{pic}$ images can also be stored directly to the hard drive during acquisition and the Mueller matrices be calculated later on. The optics in the imaging system, currently image the sample at an approximate 1:1 ratio. The numerical aperture of the system is rater low and limits the overall resolution. The resolution has not yet been our main concern since it will limit the acquisition speed, but can be further improved.

Paper V discussed the possibility of utilizing polarimetry for mine detection, however some sort of imaging polarimeter should be used. One option would be to use a system similar to Breugnot and Clémenceau's design. They report on a remote dual rotating Mueller matrix imaging polarimeter which includes a Newtonian telescope collecting the backscattered light [16], see Figure 6.2. They also suggested a much simpler polarimetric acquisition routine for backscattering

geometries. In backscattering geometries only the diagonal elements of the Mueller matrix appear to be non-zero [16] (as concluded in our detailed investigation). Depolarization is the only polarimetric containing information. This was also the case for the measured mines in Paper V. In many cases also the elements which alter the linear depolarization $m_{2,2}$ and $m_{3,3}$ are similar. This was also the general case for the mines. However, large differences were observed in some of the plants. This is probably due to the ordered fiber structure of the leafs. A few of the mines showed differences in these values which were probably caused by surfaces scratches. Breugnot and Clémenceau show that in cases where $m_{2,2}$ and $m_{3,3}$ are similar, the acquisition can be simplified by illuminating with only one specific polarization state and using only two orthogonal analyzing states. If the system is used in some sort of "division of amplitude configuration" [34], where two CCD cameras measure different polarization states, the system can operate in a static configuration with no moving parts. $m_{2,2}$ and $m_{4,4}$ cannot be separated with this limited number of measurements, so Breugnot and Clémenceau used a different definition for magnitude of the depolarization,

$$P_d = \frac{2m_{2,2} + m_{4,4}}{m_{1,1}}. \tag{6.1}$$

The techniques discussed in this thesis are general and can be applied for optimizing and calibrating any Mueller matrix ellipsometer. One of the discussed routines is the eigenvalue calibration technique of Compain *et al.* [49], which appears as a powerful characterization tool, as it can also be used for non-ideal systems. The techniques for analyzing the Mueller matrix are also general. Checking if the measured Mueller matrix is physically realizable by using Cloude's fidelity test has proven to give valuable information about the measurement. The fidelity is low when serious artifacts, such as partial beam blocking and misalignment, are present. This becomes specially obvious in imaging systems, as dust and interference patterns can be identified with high contrast, see Figure 5.14. Cloude's fidelity test works best for non-polarizing samples. To the author's experience, depolarizing samples easily become physically realizable even when artifacts are present. To the author's experience, measurements with larger fidelity than -15 dB have usually been effected by calibration errors or misalignment.

The decomposition routine of Lu and Chipman [60] is an attractive analyzing technique when system modeling is impossible or hard, as the physical parameters of the Mueller matrix like diattenuation, retardation and depolarization can be obtained. The orientations of the retardation axis and diattenuation axis are also easily obtained. This can for instance be directly related to stress fields as demonstrated in Figure 5.13, or orientation of microstructures or samples as in Paper IV. Several variants of the decomposition routine exist. In this thesis only a review of the forward decomposition procedure was emphasized. As pointed out in

Section 4.2, which decomposition routine to use is governed by the depolarization in the samples. Discussion around inhomogeneous Mueller matrices has also been omitted in this thesis, since other variants of the decomposition routine must be used in such cases.

Bibliography

[1] Collett, E., [*Polarized light Fundamentals and applications*], Marcel Dekker Inc, 270 Madision Avenue, New York (1993).

[2] Bohren, C. F. and Huffman, D. R., [*Absorbtion and Scattering of light by small particles*], Wiley-VCH Verlag GmbH & Co. KGaA, Weinheim, Germany, first ed. (2004).

[3] Dacke, M., Nilsson, D.-E., Scholtz, C. H., Byrne, M., and Warrant, E. J., "Animal behavior insect orientation to polarized moonlight" *Nature* **424**, 33–34 (2003).

[4] Shashar, N., Rutledge, P., and Cronin, T., "Polarization vision in cuttlefish in a concealed communication channel?" *J. Exp. Bio.* **199**, 2077–2084 (1996).

[5] Bartholin, E., "Experiments on birefringent Icelandic crystal; translated by Thomas Archibald" *Acta Historica Scientarium Naturalium et Medecinalum* **40**, "Danish National Library of Science and Medicine" (1669).

[6] Roslund, C. and Beckman, C., "Disputing Viking navigation by polarized skylight" *Appl. Opt.* **33**, 4754–4755 (1994).

[7] del Toro Iniesta, J. C., [*Introduction to Spectropolarimetry*], Cambridge, UK: Cambridge University Press (2003).

[8] Brosseau, C., ed., [*Fundamentals of polarized light a statical optics approach*], John Wiley & Sons, Inc, Inc, 605 Third Avenue, NY 10158-0012 (1998).

[9] Applequist, J., "Optical activity: Biot's bequest" *Am. Sci.* **75**, 58–68 (1987).

[10] Kahr, B. and Claborn, K., "The lives of Malus and his bicentennial alw" *Chem. Phys. Chem.* **9**, 43–58 (2008).

[11] Fairbairn, M. B., "Physical models of Haidinger's brush" *J. Royal. Astro. Soc. Can.* **95**, 248–251 (2001).

[12] Haidinger, W., "Ueber das directe erkennen des polarisirten lichts und der lage der polarisationsebene" *Ann. der Phys.* **139**, 29–39 (1844).

[13] Turner, G. L., [*Nineteenth Century Scientific Instruments*], Berkeley, University of California Press (1983).

[14] Browne, C. and Zerban, F. W., [*Physical and Chemical methods of sugar Analysis*], John Wiley & Sons, Inc, 605 Third Avenue, NY 10158-0012, 3 ed. (1948).

[15] Bass, M., Stryland, E. W. V., Williams, D. R., and Wolfe, W. L., [*Handbook of Optics Volume II Devices, Measurements, and Properties*], New York, NY: McGraw-Hill, INC, 2 ed. (1995).

[16] Breugnot, S. and Clemenceau, P., "Modeling and performances of a polarization active imager at lambda = 806 nm" *Opt. Eng.* **39**, 2681–2688 (2000).

[17] Hauge, P., Mueller, R. H., and Smith, C., "Conventions and formulas for using the Mueller-Stokes calculus in ellipsometry" *Surf. Sci.* **96**, 81–107 (1980).

[18] Stokes, G. G., "Ueber die Veränderung der Brechbarkeit des Lichts" *Ann. der Phys.* **163**, 480–490 (1852).

[19] Schellmann, J. and Jensen., H., "Optical Spectroscopy of oriented Molecules" *Chem. Rev.* **87**, 1359–1399 (1987).

[20] Poincaré, H., "Theorie Mathematique de la Lumière" **2**, Georges Carré, Paris (1892).

[21] Azzam, R. and Bashara, N., [*Ellipsometry and polarized light*], Amsterdam : North-Holland (1987).

[22] Soleillet, P., "Sur les paramètres caracterisant la polarisation partielle de la lumiere dans les phenomenes de fluorescence." *Ann. de Phys.* (23) (1929).

[23] Perrin, F., "Polarization of light scattered by isotropic opalescent media" *J. Chem. Phys.* **10** (1942).

[24] Mueller, H. *M.I.T Lecture, Cource (8.26), Spring* (1945).

[25] Jones, R. C., "New calculus for the treatment of optical systems. I. Description and discussion of the calculus" *J. Opt. Soc. Am. (1917-1983)* **31**, 488–493 (1941).

[26] Jones, R. C., "A new calculus for the treatment of optical systems V. A more general formulation, and description of another calculus" *J. Opt. Soc. Am. (1917-1983)* **37**, 107–110 (1947).

[27] Wolf, E., "Unified theory of coherence and polarization of random electromagnetic beams" *Phys. Lett. A* **312** (2003).

[28] Wolf, E., [*Introduction to the Theory of Coherence and Polarization of Light*], Cambridge University Press, Cambridge, UK (2007).

[29] Barakat, R., "Theory of the coherency matrix for light of arbitrary spectral bandwidth" *J. Opt. Soc. Am. (1917-1983)* **53**, 317–322 (1963).

[30] Born, M. and Wolf, E., [*Principles of Optics*], Pergamon Press, London, UK (1959).

[31] Fano, U., "A Stokes-parameter technique for the treatment of polarization in Quantum Mechanics" *Phys. Rev.* **93**, 121–123 (1954).

[32] Anderson, D. and Barakat, R., "Necessary and sufficient conditions for a Mueller matrix to be derivable from a Jones matrix" *J. Phys. D: Appl. Phys.* **11**, 2305–2319 (1994).

[33] Simon, R., "The connection between Mueller and Jones matrices of polarization optics" *Opt. Commun.* **42**, 293–297 (1982).

[34] Azzam, R. M. A., "Arrangement of four photodetectors for measuring the state of polarization of light" *Opt. Lett.* **10**, 309–311 (1985).

[35] Thompson, R. C., Bottiger, J. R., and Fry, E. S., "Measurement of polarized light interactions via the Mueller matrix" *Appl. Opt.* **19**, 1323–1332 (1980).

[36] Compain, E. and Drevillion, B., "High-frequency modulation of the four states of polarization of light with a single phase modulator" *Rev. Sci. inst.* **69**(4), 1574–1580 (1998).

[37] Bueno, J. M. and Artal, P., "Double-pass imaging polarimetry in the human eye" *Opt. Lett.* **24**, 64–66 (1999).

[38] Delplancke, F., "Automated high-speed Mueller matrix scatterometer" *Appl. Opt.* **36**, 5388–5395 (1997).

[39] Pelz, B. C., Weschenmoser, C., Goelz, S., Fischer, J. P., Burk, R. O., and Bille, J. F., "In-vivo measurement of the retinal birefringence with regard to corneal effects using an electro-optical ellipsometer" *Proc. SPIE* **2930**, 92–101 (1996).

[40] Lara, D. and Dainty, C., "Axially resolved complete Mueller matrix confocal microscopy" *Appl. Opt.* **45**, 1917–1930 (2006).

[41] Laude-Boulesteix, B., de Martino, A., Drévillon, B., and Schwartz, L., "Mueller polarimetric imaging system with liquid crystals" *Appl. Opt.* **43**, 2824–2832 (2004).

[42] Ladstein, J., Kildemo, M., Svendsen, G. K., Nerbø, I. S., and Stabo-Eeg, F., "Characterisation of liquid crystals for broadband optimal design of Mueller matrix ellipsometers" *Proc. SPIE* **6587** (2007).

[43] Azzam, R. M. A., "Photopolarimetric measurement of the Mueller matrix by Fourier analysis of a single detected signal" *Opt. Lett.* **2**, 148–150 (1978).

[44] Pezzaniti, J. L. and Chipman, R. A., "Mueller matrix imaging polarimetry" *Opt. Eng.* **34**, 1558–1568 (1995).

[45] Garcia-Caurel, E., "Spectroscopic Mueller polarimeter based on liquid crystal devices" *Thin Sol. Film.* **455**, 120–123 (2004).

[46] Gandorfer, A. M., "Ferroelectric retarders as an alternative to piezoelastic modulators for use in solar Stokes vector polarimetry" *Opt. Eng.* **38**, 1402–1408 (1999).

[47] Tyo, J. S., "Noise equalization in Stokes parameter images obtained by use of variable-retardance polarimeters" *Opt. Lett.* **25**, 1198–1200 (2000).

[48] Sabatke, D. S., Descour, M. R., Dereniak, E. L., Sweatt, W. C., Kemme, S. A., and Phipps, G. S., "Optimization of retardance for a complete Stokes polarimeter" *Opt. Lett.* **25**, 802–804 (2000).

[49] Compain, E., Poirier, S., and Drevillon, B., "General and self-consistent method for the calibration of polarization modulators, polarimeters, and Mueller-matrix ellipsometers" *Appl. Opt.* **38**, 3490–3502 (1999).

[50] Laude-Boulesteix, B., "Développements instrumentaux en imagerie tomographique et polarimétrique" *PhD thesis, Ecole polytechnique* (2004).

[51] Lu, S. and Chipman, R. A., "Generalized diattenuation and retardance for inhomogeneous polarization elements" *Proc. SPIE* **1746**, 197–200 (1992).

[52] Lu, S. and Chipman, R. A., "Homogeneous and inhomogeneous Jones matrices" *J. Opt. Soc. Am. A* **11**, 766–773 (1994).

[53] van der Mee, C. V. M., "An eigenvalue criterion for matrices transforming Stokes parameters" *J. Math. Phys.* **34**, 5072–5088 (1993).

[54] Gil, J., "Characteristic properties of Mueller Matrices" *J. Opt. Soc. Am. A* **17**(2), 328–334 (2000).

[55] Cloude, S. R., "Conditions for physical realizability of matrix operators in polarimetry" *Proc. SPIE* **1166**, 177–185 (1990).

[56] Cloude, S. R. and Pottier, E., "Concept of polarization entropy in optical scattering" *Opt. Eng.* **34**, 1599–1610 (1995).

[57] Hayes, D. M., "Error propagation in decomposition of Mueller matrices" *Proc. SPIE* **3121**, 112–123 (1997).

[58] Kostinski, A. B., "Depolarization criterion for incoherent scattering" *Appl. Opt.* **31**, 3506–3508 (1992).

[59] Roy-Bréhonnet, F., Jeune, B., Cariou, J., and Lotrian, J., "Optical media and target characterization by Mueller matrix decomposition." *J. Phys. D: Appl. Phys.* **29**, 34–38 (1996).

[60] Lu, S. and Chimpan, R., "Interpretation of Mueller matrices based on polar decomposition" *J. Opt. Soc. Am. A* **13**, 1106–113 (1996).

[61] Morio, J. and Goudail, F., "Influence of the order of diattenuator, retarder, and polarizer in polar decomposition of Mueller matrices" *Opt. Lett.* **29**, 2234–2236 (2004).

[62] Ossikovski, R., de Martino, A., and Guyot, S., "Forward and reverse product decompositions of depolarizing Mueller matrices" *Opt. Lett.* **32**, 689–691 (2007).

[63] Anastasiadou, M., Ben Hatit, S., Ossikovski, R., Guyot, S., and de Martino, A., "Experimental validation of the reverse polar decomposition of depolarizing Mueller matrices" *J. Europ. Opt. Soc. - Rap. Pub.* **2** (2007).

[64] Swami, M. K., Manhas, S., Buddhiwant, P., Ghosh, N., Uppal, A., and Gupta, P. K., "Polar decomposition of 3 x 3 Mueller matrix: a tool for quantitative tissue polarimetry" *Opt. Exp.* **14**, 9324–9337 (2006).

[65] Ossikovski, R., Anastasiadou, M., and de Martino, A., "Product decompositions of depolarizing Mueller matrices with negative determinants" *Opt. Commun.* **281**, 2406–2410 (2008).

[66] Manhas, S., Swami, M. K., Buddhiwant, P., Ghosh, N., Gupta, P. K., and Singh, K., "Mueller matrices approcah for determination of optical rotation in chiral turbid media in backscattering geometry" *Opt. Exp.* **14**, 190–202 (2006).

[67] Fry, E. S. and Kattawar, G. W., "Relationships between elements of the Stokes matrix" *Appl. Opt.* **20**, 2811–2814 (1981).

[68] Gil, J. and Bernabeu, E., "A depolarization criterion in Mueller matrices" *Opt. Acta* **32**, 259–261 (1985).

[69] Gil, J. J. and Bernabeu, E., "Depolarization and Polarization Indices of an Optical System" *J. Mod. Opt.* **33**, 185–189 (1986).

[70] Chipman, R. A., "Depolarization index and the average degree of polarization" *Appl. Opt.* **44**, 2490–2495 (2005).

[71] Boulvert, F., Piederrière, Y., Le Brun, G., Le Jeune, B., and Cariou, J., "Comparison of entropy and polarization memory rate behaviors through a study of weakly-anisotropic depolarizing biotissues" *Opt. Commun.* **272**, 534–538 (2007).

[72] O'Neill, E. L., ed., [*Introduction to statistical optics*], vol. 27, Reading Massachusets, Addison-Wesley (1963).

[73] Cloude, S., "Group theory and polarisation algebra" *Optik (Stuttgart)* **75**, 26–36 (1986).

[74] Goldstein, D. H., "Applications and limitations of polarimetry" *Proc. SPIE* **1317**, 210–222 (1990).

[75] Gil, J. J., "Polarimetric characterization of light and media. Physical quantities involved in polarimetric phenomena" *Euro. Phys. J. App. Phys.* **40**, 1–47 (2007).

[76] Wriedt, T., "Mie type codes, http://www.iwt-bremen.de/vt/laser/wriedt/mie_type_codes/body_mie_type_codes.html" (2008).

[77] Barnett, D., "Matlab mie functions, http://www.lboro.ac.uk/departments/el/research/photonics/matmie/mfiles.html" (2008).

[78] Du, H., "Mie-Scattering Calculation" *Appl. Opt.* **43**, 1951–1956 (2004).

[79] Hecht, L., Jordanov, B., and Schrader, B., "Stokes Mueller treatment of artifacts in natural Raman optical activity" *Appl. Spect.* **41**, 295–307 (1987).

[80] Nee, T., Nee, S. F., Yang, D., and Huang, Y., "Scattering polarization by anisotropic biomolecules" *J. Opt. Soc. Am. A* **25**, 1030–1038 (2008).

[81] Videen, G., Bickel, W. S., and Boyer, J. M., "Coherent fluorescent emission and scattering from a uniform sphere" *Phys. Rev. A* **44**, 1358–1365 (1991).

[82] Videen, G., Bickel, W. S., and Boyer, J. M., "Coherent fluorescent emission and scattering from a uniform cylinder" *Phys. Rev. A* **43**, 5655–5664 (1991).

[83] Lakowicz, J. R., [*Principles of Fluorescence Spectroscopy*], Springer,Berlin, Germany (2006).

[84] Swaminathan, R. and Hoang, C. P. and Verkman, A. S., "Photobleaching Recovery and Anisotropy Decay of Green Fluorescent Protein GFP-S65T in Solution and Cells: Cytoplasmic Viscosity Probed by Green Fluorescent Protein Translational and Rotational Diffusion" *Biophys. J.* **72**, 1900–1907 (1997).

[85] Shindo, Y. and Oda, Y., "Mueller matrix approach to fluorescence spectroscopy. Part I: Mueller matrix expressions for fluorescent samples and their application to problems of circularly polarized emission spectroscopy" *Appl. Spect.* **46**, 1251–1259 (1992).

[86] Stefani, M. and Dobson, C., "Protein aggregation and aggregate toxicity: new insights into protein folding, misfolding diseases and biological evolution" *J. Mol. Med.* **81**, 678–699 (2003).

[87] Lindgren, M., Sörgjerd, K., and Hammarström, P., "Detection and characterization of aggregates, prefibrillar amyloidogenic oligomers, and protofibrils using fluorescence spectroscopy" *Biophys. J.* **88**, 4200–4212 (2005).

[88] Sörgjerd, K., Klingsted, T., Lindgren, M., Kågedal, K., and Hammarström, P., "Prefibrillar transthyretin oligomers and cold stored native tetrameric transthyretin are cytotoxic in cell culture." *Biophys. Res. Commun.* (2008). PMID: 18983977 [PubMed - as supplied by publisher].

[89] Tyo, J. S., Goldstein, D. L., Chenault, D. B., and Shaw, J. A., "Review of passive imaging polarimetry for remote sensing applications" *Appl. Opt.* **45**, 5453–5469 (2006).

[90] Collet, C., Zallat, J., and Takakura, Y., "Clustering of Mueller matrix images for skeletonized structure detection" *Opt. Exp.* **12**, 1271–1280 (2004).

[91] Baba, J. S., Chung, J., DeLaughter, A. H., Cameron, B. D., and Cote, G. L., "Development and calibration of an automated Mueller matrix polarization imaging system" *J. Biomed. Opt.* **7**, 341–349 (2002).

[92] Meriaudeau, F., Ferraton, M., Stolz, C., Morel, O., and Bigué, L., "Polarization imaging for industrial inspection" *Proc. SPIE* **6813**, 681308–1,681308–10 (2008).

[93] Chipman, R. A. and Wolfe, J., "Reducing symmetric polarization aberrations in a molded glass lens by annealing" *Proc. SPIE* **5888**, 72–79 (2005).

[94] Kaplan, B., Compain, E., and Drevillon, B., "Phase-modulated Mueller ellipsometry characterization of scattering by latex sphere suspensions" *Appl. Opt.* **39**, 629–636 (2000).

Paper I

Design and characterization of achromatic 132° retarders in CaF_2 and fused silica

Journal of Modern Optics $\mathbf{55}$, (14),2203-2214,(2008)

Is not included due to copyright

Paper II

Well-conditioned multiple laser Mueller matrix ellipsometer

Optical Engineering **47**(7), 073604 (2008)

Is not included due to copyright

Paper III

Fast near-infra-red spectroscopic Mueller matrix ellipsometer based on ferroelectric liquid crystal retarders

Physica Solidi Status (c) **5**, (5), 1097-1100 (2008)

Is not included due to copyright

Paper IV

Product decomposition of measured Mueller matrices from the FLC based NIR Mueller Matrix Ellipsometer

Physica Solidi Status (c) **5**, (5), 1093-1096 (2008)

Is not included due to copyright

Paper V

Discriminating land mines from natural backgrounds by depolarization

Proc. SPIE , Paper 7114-16 (2008.)

Is not included due to copyright

Paper VI

Quantum efficiency and two-photon absorption cross-section of conjugated polyelectrolytes used for protein conformation measurements with applications on amyloid structures

Chemical Physics **336** 121-126 (2007)

Available online at www.sciencedirect.com
ScienceDirect
Chemical Physics 336 (2007) 121–126
Chemical Physics
www.elsevier.com/locate/chemphys

Quantum efficiency and two-photon absorption cross-section of conjugated polyelectrolytes used for protein conformation measurements with applications on amyloid structures

Frantz Stabo-Eeg [a,*], Mikael Lindgren [a], K. Peter R. Nilsson [b], Olle Inganäs [b], Per Hammarström [b]

[a] *Norwegian University of Science and Technology, N-7491 Trondheim, Norway*
[b] *IFM Department of Physics, Chemistry and Biology Linköping University, S-581 83 Linköping, Sweden*

Received 18 August 2006; accepted 5 June 2007
Available online 22 June 2007

Abstract

Amyloid diseases such as Alzheimer's and spongiform encephalopathies evolve from aggregation of proteins due to misfolding of the protein structure. Early disease handling require sophisticated but yet simple techniques to follow the complex properties of the aggregation process. Conjugated polyelectrolytes (CPEs) have shown promising capabilities acting as optical biological sensors, since they can specifically bind to polypeptides both in solution and in solid phase. The structural changes in biomolecules can be monitored by changes of the optical spectra of the CPEs, both in absorption and emission modes. Notably, the studied CPEs possess multi-photon excitation capability, making them potential for *in vivo* imaging using laser scanning microscopy. Aggregation of proteins depends on concentration, temperature and pH. The optical effect on the molecular probe in various environments must also be investigated if applied in these environments. Here we present the results of quantum efficiency and two-photon absorption cross-section of three CPEs: POMT, POWT and PTAA in three different pH buffer systems. The extinction coefficient and quantum efficiency were measured. POMT was found to have the highest quantum efficiency being approximately 0.10 at pH 2.0. The two-photon absorption cross-section was measured for POMT and POWT and was found to be more than 18–25 times and 7–11 times that of Fluorescein, respectively. We also show how POMT fluorescence can be used to distinguish conformational differences between amyloid fibrils formed from reduced and non-reduced insulin in spectrally resolved images recorded with a laser scanning microscope using both one- and two-photon excitation.
© 2007 Elsevier B.V. All rights reserved.

Keywords: Quantum efficiency; Bio-sensing; Two-photon absorption; Polythiophenes; Conjugated polymers; Protein aggregation; Conformational changes

1. Introduction

Misfolded proteins and peptides can evolve into amyloid fibrils. Aggregates of such structures are known to be the hallmark of a least 20 different diseases [1], including Diabetes II, Alzheimer's and Parkinson's. During the formation of fibrils the abnormal protein conformations can go through several pre-fibrillar states. In the search of effective treatment a better understanding of how such precursor states are formed is therefore of interest. Our laboratories are working towards understanding the molecular basis behind protein misfolding diseases. A plethora of new molecules and fluorescence techniques are developed to facilitate this work. Previously, we have shown how substituted conjugated polymers, so called conjugated polyelectrolytes (CPEs) can be used to study peptides and proteins conformational changes [2–5]. Notably, chiral CPEs bind differently to different enantiomers of synthetic

* Corresponding author. Tel.: +47 73593455.
E-mail address: Frantz.Stabo-Eeg@phys.ntnu.no (F. Stabo-Eeg).

0301-0104/$ - see front matter © 2007 Elsevier B.V. All rights reserved.
doi:10.1016/j.chemphys.2007.06.020

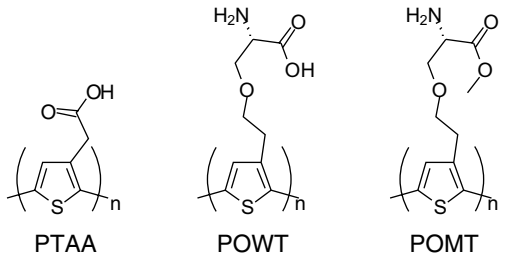

Fig. 1. Scheme: Molecular structures of POMT, POWT and PTAA.

peptides [2]. They can also be used to stain regions of amyloidic misfolded proteins in tissue samples. It has been shown that two photon excitation of fluorescence is a possible route for bioimaging of tissue samples [6]. Most importantly CPE's change their conformation depending on the binding partner (protein) and the environment. This conformational change induces a change in optical properties of the CPE and thereby directly couples protein conformation to spectroscopic signal. Of interest is to enable analysis of conformational variations within amyloid structures to facilitate our understanding of heterogeneities of fibrillar states. Non-linear characterization together with fluorescence anisotropy are currently also being applied and have been shown capable of detecting small aggregates of dye label peptide [7].

Aggregation of proteins depends on concentration, temperature and pH. To effectively use CPEs as optical biosensors, their optical properties in the solvent of choice must also be investigated, to determine if there are changes of the probes in addition to changes due to binding to biomolecules [3,8]. Very often acidic pH is applied to destabilize the native protein conformation in order to facilitate protein misfolding on the timescale of minutes to days instead of years in an affected individual. This paper presents the photo-physical characterization of three CPEs: POMT (poly(3-[(*S*)-5-amino-5-methoxycarboxyl-3-oxapentyl]-2, 5-thiophenylene hydrochloride): Nilsson et al. [2]), POWT (poly(3-[(*S*)-5-amino-5-carboxyl-3-oxapentyl]-2,5-thiophenylene hydrochloride): Andersson et al. [9]), and PTAA (poly(thiophene-3-acetic acid): Ding et al. [10]). The extinction coefficient and quantum efficiency (QE) of these CPEs in three widely used buffer systems, 10 mM HCl pH 2.0, 20 mM MES pH 5.9, and 100 mM Na_2CO_3 pH 10.0, at room temperature, were investigated. For POMT and POWT also the two-photon absorption cross-section was determined. A scheme with the studied structures is shown in Fig. 1.

2. Experimental

A Shimadzu UV-1601 PC UV–visible spectrophotometer was used for the absorption measurements. For time and spectrally resolved detection, a Jobin Yvon IBH FluoroCube photon-counting spectrometer was used. All spectra were corrected against the wavelength dependent detector effciency. Fluorescence was measured in time-correlated single photon counting (TC-SPC) mode. For two-photon absorption cross-section measurements the 180 fs pulses of the Ti:Sapphire laser (Coherent MIRA 900-F) was used. A pulse picker (Coherent 9200 Pulse Picker) was used to lower and control (9.5 kHz to 4.75 MHz) the pulse repetition frequency. An IBH TB-01 module (optical trigger) was used as time-reference using a thin glass wedge to take out a small part of the fundamental. For the single photon excitation luminescence of a 443 nm IBH NanoLED (S/N 04493) was used.

The different dilute concentrations of the polymers were prepared in the following manner before performing the measurements: first the three polymers were weighted and dissolved in deionized water at concentrations 1 (mg/ml) in separate initial solutions. Then 3×3 quartz cuvettes containing the three pH buffer solution were prepared. The concentrations was then increased by adding small amounts of the polymers from the initial solutions. The procedure was performed for fluorescein dissolved in NaOH, used as a reference sample in the QE measurements.

Amyloid fibrils were generated through incubation of 320 μM bovine insulin in 25 mM HCl at 65 °C the presence and absence of reducing agent (14 mM β-mercaptoethanol) for 5 days. Staining with POMT was performed taking a 30 μl aliquot of amyloid fibrils into 500 μl 25 mM HCl and mixing with 2.5 μl of POMT (1 mg/ml). The stained amyloid were pelleted through centrifugation at 3000 rpm for 15 minutes and the pellet was applied on a glass microslide. The amyloid fibrils were visualized using a Zeiss 510-LSM equipped with a META spectral detector. Excitation was performed using a 488 nm argon laser and a Ti:Sapphire fs laser tuned to 820 nm used for two-photon excitation, for further details, see [6].

3. Results and discussion

3.1. Extinction coefficient

Representative plots of absorbance versus CPE concentration for PTAA dissolved in the three buffer systems (mol/l), are shown in Fig. 2. From these experimental data the extinction coefficient in each CPE/solvent case ϵ was calculated from the gradient of the linear fit by the use of the well known Beers law; $A = \log\left(\frac{I_0}{I_t}\right) = \epsilon c l$, where A is the absorption, l is the quarts cuvette length, c is the concentration. The results in terms of absorbance are summarized in Table 1. Each CPE was typically a distribution of different chain lengths in the range 10–26 units. Due to this distribution average molecular weights were calculated from the figures in [2,4]. They were found to be 3750 ± 170 g/mol for POWT, 4630 ± 260 g/mol for POMT and 2500 ± 260 g/mol for PTAA.

A red-shifted maximum and a large extinction coefficient is generally believed to occur for the longest conjugation length. At low pH the amino groups become protonated. This happens at pH below the *isoelectric* point

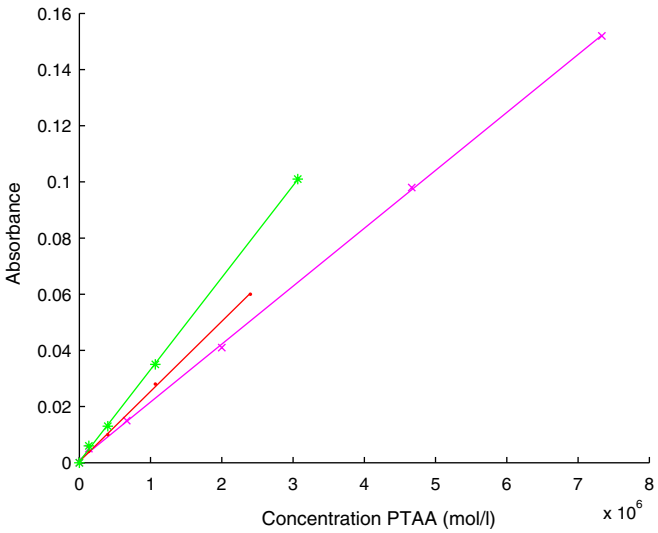

Fig. 2. Absorbance at 443 nm of PTAA (OD) vs. concentration (mol/l) (buffers: (×) pH 2.0, (●) pH 5.9, (*) pH 10).

Table 1
The extinction coefficient ϵ 10^4 (l/mol cm^{-1}) and absorption maximum $A_{\lambda max}$ (nm) and emission maximum $F_{\lambda max}$ for POMT, POWT and PTAA in various pH buffers

Sample	pH 2.0	pH 5.9	pH 10.0
POMT $\epsilon_{\lambda=443}$	19.8	10.1	8.46
POWT $\epsilon_{\lambda=443}$	8.22	5.76	6.09
PTAA $\epsilon_{\lambda=443}$	2.06	2.50	3.27
POMT $A_{\lambda max}$	460	415	450
POWT $A_{\lambda max}$	420	400	430
PTAA $A_{\lambda max}$	425	420	450
POMT $F_{\lambda max}$	590	585	610
POWT $F_{\lambda max}$	580	570	600
PTAA $F_{\lambda max}$	590[a]	590	600

[a] Very weak and noisy fluorescence signal.

(p*I*), pH 5.9 for POWT and pH 9.2 POMT, resulting in a planar polythiophene backbone by charge repulsion between adjacent substituents. This agrees well with the data of POMT and POWT both having a strong absorption and red-shift for the expected planar conformation (Table 1). By similar arguments the shortest wavelength of the absorption maximum as well as the minimum extinction coefficient occur for the conformation with the shortest conjugation length. For POMT and POWT this occurs around the intermediate pH or higher pH. PTAA on the other hand does not contain the amino group and consequently the substituent becomes charged at high pH where the proton of the carboxyl group is attracted to the solvent, rendering the substituent negatively charged. Hence, the red-shift of the absorption maximum along with the maximum extinction coefficient occur at high pH (Table 1).

This is in agreement with earlier circular dichroism studies of POWT in pH buffer solution showed that pH-levels equal to the isoelectric point (p*I*) at pH 5.9 for this amino-acid leads to a helical conformation of the polymer backbone [4,11]. In this conformation the overlap of the π-orbitals is reduced, resulting in a shorter conjugation length. This is the common explanation of the blue shift at pH 5.9 [11] (see also Table 1). The two other polythiophenes also experienced a similar absorption shift at intermediate pH. CD spectra taken of POMT around the same pH-value confirmed a similar structural configuration [2]. Single chain conformational changes for PTAA around the pK_a value at pH 5.0–6.0 were earlier reported by Kim et al. [12], also attributed to be a planar to non-planar transition. PTAA is known to be in an achiral state in deionized water and in 20 mM sodium phosphate at pH 7.4. Extremely poor fluorescence was also experienced here for pH levels below pH 4 [12], as will be discussed further below.

3.2. Quantum efficiency

The quantum efficiency (QE) of a compound is defined as the probability for an absorbed photon to be re-emitted as luminescence. In absolute quantum efficiency measurements an extensive knowledge of the detection system is needed. However, the relative quantum efficiency can be determined by comparing the absorbance versus emission of the unknown sample relative a reference sample under identical experimental conditions. Thus, QE (ϕ_X) for a dilute sample X is given by [13]

$$\phi_X \approx \frac{F_X A_R}{F_R A_X}\left(\frac{n_x}{n_r}\right)^2 \phi_R. \quad (1)$$

Here F_X and F_R are the integrated fluorescence spectrum, A_X and A_R the absorbance at the excitation wavelength. n_x and n_r are the refractive indices of the sample and reference, respectively. The refractive index are here approximated to be equal.

The absorbance and fluorescence spectra were collected for the CPEs dissolved in each of the buffers at increasing concentrations and care was taken to avoid too high concentration (absorbance was kept below OD 0.1). For each series of measurements a new reference data set was recorded to avoid errors from unexpected changes or drift of the excitation and detection systems. Representative plots of the integrated fluorescence versus absorbance are shown for PTAA in Fig. 3. The slope of the fitted straight lines was compared to the data of the well documented reference standard; fluorescein dissolved in 0.1 M NaOH having a QE of 0.90 [13]. The resulting QEs are collected in Table 2.

In contrast to the wavelength dependence of both the extinction coefficient and the absorbance maximum the quantum efficiency is not as straight forward to interpret. The strength of both the extinction coefficient and the spontaneous emission are proportional to the electronic transition dipole moment and to first order an increase or decrease of the conjugation length of the π-system would cancel if other dynamic quenching mechanisms are neglected. Nevertheless, both POMT and POWT (at low

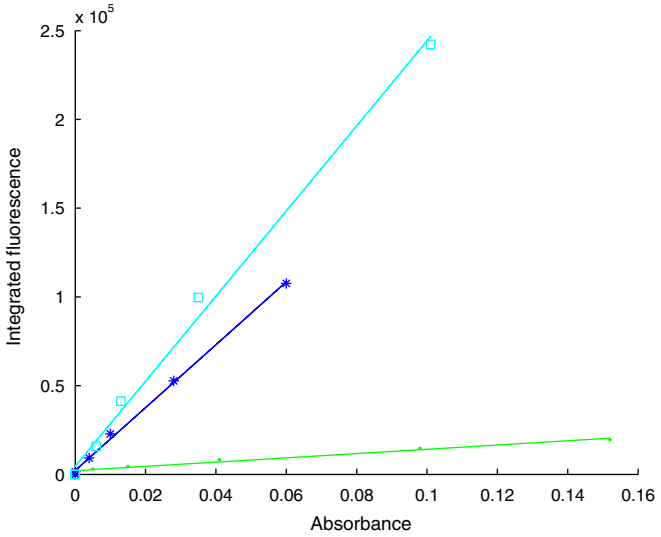

Fig. 3. Absorbance of PTAA vs. integrated fluorescence (buffers (●) pH 2.0, (∗) pH 5.9, (□) pH 10).

Table 2
The measured quantum efficiency of POMT, POWT and PTAA for various pH concentration

Sample	$\phi_{\text{pH 2.0}}$	$\phi_{\text{pH 5.9}}$	$\phi_{\text{pH 10.0}}$
POMT	0.10	0.077	0.090
POWT	0.073	0.066	0.043
PTAA	0.0014	0.020	0.027

The refractive indexes in hence NaOH and the buffers are approximated equal.

pH) as well as PTAA (at high pH) have their largest QE corresponding to the planar conformation. We interpret this to the flexibility of the polymer chain: in solution the extended conformation is more stiff and less susceptible to relaxation processes imposed by local motions close to the excitation center that can quench the fluorescence. We also want to emphasize that the results of our samples in diluted solutions are not possible to directly compare with those obtained from conjugated polymers in solid films for which extensive data exist in the literature (see, e.g. Berggren et al. [14]). Comparing the three CPEs used in our experiments performed under similar conditions we note that all three conjugated polymers have a similar backbone with different substitution schemes. C=O bonds are present in all three of them, and this is known to have a the strong electron affinity and perturb excitations within the π-conjugation framework, see Rothberg et al. (quenching in phenylenevinylene polymers [15]). For POWT at higher pH values the amino group in the side chain is deprotonated which enable it to behave as an hydrogen bond acceptor, and the polymer can form aggregates [11]. PTAA also form aggregates at pH below pH 4 as the carboxyl-group become uncharged [12]. This aggregation process explain the poor QE for PTAA at pH 2.0 and for POWT at pH 10 as they both become quenched. It's noted that POMT increase it's QE at pH 10 which is peculiar since POMT's pK_a value are located in the region around pH 9–10. Then POMT is uncharged and should more easily form aggregates. For instance POMT has been shown to form aggregates in alkaline buffer solutions with low ionic strength [2]. However, other investigations also show that when first dissolving the probe in deionized water and then diluting the probe in a buffer with higher ionic strength, similar conditions as used for the QE experiments, no precipitation of the polyelectrolyte is observed [6].

3.3. Two-photon absorption cross-section

The penetration depth by light in general biological tissue is largest in the near infrared (IR) region (750–850 nm). Further towards the IR absorption of vibrational overtones of O-H bonds of water and related bond become larger. Towards the visible and UV–vis region both electronic absorption and scattering increase. Dyes with dipolar excitations in the visible–UV can usually also be excited by two-photon absorption by using wavelengths in the near IR. The two-photon excitation (2PA) process is therefore of interest because of improved optical depth. 2PA is a non-linear process proportional to the square of the light intensity. A tight focus along with dyes designed to have high 2PA cross-section is therefore required. We have previously shown that 2PA can be used for imaging applications [6] and also made preliminary quantification of the importance of 2PA in peptide–POMT association experiments [2]. Here we determined the absolute 2PA cross-section by using a fluorescence technique.

The time-averaged fluorescence $\langle F\rangle$ following from two-photon absorption are given by Webb and Xu [16]

$$\langle F(t)\rangle = \frac{1}{2}\phi\eta C\delta\frac{8n\langle P(t)\rangle^2}{\pi\lambda}. \tag{2}$$

Here ϕ is the quantum efficiency, η is a geometrical factor of the excitation and detection system, δ is the two photon absorbtion cross-section, C is the concentration of the fluorophore, n the refractive index of the solvent and finally $\langle P(t)\rangle$ and λ are the time averaged laser power (photons/second) and wavelength of the excitation source, respectively.

The determination of the 2PA cross-section can be further simplified if a reference dye with a known 2PA cross-section and QE is used. Eq. (2) can then be further simplified [17] by taking the ratio between a reference R and the measurand X.

$$\delta_X = \frac{\eta_R\phi_R C_R\langle P_R\rangle^2 n_R\langle F(t)\rangle_X}{\eta_X\phi_X C_X\langle P_X\rangle^2 n_X\langle F(t)\rangle_R}\delta_R \tag{3}$$

η and $\langle P\rangle^2$ are kept constant and n is approximately equal in all the solutions, giving

$$\delta_X \approx \frac{\langle F\rangle_X\phi_R C_R}{\langle F\rangle_R\phi_X C_X}\delta_R. \tag{4}$$

POWT and POMT were excited by light at 800 nm using a $f = 10$ cm lens to focus the beam into the fluorescence

compartment. Care was taken to optimize the position of the focus to be optimal with respect to the fluorescence detection system. The excitation laser was set to 4.75 MHz repetition rate and by scanning the monochromator, typically residing 2 s at each wavelength, and counting the total number of detected photons at each point, a two-photon absorption induced fluorescence spectrum is obtained.

Representative plots for POMT in the three different buffer solutions along with the Fluorescein reference is shown in Fig. 4. The associated 2PA cross-sections were calculated from the corrected fluorescence spectrum, see Table 3. As reference we used fluorescein dissolved in water at pH 11 with molecular 2PA cross-section shown to have a constant 2PA value within the uncertainties from 750–800 nm, being approximately $\delta = 38 \pm 9.7 \times 10^{-50}$ (cm^4 s/photon)[16,18] at 50 μM concentration. POWT and POMT were dissolved at 25 μM concentration in the three pH buffer solution. The absorption was hereby sufficiently low for avoiding potential artifacts from re-absorption and other quenching mechanisms.

An error estimate of our 2PA cross-section values concluded that the largest uncertainties originate from the reference sample about 25%, the estimated consecrations 15% and the calculated quantum yield values 15%. Altogether the uncertainty is estimated to be approximately 35%. This is similar to values reported earlier by Webb [18] and also our previous comparison between direct (Z-scan) and fluorescence based 2PA cross-section [19].

As can be seen from Table 3 both POMT and POWT have their strongest absorption, both single and two-photon, for pH 2.0. This corresponds to the most planar structure. Going from the intermediate pH to pH 2 the extinction coefficient of POMT is approximately doubled, whereas the two-photon absorption cross-section increase a factor 3/2. For POWT both the extinction coefficient and the 2PA cross-section increase by the approximate 3/2 ratio. To first order, the 2PA cross-section is proportional to the square of the transition moment of the linear single-photon absorption. However, since the single and two-photon absorption processes occur under different selection rules, not exactly the same electronic states are involved in the two processes. Nevertheless, the increase in 2PA cross-section going from the intermediate pH and a helical conformation to a planar conformation is considerably larger. Two-photon excitation has earlier been reported to be more dependent on conjugation length than one-photon excitation [20,21].

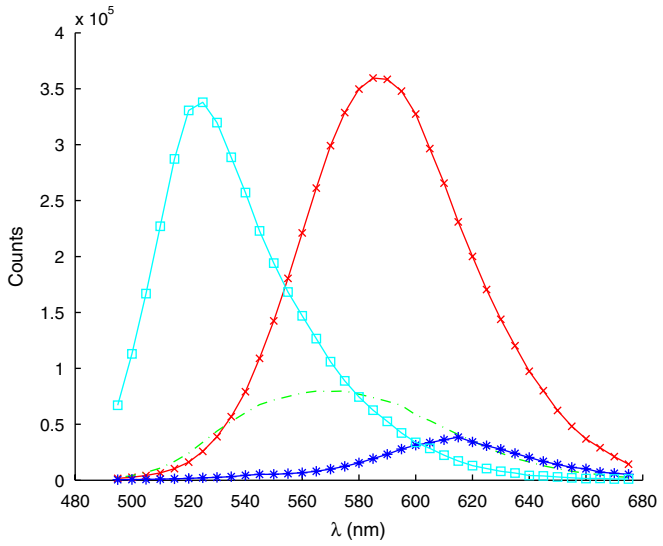

Fig. 4. Two-photon absorbtion induced luminescence spectrum of POMT ((□) Fluorescein in water (pH 11), POMT in buffers (×) pH 2.0, (●) pH 5.9, (☆) pH 10).

Table 3
Calculated 2PA cross-section (10^{-48} cm^4 s/photon) of POMT and POWT with estimated uncertainties of approximate 35%

Sample	$\delta_{pH\,2.0}$	$\delta_{pH\,5.9}$	$\delta_{pH\,10.0}$
POMT	10	6.9	7.1
POWT	4.2	2.8	4.0

3.4. Application

We also analyzed POMT emission from amyloid fibrils generated from reduced and non-reduced insulin, see Fig. 5. Amyloid fibrils from reduced insulin, with separated A and B chains, fluoresce with an augumented Thioflavin T fluorescence compared to non-reduced insulin and display different fibrillation properties (Rajesh Mishra, PH unpublished results). Excitation using the 488 nm argon laser provides a red-shifted fluorescence emission peak of reduced

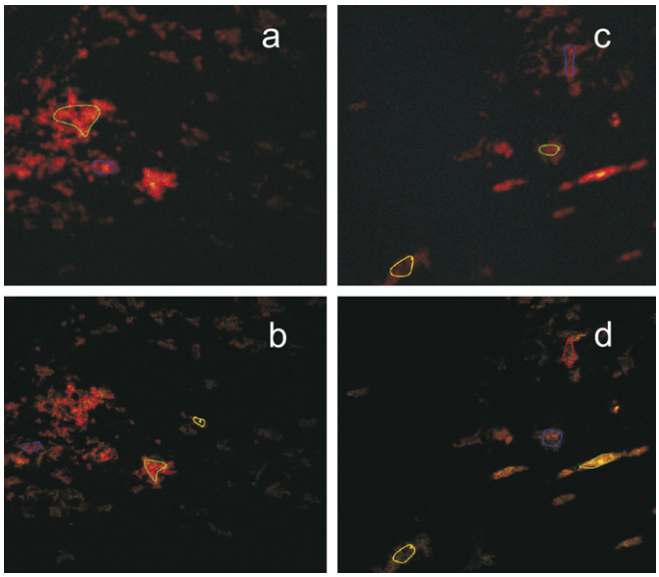

Fig. 5. Micrographs of insulin amyloid aggregates stained with POMT. (a) Two photon excitation 820 nm of reduced insulin amyloid; (b) 488 nm excitation of reduced insulin amyloid; (c) Two photon excitation 820 nm of non-reduced insulin amyloid; (d) 488 nm excitation of non-reduced insulin amyloid.

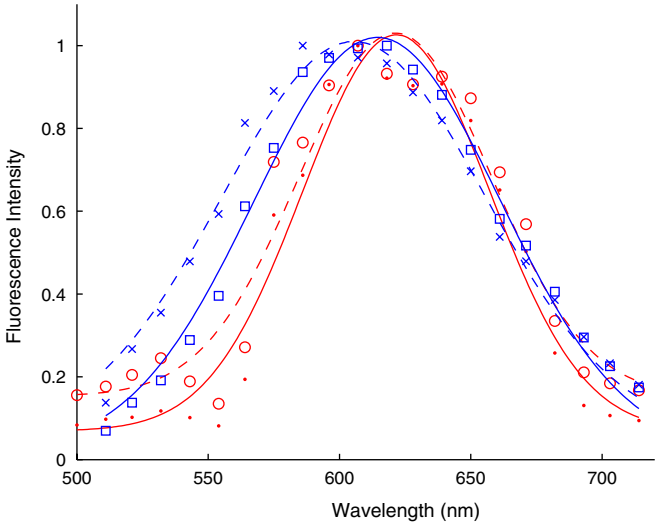

Fig. 6. Averaged spectra from 3 to 4 regions of interest (ROI) indicated in the micrographs in Fig 5. The averaged data points were fitted to a Gaussian function to provide the emission peak. Symbols: Two photon excitation 820 nm of reduced insulin amyloid (○, dashed line); Two photon excitation 820 nm of non-reduced insulin amyloid (●, solid line); 488 nm excitation of non-reduced insulin amyloid (×, dashed line); 488 nm excitation of reduced insulin amyloid (□, solid line).

insulin (peak at 614 nm) compared to non-reduced insulin (peak at 605 nm) indicating a more planar backbone or more tightly assembled POMT molecules bound to the reduced insulin fibrils, see Fig. 6. Emission from 2-photon excitation provides the same emission peak (621 nm) for both types of amyloid fibrils. Interestingly, the POMT emission spectra using 2-photon excitation are red-shifted compared to single photon excitation. This was previously shown for amyloid plaque in brain tissue from an Alzheimer's disease patient [6].

4. Summary and conclusion

The photophysical properties of three CPE's in three buffer systems widely used in vitro and for ex vivo tissue samples for protein conformation measurements were explored. PTAA has a poor quantum efficiency compared to both POWT and POMT in all pH buffers. This might be due to a shorter inter-atomic distance between the conjugated chain and the quenching carboxyl group. POMT and POWT also have a stronger overall fluorescence than PTAA at acidic pH due to higher absorption. Both POMT and POWT should therefore be good candidates for applications in protein amyloid samples stained at acidic pH. POMT and POWT showed strong 2PA-cross-sections. Comparing with another widely used two-photon dye Fluorescein in pH 11 water, the molecular cross-section is around 25 times larger for POMT. The much larger cross-section of the CPEs can be explained by the longer conjugation length of POMT and POWT. POMT have an averaged mean polymer length of 20–21 thiophene rings along one dimension, while fluorescein consist of four aromatic rings in one unit. POWT has lower extinction coefficient, QE and two photon cross-section than POMT. Notably, the structural replacement of the hydrogen (from POWT) by a methyl-group in the carboxyl-group (to get POMT) makes POMT a better candidate to be used in two-photon imaging. Finally we have shown an application of POMT as an optical probe distinguishing between amyloid fibrils formed from reduced and non-reduced insulin indicating that these fibrils have different conformations although originating from the same protein. The results is a clear indication that CPE's are very promising for use in applications involving non-transparent samples such as protein amyloid aggregates that can be imaged by laser scanning microscopy.

Acknowledgments

This work was partially supported by the Research Council of Norway within the NanoMat program, and by VR, Swedish research council and SSF, the Swedish foundation for strategic research. Thanks to Rajesh Mishra for helpful discussions about insulin amyloid heterogeneity.

References

[1] M. Stefani, C. Dobson, J. Mol. Med. 81 (2003) 678.
[2] K.P.R. Nilsson, J. Olsson, F. Stabo-Eeg, M. Lindgren, P. Konradsson, O. Inganäs, Macromolecules 38 (2005) 6813.
[3] K.P.R. Nilsson, J. Rydberg, L. Baltzer, O. Inganäs, Proc. Natl. Acad. Sci. USA 100 (2003) 10170.
[4] K.P.R. Nilsson, O. Inganäs, Macromolecules 37 (2004) 9109.
[5] K.P.R. Nilsson, A. Herland, P. Hammarström, O. Inganäs, Biochemistry 44 (2005) 3718.
[6] K.P.R. Nilsson, P. Hammarström, F. Ahlgren, A. Herland, E.A. Schnell, M. Lindgren, G.T. Westermark, O. Inganäs, Chem. Bio. Chem. 7 (2006) 1096.
[7] Y. Wang, T. Goodson, J. Phys. Chem. Lett. B 111 (2006) 327.
[8] K.P.R. Nilsson, O. Inganäs, Nature Mater. 2 (2003) 419.
[9] M. Andersson, P.O. Ekeblad, T. Hjertberg, O. Wennerström, O. Inganäs, Polym. Commun. 32 (1991) 546.
[10] L. Ding, M. Jonforsen, L.S. Roman, M.R. Andersson, O. Inganäs, Synth. Met. 110 (2000) 133.
[11] K.P.R. Nilsson, M. Andersson, O. Inganäs, J. Phys.–Condens. Mat. 304 (2002) 10011.
[12] B.-S. Kim, L. Chen, J. Gong, Y. Osada, Macromolecules 32 (1999) 3964.
[13] J. Demas, G.A. Crosby, J. Phys. Chem. 75 (1971) 991.
[14] M. Berggren, P. Bergman, J. Fagerström, O. Inganäs, M. Andersson, H. Weman, M. Granström, S. Stafström, O. Wennerström, T. Hjertberg, Chem. Phys. Lett. 304 (1999) 84.
[15] L. Rothberg, M. Yan, F. Papadimitrakopoulos, M. Galvin, E. Kwock, T. Miller, Synth. Met. 80 (1996) 41.
[16] C. Xu, W.W. Webb, J. Opt. Soc. Am. B 13 (1996) 481.
[17] J.M. Song, T. Inque, H. Kawazumi, T. Ogawa, Anal. Sci. 15 (1999) 601.
[18] M.A. Albota, C. Xu, W.W. Webb, Appl. Opt. 37 (1998) 7352.
[19] E. Glimsdal, M. Carlsson, B. Eliasson, B. Minaev, M. Lindgren, J. Phys. Chem. A 111 (2) (2007) 244.
[20] P. Norman, Y. Luo, H. Ågren, Opt. Commun. 168 (1999) 297.
[21] D. Beljonne, J.L. Bredas, J. Opt. Soc. Am. B 11 (1994) 1380.